

# High-speed silicon detector structures for photonic integrated circuits

# High-speed silicon detector structures for photonic integrated circuits

by

JASON ACKERT

B.Sc. Waterloo (2009)

A Thesis

Submitted to the School of Graduate Studies in Partial Fulfillment of the  
Requirements for the Degree

Doctor of Philosophy

McMaster University © Copyright of Jason Ackert, 2015

**McMaster University (Engineering Physics)**

**DOCTOR OF PHILOSOPHY (2015)**

**Hamilton, Ontario**

**TITLE:** High-speed silicon detector structures for photonic integrated circuits

**AUTHOR:** Jason Ackert, B.Sc. (University of Waterloo)

**SUPERVISORS:** Dr. A.P. Knights & Dr. P.E. Jessop

**NUMBER OF PAGES:** xv, 156

# Abstract

Computing as a service is rapidly becoming the new normal for many sectors of the economy. The widespread availability of broadband internet has allowed an extensive range of services to be delivered on-demand from centralized computing systems known as ‘data centers’. These systems have evolved to be enormously complex. Optical-based communication is desired to increase data center capability and efficiency, however traditional optical technologies are not feasible due to cost and size. Silicon photonics aims to deliver optical communications on an integrated and affordable platform for use in data centers by leveraging the existing capabilities of complementary metal-oxide semiconductor manufacturing.

This thesis contains a description of the development of monolithic silicon photodiodes for use in photonic integrated circuits in, and beyond, the current telecommunications wavelength windows. The focus is on methods which are compatible with standard silicon processing techniques. This is in contrast to the current approaches which rely on hybrid material systems that increase fabrication complexity.

Chapter 1 and 2 provide background information to place this work into context. Chapter 3 presents an experimental study of resonant devices with lattice defects which determines the refractive index change in silicon-on-insulator waveguides. High-speed operation of resonant photodiodes is demonstrated and is found to be limited by resonance instability. Chapter 4 demonstrates high responsivity avalanche photodetectors using lattice defects. The detectors are shown to operate error-free at 10 Gbit/s, thus confirming their capability for optical interconnects. Chapter 5 presents photodiodes operating with absorption through surface-state defects. These detectors show fast operation (10 Gbit/s) and have an extremely simple fabrication process. Chapter 6 demonstrates photodiodes operating beyond the traditional telecommunications window. Operation at 20 Gbit/s, at a wavelength of 1.96  $\mu\text{m}$  is demonstrated, offering potential for their use in the next generation of optical communication systems which will exploit the thulium doped fiber amplifier.

# Acknowledgements

Foremost I would like to thank my supervisors Andy Knights and Paul Jessop, and committee member Harold Haugen for the opportunity to complete this work, and their guidance in doing so.

Many thanks to all the members of the Knights-Jessop group who provided me with help over the years, Dixon '*D\$*' Paez, Ross '*the boss*' Anthony, Jimmy '*the angry one*' Zheng, Zhao '*the chairman*' Wang, Kyle '*KFM Radio*' Murray, David '*DJL*' Hagan, John Gellesta, Shabnam Homanpour, Dave Walters and Thomas Jacob. And a special thanks to the Ph.D. students preceding me, who offered help during my first years at McMaster, Edgar Huante-Ceron, Dylan Logan, Jonathan Doyle and Chris Brooks.

The work in this thesis relied on the effort of many collaborators; Abdullah Karar and John Cartledge at Queen's University, David Thomson, Li Shen and Goran Mashanovich at the University of Southampton and Marco Fiorentino and Ray Beausoleil at Hewlett-Packard Laboratories.

This work relied on externally sourced fabrication, and there are a lot of people who made that possible including Dan Deptuck and Jessica Zhang at CMC Microsystems. Lukas Chrostowski (and many others) for organizing and hosting the silicon photonics workshops which would become the Si-EPIC program. The first workshop I attended in 2009 at the University of British Columbia spurred my interest and provided me with the motivation to continue on in this field. Thanks to Doris Stevanovic and Zhilin Peng at McMaster University and Jack Hendriks at the University of Western Ontario for enabling the post-fabrication ion implantation.

Finally, I thank my parents. Without their support I would not have followed this path.

# Table of Contents

<b>Chapter 1 Introduction.....</b>	<b>1</b>
1.1 Photonics & computing.....	1
1.2 Silicon photonics as a solution.....	5
1.2.1 The strengths of silicon.....	5
1.2.2 Lasers.....	7
1.2.3 Modulation.....	8
1.2.4 Photodetection: The hybrid approach.....	10
1.2.5 Challenges of integration.....	12
1.2.6 Multi-project wafers and the ‘fabless’ approach.....	13
1.3 Monolithic silicon detectors.....	15
1.3.1 Defect-based detection.....	15
1.3.2 Long wavelength detection.....	16
1.3.3 Surface-state detection & other approaches.....	16
1.3.4 Resonant detectors.....	17
1.4 Contributions in thesis.....	18
1.5 Publications.....	19
1.6 Statement of work.....	20
<b>Chapter 2 Background.....</b>	<b>26</b>
2.1 Optical absorption.....	26
2.1.1 The frequency dependence of refractive index.....	27
2.1.2 Free carrier absorption.....	32
2.1.3 Two-photon absorption.....	34
2.1.4 Absorption through deep-level defects.....	34
2.1.5 Surface-state absorption.....	37
2.2 Photodiodes.....	38
2.2.1 <i>P-N</i> junction.....	38
2.2.2 <i>P-I-N</i> photodetector.....	40

2.2.3	Quantum efficiency .....	41
2.2.4	Operation speed limitations .....	42
2.3	Avalanche photodetectors .....	45
2.3.1	Avalanche multiplication .....	45
2.3.2	Avalanche noise .....	46
2.3.3	Avalanche-limited transit time .....	47
2.4	Optical resonators in silicon.....	48
2.4.1	Ring resonators .....	48
2.4.2	All-pass microring resonator.....	49
2.4.3	Coupling condition.....	51
2.4.4	Free spectral range .....	52
2.4.5	Quality factor .....	53
2.4.6	Racetrack resonators .....	54
2.5	High-speed measurement instrumentation.....	56
2.5.1	Modulation patterns .....	56
2.5.2	Frequency response characterization .....	57
2.5.3	Eye diagrams and bit-error rate measurement .....	58
2.6	Simulation tools .....	60
2.7	Summary .....	60
<b>Chapter 3 Resonant Detection via Mid-gap Lattice Defects .....</b>		<b>64</b>
3.1	The effect of lattice defects on the refractive index of silicon waveguides .....	65
3.1.1	Introduction .....	65
3.1.2	Device fabrication and experimental methods .....	65
3.1.3	Experimental results.....	67
3.1.4	Determination of the real component of the refractive index .....	70
3.1.5	Discussion .....	73
3.2	High-speed resonant detection via defect states in silicon ring resonators .....	74
3.2.1	Overview .....	74
3.2.2	Device fabrication and experimental methods .....	74
3.2.3	High-speed characterization method.....	76

3.2.4	Continuous-wave measurement results.....	76
3.2.5	High-speed measurement results.....	78
3.3	High-speed resonant detection via defect states in silicon disk resonators.....	81
3.3.1	Overview.....	81
3.3.2	Fabrication and device details.....	81
3.3.3	Continuous-wave characterization.....	82
3.3.4	Continuous-wave power loading.....	85
3.3.5	Frequency response.....	86
3.3.6	Carrier concentration modulation as a cause of instability.....	88
3.3.7	The shift in the imaginary index.....	91
3.4	Summary.....	92
 <b>Chapter 4   Avalanche High-Speed Photodetectors.....</b>		<b>96</b>
4.1	LETI devices.....	97
4.1.1	Design and fabrication.....	97
4.1.2	Continuous-wave characterization.....	98
4.1.3	Temperature response.....	100
4.1.4	Wavelength dependence.....	102
4.1.5	High-speed results.....	104
4.1.6	Bandwidth limiting factors.....	108
4.2	Devices fabricated at IME*ASTAR (Singapore).....	109
4.2.1	Fabrication.....	110
4.2.2	Continuous-wave results.....	110
4.2.3	High-speed results.....	111
4.3	Summary.....	118
 <b>Chapter 5   Photodetection with Si/SiO<sub>2</sub> Surface States.....</b>		<b>121</b>
5.1	Fabrication & Measurement.....	122
5.2	Surface-state detectors.....	125
5.2.1	Continuous-wave results.....	125
5.2.2	Optical power linearity.....	127

5.2.3 High-speed results.....	128
5.3 Bulk defects versus surface-state defects.....	129
5.3.1 Comparison of continuous-wave results .....	129
5.3.2 Comparison of high-speed operation .....	130
5.4 Summary .....	132
<b>Chapter 6 Long Wavelength Detection.....</b>	<b>134</b>
6.1 Integrated optics at extended wavelengths.....	134
6.2 Fabrication .....	136
6.3 Results.....	138
6.3.1 Continuous-wave measurements.....	138
6.3.2 High-speed measurements .....	142
6.4 Comparison with previous work described in this thesis.....	146
6.5 Summary .....	148
<b>Chapter 7 Summary, Suggested Future Work &amp; Outlook.....</b>	<b>152</b>
7.1 Summary of work .....	152
7.2 Suggested future work .....	153
7.2.1 Avalanche detection.....	153
7.2.2 Long wavelength detection .....	154
7.2.3 Surface-state photodetection .....	155
7.3 Outlook .....	155

# List of Figures

1.1	The ‘macrochip’ concept. A dense integration of multiple silicon dies connected with silicon photonic bridges. ....	4
1.2	Hybrid laser structures created with III-V semiconductor materials bonded to silicon-on-insulator wafers. ....	8
1.3	An optical modulator created with a silicon ring resonator.....	9
1.4	A silicon modulator cross section and 40 Gbit/s eye diagram .....	10
1.5	A hybrid photodetector created with germanium on silicon .....	11
1.6	A photograph of a multi-project wafer containing photodetectors used in this thesis. ....	14
2.1	The frequency dependent absorption coefficient and refractive index for a non-conducting medium.....	29
2.2	A simplified band diagram of a conductor, semiconductor and insulator.....	30
2.3	Optical absorption versus wavelength for various semiconductor materials .....	31
2.4	A simplified band diagram comparison of direct and indirect optical absorption. ....	32
2.5	The photoconductance and absorption spectra from p-type silicon irradiated with neutrons. ....	35
2.6	A simple model of the optical excitation process through a deep-level.....	36
2.7	A schematic diagram of an abrupt $p-n$ junction .....	39
2.8	A simplified band diagram of a $p-n$ junction showing photodetection .....	40
2.9	A schematic cross section of a $p-i-n$ waveguide photodetector.....	41
2.10	An equivalent electric circuit diagram of a photodiode .....	43
2.11	A conceptual diagram of the avalanche multiplication process .....	45
2.12	Schematic diagrams of a ring resonator and Fabry-Perot resonator.....	49

<b>2.13</b>	A schematic diagram of an all-pass ring resonator.....	50
<b>2.14</b>	An SEM image of an SOI racetrack resonator in an add-drop configuration ....	56
<b>2.15</b>	The transmission and reflection parameters for a 2-port device and a sample measurement from a network analyzer.....	58
<b>2.16</b>	A sample eye diagram with relevant metrics labelled.....	59
<b>3.1</b>	An SEM image of a racetrack resonator.....	67
<b>3.2</b>	Post ion implantation optical spectra of a racetrack resonator for various annealing temperatures.....	68
<b>3.3</b>	The resonance shift and excess loss of ion implanted racetrack resonators as a function of annealing temperature.....	69
<b>3.4</b>	The quality factor and resonance shift for racetrack resonators as a function of annealing temperature .....	70
<b>3.5</b>	A simulation of the change in effective index for an SOI waveguide as a function of the change in the real part of the silicon refractive index.....	71
<b>3.6</b>	An optical micrograph of a 40 $\mu\text{m}$ diameter ring resonator based photodetector .....	75
<b>3.7</b>	A block diagram of the high-speed characterization setup for resonant devices .....	76
<b>3.8</b>	Optical transmission and photodiode current as a function of wavelength for a 40 $\mu\text{m}$ diameter ring resonator detector.....	77
<b>3.9</b>	The current versus voltage and current versus wavelength for a ring resonator detector .....	77
<b>3.10</b>	Optical and photocurrent spectra for a 40 $\mu\text{m}$ diameter ring resonator detector at low power .....	78
<b>3.11</b>	A 5 Gbit/s eye diagram and the small-signal frequency response of a ring resonator detector .....	79
<b>3.12</b>	An optical micrograph and schematic diagram of a microdisk photodetector ...	82

<b>3.13</b>	Photocurrent and transmitted optical power spectra for a 10 $\mu\text{m}$ diameter microdisk photodetector .....	83
<b>3.14</b>	Photocurrent and transmitted optical power spectra for a 20 $\mu\text{m}$ diameter microdisk photodetector .....	84
<b>3.15</b>	A comparison of microdisk spectra with and without defects introduced via ion implantation.....	84
<b>3.16</b>	Photocurrent and transmitted optical power spectra for a 20 $\mu\text{m}$ diameter microdisk photodetector with increased optical power .....	85
<b>3.17</b>	A 10 Gbit/s eye diagram and the small signal frequency response of a 20 $\mu\text{m}$ diameter microdisk photodetector .....	86
<b>3.18</b>	Measured 5 Gbit/s bit patterns from a 20 $\mu\text{m}$ diameter microdisk for various displacements from resonance.....	87
<b>3.19</b>	The calculated blue-shift versus waveguide optical power for a ring resonator	90
<b>3.20</b>	The build-up factor versus single round-trip loss coefficient for a ring resonator .....	92
<b>4.1</b>	A schematic cross-section of the LETI photodiode .....	98
<b>4.2</b>	Current versus reverse bias voltage for a 600 $\mu\text{m}$ long LETI photodiode .....	99
<b>4.3</b>	Current versus optical power for a 200 $\mu\text{m}$ long LETI photodiode .....	100
<b>4.4</b>	The photocurrent response to annealing temperature of a LETI photodiode .....	101
<b>4.5</b>	The photocurrent response to operating temperature of a LETI photodiode .....	102
<b>4.6</b>	The wavelength dependence of the LETI photodiode.....	103
<b>4.7</b>	A block diagram of the experimental setup for high-speed characterization .....	104
<b>4.8</b>	A comparison of 200 and 800 $\mu\text{m}$ long LETI photodiodes.....	105
<b>4.9</b>	The small-signal frequency response of LETI photodiode with lengths 200, 600 and 800 $\mu\text{m}$ .....	106
<b>4.10</b>	Measured bit-patterns from a 200 $\mu\text{m}$ long LETI photodiode at 10 Gbit/s.....	107
<b>4.11</b>	The small-signal frequency response of a 600 $\mu\text{m}$ long LETI photodiode .....	108

<b>4.12</b>	Measured capacitance of the LETI photodiode for various lengths.....	109
<b>4.13</b>	A schematic cross-section of the IME #1 photodiode.....	110
<b>4.14</b>	Current versus voltage, and current versus operating temperature for the IME #1 photodiode .....	111
<b>4.15</b>	A block diagram of the high-speed characterization setup for the IME #1 photodiode .....	112
<b>4.16</b>	The small-signal frequency response of a 1 mm long IME #1 photodiode.....	112
<b>4.17</b>	10 Gbit/s eye diagrams of a 1 mm long IME #1 photodiode, with and without the use of a transimpedance amplifier .....	113
<b>4.18</b>	The bit-error rate versus received optical power for a 1 mm long IME #1 photodiode .....	114
<b>4.19</b>	Eye diagrams of the 1 mm long IME #1 photodiode at 14 and 20 Gbit/s.....	115
<b>4.20</b>	SEM images of the IME #1 photodiode showing a fabrication issue .....	117
<b>4.21</b>	SEM image of a directional coupler from the IME #1 fabrication run .....	118
<b>5.1</b>	SEM images of the IME #2 photodiodes .....	123
<b>5.2</b>	A schematic cross-section of the IME #2 photodiode.....	124
<b>5.3</b>	A block diagram of the experimental setup for the IME #2 photodiode.....	125
<b>5.4</b>	Current versus voltage for the IME #2 surface-state photodiode.....	126
<b>5.5</b>	Current versus optical power for the IME #2 surface-state photodiode.....	127
<b>5.6</b>	Eye diagrams of the IME #2 surface-state photodiode at 10 Gbit/s.....	128
<b>5.7</b>	A current versus voltage comparison of the surface-state photodiode and bulk defect detector .....	130
<b>5.8</b>	A 10 Gbit/s eye diagram of a 1 mm long IME #2 bulk defect photodiode .....	131
<b>5.9</b>	An eye diagram comparison of a surface-state and bulk defect detector at 10 Gbit/s .....	131
<b>6.1</b>	Schematic cross-section of IME #3 photodiode .....	137

<b>6.2</b>	SEM images of IME #3 photodiode .....	138
<b>6.3</b>	Current versus voltage for 1 mm long IME #3 photodiode at $\lambda=2.02 \mu\text{m}$ .....	139
<b>6.4</b>	Current response for IME #3 photodiode from $\lambda=1.96$ to $2.5 \mu\text{m}$ .....	140
<b>6.5</b>	Optical transmission of a 750 nm wide waveguide versus wavelength .....	141
<b>6.6</b>	Current versus optical power for IME #3 photodiode at $\lambda=2.2 \mu\text{m}$ .....	142
<b>6.7</b>	Experimental setup for high-speed characterization of IME #3 photodiode.....	143
<b>6.8</b>	28 Gbit/s eye diagrams of 1mm long IME #3 photodiode .....	143
<b>6.9</b>	Small signal frequency response of 1 mm and 200 $\mu\text{m}$ long IME #3 photodiode .....	144
<b>6.10</b>	Eye diagrams of 1 mm long IME # 3 photodiode for 15, 20 and 27 V reverse bias.....	145
<b>6.11</b>	A comparison of fabrication parameters for the four multi-project wafers in this thesis .....	147

# List of Acronyms & Abbreviations

AC – Alternating current

BERT – Bit-error rate test

CMOS – Complementary metal-oxide semiconductor

DC – Direct current

DUT – Device under test

EDFA – Erbium-doped fiber amplifier

FEC – Forward error correction

FIB – Focused ion beam

FSR – Free spectral range

IME A\*STAR – Institute for Microelectronics (Agency for Science, Technology and Research) , Singapore.

LETI - Laboratoire d'électronique des technologies de l'information, (Grenoble, France).

LNA – Lightwave network analyzer

MPW – Multi-project wafer

NRZ – non-return to zero

OOK – on-off keying

PIC – Photonic integrated circuit

PPG – Pulse pattern generator

PRBS – Pseudo-random binary sequence

Q – Quality factor

QE – Quantum efficiency

RC – Resistance-capacitance

RF – Radio frequency

RZ – return to zero

SEM – Scanning electron microscope

SOI – Silicon on insulator

TDFA – Thulium-doped fiber amplifier

TPA – Two-photon absorption

UV – Ultraviolet

VNA – Vector network analyzer

WDM – Wavelength-division multiplexing

# Chapter 1 Introduction

## 1.1 Photonics & computing

The photonics industry has entered an era of integration. Discrete photonic components are increasingly rare, as they are replaced with photonic integrated circuits (PIC). In this sense, we can draw a parallel from the middle of the 20<sup>th</sup> century, and the development of the integrated electronics industry which enabled dense functionality of electrical devices on semiconductor substrates in line with the predictions of Gordon Moore [1]. The emergence of the microprocessor, coupled with steady improvements in fabrication technology has witnessed incredible utility of microelectronics in the past 50 years. The invention of the microprocessor is arguably the most significant technological step in recent history, as it has enabled or accelerated the advancement of nearly every field in science and technology.

The complete integration of photonic devices onto semiconductor substrates will enable a new era of functionality. This next generation of devices will take advantage of existing knowledge in semiconductor manufacturing to dramatically lower cost versus discrete photonic components [2]. Miniaturization will allow for deployment in a wide range of applications previously prohibited by cost or size. These developments will have widespread impact but are largely driven by the demands of the computing industry. After decades of silicon device miniaturization, fundamental limitations are being reached in high performance systems [3] and integrated photonics is needed to help [4,5].

Photonic and computing technology already have an intertwined relationship. The development of optical fiber networks through the 1980's and 1990's has brought high data-rate connections spanning the globe. In recent years both computing power and optical communication bandwidth have steadily improved. This has allowed for a new range of online services which exploit high bandwidth connections to individual homes and businesses. This includes consumer services such as streaming video (e.g. Netflix)

and social networking (e.g. Facebook), but extends to hardware resources as well; from online data storage to processing power itself, providers such as Amazon offer the use of powerful computing systems. These services allow a user to access vast resources, and represent a true paradigm shift in computing, as functionality is not limited by the tool that one owns (or has access to locally). Computing is transforming to an on-demand service or utility, the so called ‘cloud’ model. To enable this model, service providers maintain centralized computing systems collectively referred to as ‘data centers’.

Data centers are very large scale computing systems that consist of thousands of interconnected components. The limitations of a single silicon die necessitate a data center model based on parallel processing as the demand for computation power far outreaches the pace of individual processor performance. It is difficult to comprehend the scale of these systems, even more so as details of individual data centers are generally unavailable for competitive reasons. However data centers may be viewed as a subset of high performance computing, albeit a very large one, and we can look elsewhere to provide some perspective on the scale of state of the art systems. Supercomputers designed for intense science and engineering functions also consist of thousands of interconnected nodes. For example the Titan Cray XK7 system at the Oak Ridge National Laboratory in the United States consists of 18,688 AMD Opteron-6274 16-core CPUs and 18,688 Nvidia Tesla K20X GPUs, giving a grand total of 560,640 cores. Regardless of the systems purpose, be it simulating supernovas or simply stockpiling “selfies” in a data center, the power consumption of computing at this scale is incredible. The Titan supercomputer has a theoretical peak computation power of 27 PetaFlops ( $10^{15}$ ), while consuming over 8 MW of power. To place this in context, producing this electricity requires approximately 95 metric tons of coal per day, or about one train car’s worth. This may be viewed as both an ecological and economical disaster today, but is also a roadblock to future development. The next generation of high performance systems is aimed at achieving exascale computing power ( $10^{18}$  Flops), but the current energy efficiency in terms of Flops/Watt must greatly increase [6,7]. Improving the interconnect

system with photonics is a key ingredient to the next generation of high performance computing.

As data centers scale up in physical size and bandwidth requirements, electrical interconnects have been pushed to their fundamental limits due to their finite electrical resistance. As the length of wire increases, so does the resistance and capacitance, limiting the electrical bandwidth [8]. Transmission lines cannot simply be made thicker to lower resistance due to the “skin” effect, described as follows. For an alternating current in a conductor, as the frequency increases the current density concentrates at the surface, increasing the effective resistance and countering benefits gained from using a thicker wire. Resistive loss in electrical transmission lines limits the maximum bit rate to

$$B \leq B_0 \frac{A}{L^2},$$

where  $B_0 \sim 10^{16}$  bit/s for a resistive-capacitance limited transmission line typically found on a chip,  $A$  is the cross section of the wire and  $L$  is the length [8,9].

Optical technology holds several advantages over electrical interconnects. Optical cabling is not susceptible to electromagnetic interference, and the non-conductive cables simplify electrical design considerations at the system level by isolating components and eliminating potential ground loops. Perhaps the key differentiator from electrical systems is that optical transmission loss is not dependent on modulation rate, thus allowing systems to scale up in both speed of operation and length. Optical dispersion does pose a challenge for long-haul applications but less so for ‘short reach’ data center needs with lengths less than 2 km. Furthermore, increased transmission rates can be accomplished using multiple wavelengths of light propagating along the same fiber simultaneously, which is a scheme known as Wavelength-Division-Multiplexing (WDM).

Optical-based interconnects are rapidly replacing electrical ones in data centers allowing for vast gains in data rate and interconnect length. The first generation of optical interconnects have been designed for an easy transition from electrical connections as

they consist of a fiber optic cable with optical transceiver structures onboard the cable connector. Known as ‘active optical cables’, they can plug into existing electrical connections but maintain high-speed performance over long distance. These cables have been deployed for several years already, with upcoming iterations reaching transfer rates of 100 Gbit/s [10]. Active optical cables will provide benefit to data centers in existence today, but significantly greater progress will be seen when new data centers are constructed which fully utilize the strengths of photonics.

The implementation of optical interconnects may lead to remarkable architectural changes in computing. The concept of a silicon ‘macrochip’ is shown in Figure 1.1, where an array of silicon dies are closely integrated with photonic bridges. Such a system would provide advantages of density, energy efficiency and reduced latency compared to existing multichip arrangements [11].

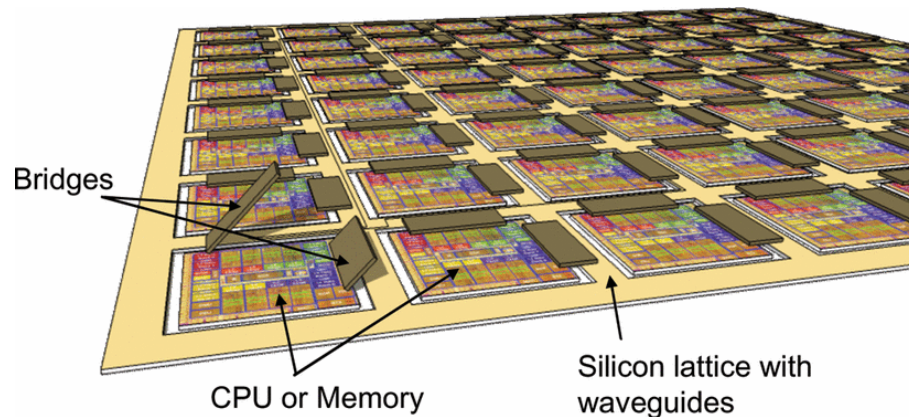


**Figure 1.1 | The ‘macrochip’ concept. A dense integration of multiple silicon dies connected with silicon photonic bridges. Figure reproduced from [11] © 2011 IEEE.**

While high performance computing is perhaps the largest driving force behind integrated optics there are many other areas that can take advantage of photonic integration. Photonic devices have penetrated into every sector of technology, therefore opportunities for integration or miniaturization are plentiful. A partial list of applications includes: gyroscopes [12], mechanical sensors [13], quantum computing [14], glasses-free three-dimensional displays [15], sensing applications for industry and medicine such as glucose monitoring [16] and gas sensing [17]. Laser integration is providing great

advances such as silicon Raman lasers for broad spectrum production [18], laser beam-steering with no moving parts [19] and optical tweezers at the nanoscale [20]. Many of these tools offer exciting opportunities. For example, integrated beam-steering will allow for affordable laser ranging technology (LIDAR), which is a key requirement of self-driving cars and other robotic vision systems.

Many of these devices operate in the optical fiber transmission windows around wavelengths of 1.3  $\mu\text{m}$  and 1.5  $\mu\text{m}$ , as there is a well developed family of optical components. Yet integrated optics will not be limited to this wavelength region as many applications exist further into the infrared spectrum. Mid-infrared photonics (2 - 5  $\mu\text{m}$ ) is an expanding field, and integrated optics can deliver solutions [21].

Most of the aforementioned devices are platform agnostic, meaning that they could be implemented in a variety of material platforms using the same physical principles. Each platform possesses their own strengths and weaknesses in the functionality offered and ease of fabrication. The focus of this thesis is on monolithic silicon photodetectors implemented on the silicon-on-insulator platform.

## **1.2 Silicon photonics as a solution**

### **1.2.1 The strengths of silicon**

Silicon has traditionally been thought of as a poor material for optoelectronic devices. It has an indirect band-gap which severely limits light emission and absorption efficiency. Silicon does not possess a linear electro-optic response (Pockels effect) and has weak second order effects, ruling out modulation with an applied electric field. Furthermore it lacks the adjustable band-gap offered by compound semiconductors such as InGaAs, which greatly increases flexibility for detection and lasing. However there are several strengths of silicon that make up these shortfalls, including the high refractive index contrast and low propagation loss of silicon waveguides.

In the infrared silicon has a refractive index of  $\approx 3.5$  while silicon dioxide is  $\approx 1.5$ , this difference provides a high degree of optical confinement making nanoscale waveguides possible using silicon-on-insulator (SOI). An SOI wafer consists of a silicon handle wafer with a layer of buried oxide underneath a thin surface layer of silicon, which is typically constructed from bonding two wafers together [22]. This process was originally developed for electronics but has become foundational for silicon photonics. With the optical isolation provided by the buried oxide, low loss waveguides can be formed in the thin silicon surface layer. Silicon has an optical band-gap of  $\approx 1100$  nm, and the established telecommunication wavelength regions lie beyond this in the range of 1300 - 1600 nm. Thus the bulk material transmission loss is limited by crystalline defects and impurities, which are not a concern as high quality crystalline silicon is relatively inexpensive. The primary propagation loss associated with silicon waveguides is due to surface roughness. With advanced silicon processing knowledge, this is not a critical problem. Sub-micron waveguides can be routinely made with losses lower than 2 dB/cm [23], which is an acceptable figure for photonic circuits on the order of millimetres in length.

The high resolution lithography available for silicon allows complex structures to be fashioned onto the SOI platform. For efficient on/off chip coupling there are grating structures [24] and nanotapers [25]. The availability of low-loss waveguides provides compact and high quality-factor resonant structures including ring resonators [26], disk resonators [27] and photonic crystal cavities [28]. These resonant structures can be used for on-chip routing, along with arrayed waveguide gratings [29], multimode interferometers [30] and sub-wavelength structures for waveguides and waveguide crossings [31]. These are just a small selection of the wide variety of structures that allow for the control of light on the SOI platform. They are all possible to produce cheaply due to the availability of high quality optical lithography.

The entrenchment of silicon in the semiconductor industry is a primary motivation for silicon photonics. The large wafer sizes and mature manufacturing protocols provide an economic advantage for the platform. Despite the strengths of the SOI platform for

passive devices, there are challenges in the electrical integration of active devices. The building block components that nearly all photonic systems make use of are a light source, a modulator to encode an electrical signal onto an optical carrier wave and a photodetector to convert the optical signal back to an electrical signal. These three components are also the basis for optical interconnects. Various other structures may be required depending on the application but will not be discussed in detail, these include amplifiers [32], thermal controllers [33], variable optical attenuators [34] and optical isolators [35].

### **1.2.2 Lasers**

The most notable absence in the library of available devices is the silicon laser. Silicon has a fundamental limitation for light emission due to its indirect band-gap. Achieving an electrically pumped silicon light source would have tremendous benefit and so there is much work towards this goal but the research developments to date are still far short of application requirements. Silicon nanocrystals can emit light far more efficiently than bulk silicon [36] but their integration into operating devices is troublesome as the crystals are formed within oxide which is a barrier to electrical injection. Silicon Raman lasers have been demonstrated but are not a practical solution for most integrated optics applications as they require a high power optical pump source [18]. Lasing has been demonstrated using germanium grown on silicon waveguides but the efficiency with electrical injection is low, and requires tensile strain [37]. However this is a developing topic and is likely to see further advances. The only remaining solution is one using a hybrid III-V semiconductor on SOI approach. Wafer bonding of III-V semiconductors to silicon waveguides has been demonstrated, and examples of both a Fabry-Perot structure and ring cavity design from Liang *et al.* are shown in Figure 1.2 [38]. While the fabrication of these hybrid devices is quite complex, they offer high optical power and most importantly a high level of integration with the laser directly fabricated on the waveguide.

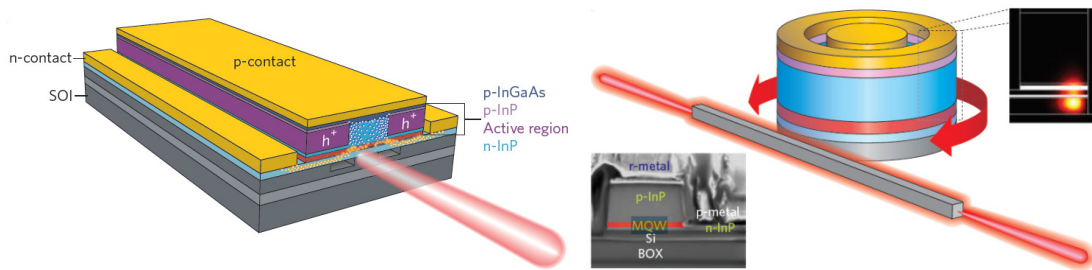


**Figure 1.2 | *Left* - A hybrid silicon Fabry-Perot laser. The waveguide mode extends into the InP region directly above the waveguide. *Right* - A hybrid microring laser with a silicon bus waveguide, the simulated mode is shown in the right inset while an SEM image of the device cross section is shown in the left inset. Figure reproduced from [38] © 2010 NPG.**

Although it would appear that an integrated light source is a required component, in fact the flexibility offered by co-packaging a discrete laser device can be significant. An SOI chip with a fiber coupled from a vertical-cavity surface-emitting laser (VCSEL) or quantum-dot frequency-comb laser [39] for example, can serve a variety of applications where complete integration is not required.

### 1.2.3 Modulation

With regard to optical modulation, silicon is again prey to its fundamental limitations. In general, high-speed optical modulators typically rely on the Pockels effect, where the application of an electric field to a crystalline material alters its refractive index. For silicon, the Pockels effect is not present in bulk material due to the centro-symmetry of the crystalline structure. This limitation has led to the development of hybrid SOI approaches, as with the laser, where III-V semiconductor materials are bonded on silicon. Additionally there are polymer based modulators, where an organic material is spun onto a silicon waveguide [40]. Both of these approaches offer excellent performance, but they lag far behind monolithic silicon devices in terms of manufacturability. III-V hybrid devices require wafer bonding, and polymer based devices are subject to the processing durability of the chosen material with thermal degradation as a common issue. To make a practical modulator in silicon an entirely different approach is needed to introduce a phase change.

A landmark paper in silicon photonics was published in 1987 which described the relationship between refractive index changes and the concentration of free carriers in silicon [41]. This work laid out the fundamentals needed to develop silicon optical modulators without relying on the Pockels effect. By using a  $p$ - $n$  diode which crosses a waveguide, the free carrier concentration can be modified either by injection or depletion, allowing for the direct control of refractive index and therefore phase modulation. This was demonstrated, for example, by Xu *et al.* and is shown in Figure 1.3, describing a silicon ring resonator with a  $p$ - $n$  junction integrated on the ring [42].

Due to the complex manufacturability and cost issues of hybrid structures, much of the recent attention has been directed towards carrier based modulation and the monolithic silicon approach. Using modern silicon foundries, sub-micron waveguides and tightly controlled doping profiles, the speed of silicon modulators has been pushed above 40 Gbit/s. Figure 1.4 shows a 40 Gbit/s eye diagram, accompanied by a schematic cross-section of the silicon modulator developed by Gardes *et al.* [43]. Unlike the ‘instantaneous’ Pockels effect, employing carriers involves a speed limitation, therefore shorter drift distances and optimally placed dopant greatly influence device functionality.

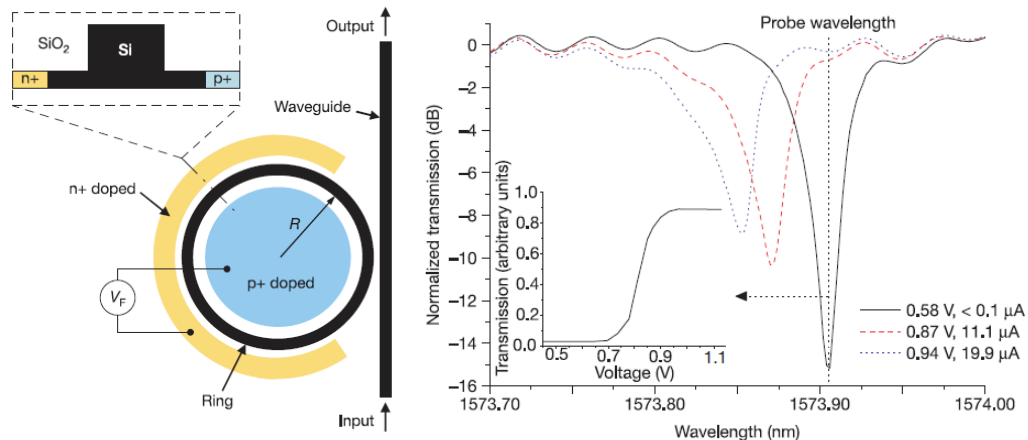


**Figure 1.3 | The first reported silicon modulator using a ring resonator. *Left* - A schematic diagram of the ring resonator device. *Right* - A transmission spectrum of the bus waveguide, as the voltage increases there is a blueshift in resonance due to increased carrier concentration. Figure reproduced from [42] © 2005 NPG.**

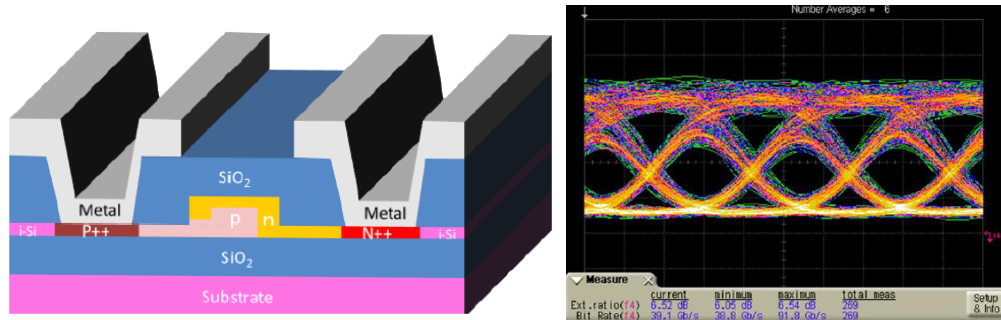


**Figure 1.4 | Left – A schematic cross-section of a silicon Mach-Zehnder modulator. The  $p$ - $n$  junction in the waveguide uses a wrap-around geometry to increase the overlap of the depletion region with the optical mode. Right - A 40 Gb/s eye diagram. Reproduced from [43] © 2011 Optical Society of America.**

While silicon modulators do not surpass the performance characteristics of hybrid approaches, they will likely win over system designers. The higher cost associated with fabrication of the hybrid devices may not be worth the marginal performance increase.

#### 1.2.4 Photodetection: The hybrid approach

Silicon waveguide photodetectors face a fundamental challenge; to absorb light beyond the optical band-gap of silicon at the telecommunications wavelengths. Due to the conflict of using the same material for both a low loss waveguide and a highly absorptive photodetector, hybrid approaches have dominated the field. It is possible to bond III-V materials to silicon waveguides in the same fashion as is done for lasing structures, but germanium based detectors have dominated research efforts due their relative simplicity. Although germanium differs with silicon in its lattice constant, epitaxial growth of germanium on silicon has been achieved. This has allowed for several different approaches for integrating detectors on silicon, including a germanium  $p$ - $i$ - $n$  diode with a bandwidth of 42 GHz, where a slab of germanium is grown at the end of a silicon waveguide [44]. A schematic diagram and micrograph of this detector is shown in Figure 1.5.

Avalanche detectors have also been explored. A gain-bandwidth product of 340 GHz was achieved with epitaxial growth of germanium on silicon [45]. A germanium

avalanche detector has also been incorporated directly onto a silicon waveguide with a rapid melting growth technique by Assefa *et al.* [46]. In this case, metal-semiconductor-metal Schottky diodes were formed directly in a germanium layer with tungsten plugs. The detector makes use of evanescent coupling to achieve a 300 GHz gain-bandwidth product and 40 Gbit/s operation.

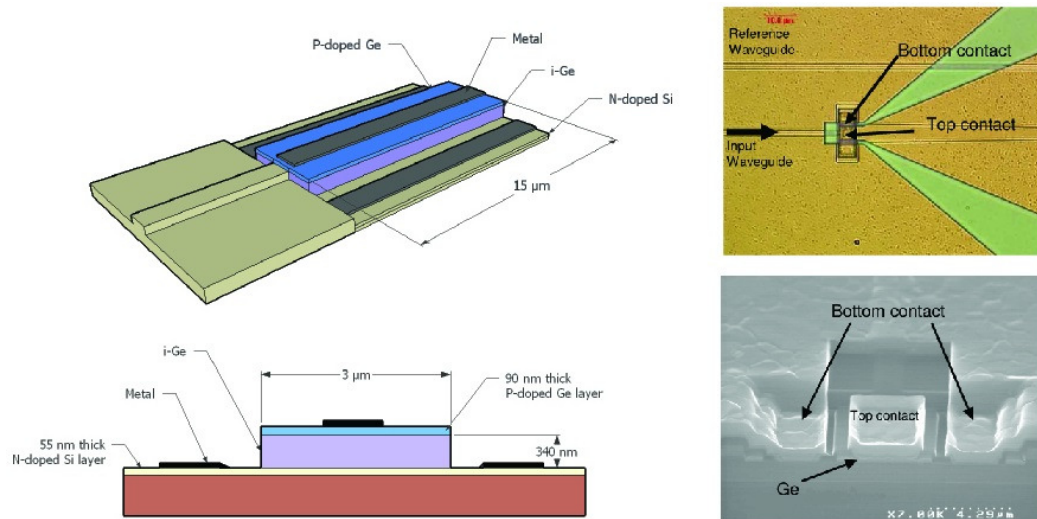


**Figure 1.5 | A 42 GHz germanium on silicon *p-i-n* photodiode. Left - A schematic diagram, germanium was grown directly on the silicon at the end of a rib waveguide. Upper right - A micrograph of the detector. Bottom right - An SEM image of the detector. Reproduced from [44] © 2009 Optical Society of America.**

The main drawback of germanium integrated photodetectors lies with the fabrication requirements. Epitaxial growth can result in a poor interface with the silicon which increases device leakage current. Also, the optical absorption of germanium begins to “roll-off” at wavelengths approaching 1570 nm, so for longer wavelengths towards the mid-infrared germanium becomes a poor option.

These hybrid approaches to detection are continually maturing in their attempt to fill the needs of silicon photonic circuits. However the gap between the research laboratory and applied technology is still large and the aforementioned manufacturability issues will remain for the foreseeable future.

### 1.2.5 Challenges of integration

It is clear that the miniaturization of optical technology through silicon photonics will provide many benefits. Existing optical technology is relatively expensive and large, but silicon photonics can provide cost savings and miniaturization. Surveying the state of the art shows a large list of devices proven in the research lab, and a much reduced list deployed in application. For medium length scale applications, such as server to server links from 1 – 1000 metres inside a data center, commercial products are deployed. In this application size requirements are less stringent and therefore the level of integration can be low (i.e. co-packaging of multiple chips).

Photonic links are also demanded at shorter scales, including links from a microprocessor to memory on-board, or looking further into the future, core to core links within a microprocessor. These small scale applications will require a higher level of integration due to the limited space and power constraints. The main obstacle is that the fabrication processes for the individual photonic components are not congruent, and therefore creating a single PIC with multiple complex structures (i.e. III-V laser + germanium detector) can inflate the fabrication cost.

A commonly used phrase in the silicon photonics community is that a device is ‘compatible with CMOS fabrication processes’. While this is true in most cases in that devices are made using the same equipment that is used in the microelectronics industry, in a certain context it can be a disingenuous statement as it suggests a photonic circuit can share a die with an electronic one. This is far from the current reality. The process flows for electronic and photonic circuits are not the same and require different optimizations. A primary difference is the top silicon thickness in SOI wafers where optical devices require a greater thickness (compared to electronic circuit fabrication) to ensure low loss waveguides. Efforts have been made to integrate photonic circuits into unmodified industrial CMOS processes [47,48]. Waveguides, modulators and filters have been created alongside transistors, but these optical devices fall short of what is achievable in a process flow optimized for silicon photonics. This leaves questions as to how ultimately

photonic chips will be integrated with electronics, and if they will ever reside on the same die. In the short term, co-packaging processes have been developed, where distinct electronic and photonic ICs are packaged together. This can be done with a flip-chip process, where the face of the chips are placed together. This has the advantage of shortening any links between the two chips. Alternatively the chips can simply be placed side by side with wire-bonded connections. For some processes multiple photonic chips will be needed, and therefore precise alignment methods are required [49]. Connecting waveguides from chip to chip may be accomplished using grating couplers in the flip-chip method, or alternatively in a side by side configuration where one solution involves polymer waveguides to join adjacent chips [50].

With the large variety of devices demonstrated and various fabrication and packaging methods any sort of standardization may take some time to occur. This is bad news for those interested in applying integrated photonic devices in larger systems. However there are now efforts to simplify development for designers and allow for wider access to advanced fabrication facilities [51, 52].

### **1.2.6 Multi-project wafers and the ‘fabless’ approach**

The use of CMOS manufacturing for silicon photonics can provide a cost advantage but only on a large scale. CMOS facilities involve a large capital investment and require a high production volume to derive cost-advantage. Even in the case of outsourced fabrication, the cost for a low volume of devices remains high due to the fixed cost of the lithography mask set, process setup and verification. CMOS chips are only delivered cheaply once these fixed costs are covered, and a high volume of wafers can be processed for relatively low variable costs. Since most academic researchers and new businesses do not require volume production, these costs are unaffordable. This has led to the silicon photonics community attempting to repeat the success of early CMOS development with the use of multi-project wafers (MPW). MPWs are shared fabrication runs where users pay for their own share of the die, allowing small projects to be developed with leading edge fabrication services in a ‘pay-as-you-go’ manner. Lowered cost is not the only

advantage with MPWs, they have an established set of design rules and a repeatable fabrication process providing for guaranteed performance of building block structures. Their disadvantage is that the process is locked such that variation from the MPW is not permitted.

For academic researchers the MPW model is essential, as the state-of-the-art in silicon photonics has mostly moved past what is achievable at university funded clean rooms. MPW fabrication has enabled a sizeable portion of recent research in silicon photonics, including the contents of this thesis. Figure 1.6 is a photograph of a wafer received through a shared fabrication run at a silicon foundry. These services allow researchers to focus on the device design, rather than the increasing difficulties of modern silicon fabrication.

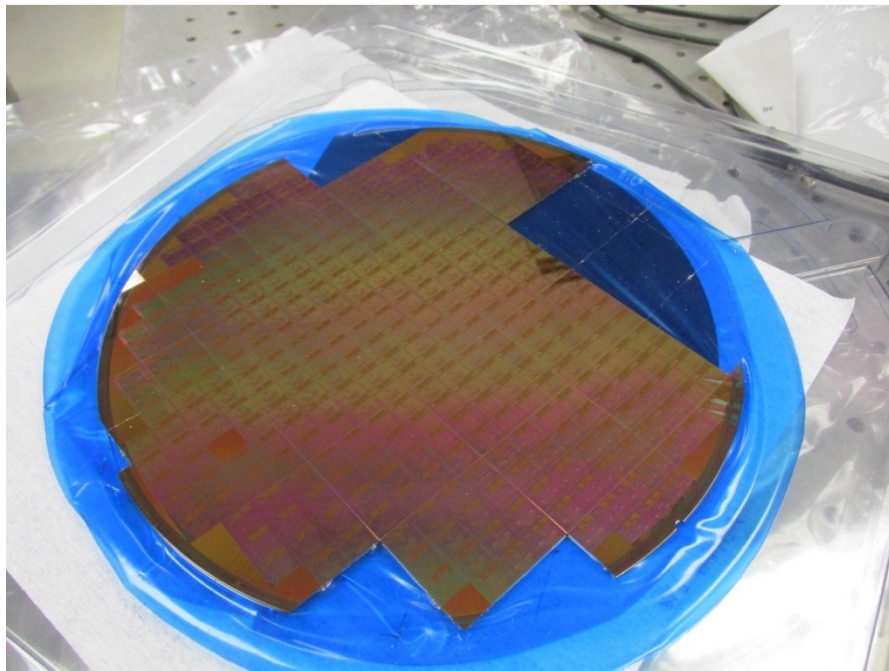


**Figure 1.6 | A wafer of silicon photonic devices used in this thesis.**

For the private sector MPWs are enablers for small companies to establish themselves as a ‘fabless’ producer, where design and testing is done in house but fabrication is outsourced. Prototyping through an MPW can accelerate development, as once the device is ready for a production run the volume can be easily scaled up as the fabrication

processes are also in place. This approach avoids switching fabrication facilities and the risk of new process conditions.

Even for larger companies the fabless approach to device manufacturing remains attractive. Consolidation is the general industry trend as even long time producers (e.g. IBM in 2014) have divested from in-house fabrication to focus on development of products. There now exists only a handful of major companies in the business of chip fabrication (e.g. TSMC, Intel, Global Foundries, Samsung).

## 1.3 Monolithic silicon detectors

### 1.3.1 Defect-based detection

While germanium-based detectors have offered the most compelling solution in terms of performance, their fabrication comes at a cost of added complexity. This has motivated the development of monolithic silicon detectors, which primarily include bulk defect-based devices and surface-state defect devices. Such detectors absorb sub-band-gap light through defect mediated processes. While developing an all-silicon high-speed photoreceiver which matches hybrid performance is the ultimate goal, silicon detectors can also fulfil other roles such as power monitoring and low speed detection for spectrometers or sensors. There are several ways in which monolithic silicon detectors for sub-band-gap light have been constructed and these will be briefly reviewed here.

Defect-based photodetectors have most extensively been studied by employing ion implantation to introduce damage to the silicon crystal structure. The advantage of ion implantation is that the concentration of defects can be controlled and delivered where desired. The absorption can be increased within a photodiode while leaving the remainder of the silicon waveguide highly transparent. Detectors created with this method have been explored at McMaster University, beginning with a *p-i-n* rib waveguide detector created by Knights *et al.* [53]. Further work by Doyle *et al.* and Logan *et al.* integrated these photodiodes within ring resonators fabricated with optical lithography and electron-beam

lithography, respectively [54, 55]. A photodetector within a ring resonator increases the responsivity due to the optical intensity build up while allowing the device to maintain a compact footprint. The resonator also acts as a filter, allowing wavelength selection for use in either a wavelength division multiplexing scheme or a spectrometer device.

While these devices demonstrated the principles of operation, the high-speed response was not characterized. To compete with hybrid solutions for deployment within optical interconnects systems a fast, low bias and highly responsive diode is needed. A step towards this goal was made by Geis *et al.* who fabricated a high-speed silicon photodetector with lattice defects introduced using ion implantation [56]. The authors reported a 35 GHz bandwidth at 10 V reverse bias. Further high-speed characterization of silicon photodiodes have shown error-free operation at 10 Gbit/s [57].

### **1.3.2 Long wavelength detection**

Much of the research effort in silicon photonics has focused on wavelengths from 1300 to 1550 nm, a range which makes up the commonly used transmission windows for telecommunications. Defect mediated detection has been demonstrated at wavelengths of 1744 nm [58], 1900 nm and 2200 nm by Souhan *et al.* [59, 60] and from 2000 nm and 2500 nm in large cross-section waveguides by Thomson *et al.* [61].

### **1.3.3 Surface-state detection & other approaches**

While bulk defects introduced from ion implantation have been shown to greatly enhance responsivity and enable useful devices, photodetection can be achieved in their absence. Defects present at the surface of crystalline silicon have been shown to absorb light. Baehr-Jones used metal contacted to the wings of an undoped silicon waveguide and demonstrated optical detection [62]. More recently, a capacitive sensing scheme was demonstrated which can measure absorption without direct electrical contact with the waveguide [63].

An unconventional method for detection is through two-photon absorption, a non-

linear optical effect where two sub-band-gap photons are simultaneously absorbed if their combined energy is greater than the band-gap. This phenomenon has allowed for detection in resonant based devices due to the build-up of high optical intensity. The effect has been observed in microdisk resonators [64] but can occur in any resonant structure including microrings or photonic crystal cavities [65]. This approach is generally less desirable as the responsivity of the detector varies with input power.

Polycrystalline silicon is another material system useful for defect-based detection. A polycrystalline material is composed of individual crystal grains or crystallites, each covered with an imperfect surface which can absorb light. Although the material possesses higher loss than mono-crystalline silicon it can be used for waveguides and has been shown to function as a detector at 1550 nm [66]. The desire to use this material comes from its manufacturability, as polycrystalline material can be produced with deposition methods on various substrates.

#### **1.3.4 Resonant detectors**

One limiting factor for any defect detector is the relatively low absorption of the damaged silicon. Germanium diodes can produce adequate absorption on a length scale of tens of microns where equivalent absorption in a silicon photodiode may need millimetres of length. This may be an unwieldy chip area to occupy for a single photodetector, and such a large area would impact chip cost and limit high-speed operation.

Defect based detectors have been developed in both resonant [54,55] and non-resonant configurations [56-60]. Resonant detectors offer the advantage of wavelength selectivity and increased responsivity per chip area occupied. Since the diode itself is a much shorter length, capacitance and leakage current are also reduced. Finally, resonant devices have the advantage of wavelength selectivity built into the device. For a wavelength division multiplexed system this saves additional chip area as the need for a separate filter is avoided.

Resonant detectors do however introduce added complexity in operation. Although

the short diode length aids in high-speed operation, they must contend with a limitation imposed by the photon cavity lifetime. Their operation is also sensitive to refractive index fluctuations and in a wavelength division multiplexing scheme, each channel must operate on a specific wavelength. In real conditions the surrounding temperature of a device will see fluctuation due to dissipated heat and environmental variation. Therefore the resonator must have real time adjustment of its resonance condition. Tuning can be performed by the integration of thermal heaters, capable of responding to these slowly varying conditions. Additional instabilities arise with a high intensity of light in the diode, resulting in a large photocurrent generated with rapidly changing carrier concentrations. This dynamic behaviour can cause small fluctuations of the index of refraction, perturbing the resonator.

## **1.4 Contributions in thesis**

The novel contributions outlined in this thesis build towards monolithic silicon detector development. In chapter 3 defect based resonant detectors are discussed. This includes an experimental study of defects in ring resonators to determine the refractive index change introduced; both real and imaginary. Also in chapter 3 are experimental results from resonant photodetectors, including high-speed operation in which a limitation in bandwidth is explored. Chapter 4 presents experimental results from avalanche photodetectors, which includes a significant improvement in sensitivity over previously reported devices as well as first demonstration of high-speed, large signal operation. Chapter 5 presents results from a monolithic silicon detector operating with surface-state based absorption. This detector has simple fabrication steps and will find use as a power monitor, with potential uses in sensing applications. A comparison in performance of detectors using bulk or surface defects is also presented. Chapter 6 presents results for avalanche detectors at wavelengths beyond the standard telecommunications windows. The detectors show sensitivity up to 2.5  $\mu\text{m}$  and are capable of operation at 20 Gbit/s which represents the fastest large signal demonstration of a defect detector to date. The thesis concludes with a summary and discussion of suggested future work.

## 1.5 Publications

The contributions of this thesis have been published in respected research journals and are listed here chronologically:

Ackert, J.J. *et al.* Defect-mediated resonance shift of silicon-on-insulator racetrack resonators. *Opt. Express* **19(13)**, 11969-11976 (2011).

Ackert, J.J. *et al.* Silicon-on-insulator microring resonator defect-based photodetector with 3.5-GHz bandwidth. *J. Nanophotonics* **5(1)**, 059507-059507 (2011).

Ackert, J.J. *et al.* Photodetector for 1550 nm formed in silicon-on-insulator slab waveguide. *Electron. Lett.* **48(18)**, 1148-1150 (2012).

Ackert, J.J. *et al.* 10 Gbps silicon waveguide-integrated infrared avalanche photodiode. *Opt. Express* **21(17)**, 19530-19537 (2013).

Ackert, J.J. *et al.* Monolithic silicon waveguide photodiode utilizing surface-state absorption and operating at 10 Gb/s. *Opt. Express* **22(9)**, 10710-10715 (2014).

At the date of submission of this thesis, a manuscript describing high-speed 2  $\mu\text{m}$  photodetectors has been accepted in *Nature Photonics*.

This research has also been presented at international scientific conferences:

Ackert, J.J. *et al.* Silicon-on-insulator Racetrack resonator tuning via Ion implantation. *Proceedings of IEEE Group IV Photonics* P1.30 (2011).

Ackert, J.J. *et al.* Defect enhanced silicon-on-insulator microdisk photodetector. *Optical Interconnects Conference* TuP10. Page 76-77 (2012).

Ackert, J.J. *et al.* Waveguide integrated silicon avalanche photodetectors. *Proceedings of SPIE* 8629, Silicon Photonics VIII, 86290R (2013).

Ackert, J.J. *et al.* 10 Gb/s bit error free performance of a monolithic silicon avalanche

waveguide integrated photodetector. *Optical Fiber Communication Conference Th4C.3* (2014).

## 1.6 Statement of work

The work in this thesis involved several collaborators whose contributions were as follows.

In chapter 3 a study of ion implantation in passive ring resonators was a collaboration with Raha Vafaei and Lukas Chrostowski at the University of British Columbia in Vancouver, BC. The initial device design and fabrication was completed by UBC, along with contributions to discussion and interpretation of results following the ion implantation experiment.

Further work in chapter 3 involved high-speed measurements of resonant photodiodes. The experimental work was done together with Marco Fiorentino at Hewlett Packard Laboratories in Palo Alto, CA, USA.

In chapter 4 and 5 high-speed measurements of photodiodes were performed together with Abdullah Karar and John Cartledge of Queen's University in Kingston, ON. Dixon Paez of McMaster contributed electrical simulations which appeared in a journal article but not in this thesis.

In chapter 6, the devices were characterized together with Dave Thomson and Li Shen at the University of Southampton, Southampton, UK. This included high-speed measurements and variable wavelength continuous-wave results.

All of these collaborators were co-authors on journal publications and contributed to the discussion of results.

## References

1. Moore, G. Cramming more components onto integrated circuits. *Electronics* **38(8)**, 114-117 (1965).
2. Streshinsky, M. *et al.* The Road to Affordable, Large-Scale Silicon Photonics. *Opt. Photon. News* **24(9)**, 32-39 (2013).
3. Markov, I.L. Limits on fundamental limits to computation. *Nature* **512(7513)**, 147-154 (2014).
4. Ashgari, M. and Krishnamoorthy, A.V. Silicon photonics: energy-efficient communication. *Nature Photon.* **5(5)**, 268-270 (2011).
5. Beausoleil, R.G. Large-Scale integrated photonics for high-performance interconnects. *ACM J. Emerg. Technol.* **7(2)** Article 6 (2011).
6. Shalf, J., Dosanjh, S. and Morrison, J. Exascale computing technology challenges. *High Performance Computing for Computational Science–VECPAR 2010. Springer Berlin Heidelberg*, 1-25 (2011).
7. Kodi, A.K., Neel, B. and Brantley, W. Photonic Interconnects for Exascale and Datacenter Architectures. *IEEE Micro* **34(5)**, 18-30 (2014).
8. Miller, D.A.B. and Ozaktas, H.M. Limit to the bit-rate capacity of electrical interconnects from the aspect ratio of the system architecture. *J. Parallel Distr. Com.* **41(1)**, 42-52 (1997).
9. Miller, D.A.B. Device requirements for optical interconnects to silicon chips. *P. IEEE* **97(7)**, 1166-1185 (2009).
10. Molex Inc. <http://www.molex.com>
11. Cunningham, J.E. *et al.* Integration and Packaging of a Macrochip With Silicon Nanophotonic Links. *IEEE J. Sel. Top. Quantum Electron.* **17(3)**, 546-558 (2011).
12. Ciminelli, C. *et al.* High performance InP ring resonator for new generation monolithically integrated optical gyroscopes. *Opt. Express* **21(1)**, 556-564 (2013).
13. Lee, C. and Thillaigovindan, J. Optical nanomechanical sensor using a silicon photonic crystal cantilever embedded with a nanocavity resonator. *Appl. Optics* **48(10)**, 1797-1803 (2009).

14. Hausmann, B.J.M. *et al.* Integrated diamond networks for quantum nanophotonics. *Nano Lett.* **12(3)**, 1578-1582 (2012).
15. Fattal, D. *et al.* A multi-directional backlight for a wide-angle, glasses-free three-dimensional display. *Nature* **495(7441)**, 348-351 (2013).
16. Shao, M.W. *et al.* Silicon nanowire sensors for bioanalytical applications: glucose and hydrogen peroxide detection. *Adv. Funct. Mater.* **15(9)**, 1478-1482 (2005).
17. Robinson, J.T., Chen, L. and Lipson, M. On-chip gas detection in silicon optical microcavities. *Opt. Express* **16(6)**, 4296-4301 (2008).
18. Rong, H. *et al.* A continuous-wave Raman silicon laser. *Nature* **433**, 725-728 (2005).
19. Doylend, J.K. *et al.* Two-dimensional free-space beam steering with an optical phased array on silicon-on-insulator. *Opt. Express* **19(22)**, 21595-21604 (2011).
20. Li, M. *et al.* Harnessing optical forces in integrated photonic circuits. *Nature* **456(7221)**, 480-484 (2008).
21. Soref, R.A. Mid-infrared photonics in silicon and germanium. *Nature Photon.* **4(8)**, 495-497 (2010).
22. Bruel, M. Silicon on insulator material technology. *Electron. Lett.* **31(14)**, 1201-1202 (1995).
23. Vivien, L. *et al.* Comparison between strip and rib SOI microwaveguides for intra-chip light distribution. *Opt. Mater.* **27**, 756-762 (2005).
24. Halir, R. *et al.* Continuously apodized fiber-to-chip surface grating coupler with refractive index engineered subwavelength structure. *Opt. Lett.* **35(19)** (2010).
25. Almeida, V.R., Panepucci, R.R. and Lipson, M. Nanotaper for compact mode conversion. *Opt. Lett.* **28(15)**, 1302-1304 (2003).
26. Xu, Q., Fattal, D. and Beausoleil, R.G. Silicon microring resonators with 1.5 $\mu\text{m}$  radius. *Opt. Express* **16(6)** (2008).
27. Soltani, M., Yegnanarayanan, S. and Adibi, A. Ultra-high Q planar silicon microdisk resonators for chip-scale silicon photonics. *Opt. Express* **15(8)** 4694-4704 (2007).

28. Zain, A.R.M. *et al.* Ultra high quality factor one dimensional photonic crystal/photonic wire micro-cavities in silicon-on-insulator (SOI). *Opt. Express* **16(16)**, 12084-12089 (2008).
29. Pathak, S. *et al.* Optimized Silicon AWG With Flattened Spectral Response Using an MMI Aperture. *J. Lightwave Technol.* **31(1)**, 87-93 (2013).
30. Thomson, D.J. *et al.* Low loss MMI couplers for high performance MZI modulators. *IEEE Photon. Technol. Lett.* **22(20)**, 1485-1487 (2010).
31. Sanchis, P. *et al.* Highly efficient crossing structure for silicon-on-insulator waveguides. *Opt. Lett.* **34(18)**, 2760-2762 (2009).
32. Park, H. *et al.* A hybrid AlGaInAs–silicon evanescent amplifier. *IEEE Photon. Technol. Lett.* **19(4)**, 230-232 (2007).
33. Dong, P. *et al.* Thermally tunable silicon racetrack resonators with ultralow tuning power. *Opt. Express* **18(19)**, 20298-20304 (2010).
34. Park, S. *et al.* Influence of carrier lifetime on performance of silicon pin variable optical attenuators fabricated on submicrometer rib waveguides. *Opt. Express* **18(11)**, 11282-11291 (2010).
35. Tzuang, L.D. *et al.* Non-reciprocal phase shift induced by an effective magnetic flux for light. *Nature Photon.* **8(9)**, 701-705 (2014).
36. Pavesi, L. and Turan, R. Silicon nanocrystals: fundamentals, synthesis and applications. *John Wiley & Sons* (2010).
37. Liu, J. *et al.* Ge-on-Si laser operating at room temperature. *Opt. Lett.* **35**, 679-681 (2010).
38. Liang, D. and Bowers, J.E. Recent progress in lasers on silicon. *Nature Photon.* **4(8)**, 511-517 (2010).
39. Wojcik, G.L. *et al.* A single comb laser source for short reach WDM interconnects. *Proc. SPIE 7230, Novel In-Plane Semiconductor Lasers VIII, 72300M* (2009).
40. Hochberg, M. *et al.* Towards a millivolt optical modulator with nano-slot waveguides. *Opt. Express* **15(13)**, 8401-8410 (2007).

41. Soref, R.A. and Bennett, B.R. Electrooptical effects in silicon. *IEEE J. Quantum Elec.* **23(1)**, 123-129 (1987).
42. Xu, Q. *et al.* Micrometre-scale silicon electro-optic modulator. *Nature* **435(7040)**, 325-327 (2005).
43. Gardes, F.Y. *et al.* 40 Gb/s silicon photonics modulator for TE and TM polarisations. *Opt. Express* **19(12)**, 11804-11814 (2011).
44. Vivien, L. *et al.* 42 GHz pin Germanium photodetector integrated in a silicon-on-insulator waveguide. *Opt. Express* **17(8)**, 6252-6257 (2009).
45. Kang, Y. *et al.* Monolithic germanium/silicon avalanche photodiodes with 340 GHz gain–bandwidth product. *Nature Photon.* **3(1)**, 59-63 (2008).
46. Assefa, S., Xia, F. and Vlasov, Y.A. Reinventing germanium avalanche photodetector for nanophotonic on-chip optical interconnects. *Nature* **464(7285)**, 80-84 (2010).
47. Orcutt, J.S. *et al.* Open foundry platform for high-performance electronic-photonic integration. *Opt Express* **20(11)**, 12222-12232 (2012).
48. Orcutt, J.S. *et al.* Nanophotonic integration in state-of-the-art CMOS foundries. *Opt. Express* **19(3)**, 2335-2346 (2011).
49. Krishnamoorthy, A.V. *et al.* Optical Proximity Communication With Passively Aligned Silicon Photonic Chips. *IEEE J. Quantum Elec.* **45(4)**, 409-414, (2009).
50. Lindenmann, N. *et al.* Photonic wire bonding: a novel concept for chip-scale interconnects. *Opt. Express* **20(16)**, 17667-17677 (2012).
51. Institute of Microelectronics, Singapore. <http://www.a-star.edu.sg/ime/>
52. IMEC, Leuven Belgium. <http://www.epixfab.eu/technologies/imec-siphotonics>
53. Knights, A.P. *et al.* Silicon-on-insulator waveguide photodetector with self-ion-implantation-engineered-enhanced infrared response. *J. Vac. Sci. Technol. A.* **24**, 783-786 (2006).
54. Doylend, J.K., Jessop, P.E. and Knights, A.P. Silicon photonic resonator-enhanced defect-mediated photodiode for sub-bandgap detection. *Opt. Express* **18(14)**, 14671–14678 (2010).

55. Logan, D.F. *et al.* Defect-enhanced Silicon-on-insulator Waveguide Resonant Photodetector With High Sensitivity at 1.55  $\mu\text{m}$ . *IEEE Photon. Technol. Lett.* **22(20)**, 1530 (2010).
56. Geis, M.W. *et al.* Silicon waveguide infrared photodiodes with  $> 35$  GHz bandwidth and phototransistors with  $50 \text{ AW}^{-1}$  response. *Opt. Express* **17(7)**, 5193-5204 (2009).
57. Grote, R.R. *et al.* 10 Gb/s Error-Free Operation of All-Silicon Ion-Implanted-Waveguide Photodiodes at 1.55. *IEEE Photon. Technol. Lett.* **25(1)**, 67-70 (2013).
58. Geis, M.W. *et al.* CMOS-compatible all-Si high-speed waveguide photodiodes with high responsivity in near-infrared communication band. *IEEE Photon. Technol. Lett.* **19(3)**, 152-154 (2007).
59. Souhan, B. *et al.* Error-Free Operation of an All-Silicon Waveguide Photodiode at 1.9 $\mu\text{m}$ . *IEEE Photon. Technol. Lett.* **25(21)**, 2031-2034 (2013).
60. Souhan, B. *et al.* Si<sup>+</sup>-implanted Si-wire waveguide photodetectors for the mid-infrared. *Opt. Express* **22(22)**, 27415-27424 (2014).
61. Thomson, D.J. *et al.* Optical detection and modulation at 2 $\mu\text{m}$ -2.5  $\mu\text{m}$  in silicon. *Opt. Express* **22(9)**, 10825-10830 (2014).
62. Baehr-Jones, T., Hochberg, M. and Scherer, A. Photodetection in silicon beyond the band edge with surface states. *Opt. Express* **16(3)**, 1659-1668 (2008).
63. Grillanda, S. Non-invasive monitoring and control in silicon photonics using CMOS integrated electronics. *Optica* **1(3)**, 129-136 (2014).
64. Chen, H. and Poon, A. W. Two-photon absorption photocurrent in pin diode embedded silicon microdisk resonators. *Appl. Phys. Lett.* **96(19)**, 191106 (2010).
65. Bravo-Abad, J., Ippen, E.P. and Soljačić, M. Ultrafast photodetection in an all-silicon chip enabled by two-photon absorption. *Appl. Phys. Lett.* **94(24)**, 241103 (2009).
66. Preston, K. *et al.* Waveguide-integrated telecom-wavelength photodiode in deposited silicon. *Opt. Lett.* **36(1)**, 52-54 (2011).

# Chapter 2 Background

## Overview

This chapter is divided into five subject areas most relevant to this thesis. Section 2.1 deals with optical absorption, section 2.2 presents background on the  $p$ - $n$  junction and photodiodes. An overview of avalanche photodiodes is presented in section 2.3. Section 2.4 covers the theory of ring resonators. Finally, section 2.5 provides a brief outline of high-speed measurement techniques.

Silicon photonics is the synthesis of a wide range of physics and technology, and thus there are some notable omissions to content in this chapter. Optical waveguide theory is not covered in any detail, as this thesis involves single mode silicon-on-insulator (SOI) waveguides which have been extensively studied and described previously. For a general treatment on the fundamentals of optical waveguides the reader may refer to *Integrated optics: theory and technology* by Hunsperger [1] and *Fundamentals of optical waveguides* by Okamoto [2]. Silicon fabrication technology is omitted as all devices in this thesis were developed with multi-project wafers that employed established CMOS processes. If the reader is unfamiliar with this subject matter they may refer to *Silicon VLSI Technology* by Plummer [3].

## 2.1 Optical absorption

It is useful to describe the phenomenon of optical absorption in matter before discussing the special case of silicon, a semiconductor material. Optical absorption is a general term describing a set of physical processes by which a photon incident on a target is converted to another form of energy. We will begin with the classical treatment of electromagnetic waves interacting with a dipole. This results in the general behaviour of the real and imaginary parts of the refractive index as a function of frequency. Further detail of this treatment can be found in *Introduction to Electrodynamics* by Griffiths [4].

### 2.1.1 The frequency dependence of refractive index

In a non-conducting medium, the electric permittivity  $\epsilon$  describes the refractive index by  $n = \sqrt{\epsilon}$ . The permittivity is frequency dependent and by exploring this dependency we can gain insight into the nature of absorption. The following treatment is valid for a non-conducting material with bound charge only.

Light interaction with non-conducting matter can be modelled by the interaction of electrons (bound to atoms) with the electric field of a propagating electromagnetic wave. For small electron displacements their binding force can be given by the spring relationship

$$F = -m\omega_0^2 x, \quad (2.1)$$

where  $m$  is the electron mass,  $\omega_0$  is the natural frequency of the oscillator and  $x$  is the displacement. The electric field constitutes a driving force, and there exists a damping force due to radiation, which are described by Eq. (2.2). This model is not fully physical but for small displacement values (low intensity light) this is a useful form;

$$F_{driving} = qE_0 \cos(\omega t) \quad F_{damping} = -m\gamma \frac{dx}{dt}, \quad (2.2)$$

where  $\omega$  is the angular frequency of the electromagnetic field,  $q$  is the electron charge,  $E_0$  is the amplitude of the electric field and  $\gamma$  is the damping constant. Writing Newton's second law, this describes a damped harmonic oscillator;

$$m \frac{d^2 x}{dt^2} + m\gamma \frac{dx}{dt} + m\omega_0^2 x = qE_0 \cos(\omega t). \quad (2.3)$$

The solution to this equation written in the complex form is

$$\tilde{x}(t) = \frac{q^2/m}{\omega_0^2 - \omega^2 - i\gamma\omega} E_0 e^{-i\omega t}. \quad (2.4)$$

The dipole moment is given by  $\tilde{p} = q\tilde{x}(t)$ , therefore the polarization  $P$  over some volume can be expressed as a summation over  $f_j$  electrons with resonant frequency  $\omega_j$  and damping  $\gamma_j$  in each of  $N$  molecules;

$$\tilde{\mathbf{P}} = \frac{Nq^2}{m} \left( \sum_j \frac{f_j}{\omega_j^2 - \omega^2 - i\gamma_j\omega} \right) \tilde{\mathbf{E}}. \quad (2.5)$$

The complex polarization can be expressed in terms of the complex electric field  $\tilde{\mathbf{E}}$  and the complex susceptibility,  $\tilde{\chi}_e$ , as  $\tilde{\mathbf{P}} = \epsilon_0 \tilde{\chi}_e \tilde{\mathbf{E}}$ . With Eq. (2.5) and the relation for complex permittivity  $\tilde{\epsilon} = \epsilon_0 (1 + \tilde{\chi}_e)$ , we can represent the complex dielectric constant as

$$\tilde{\epsilon} = 1 + \frac{Nq^2}{m\epsilon_0} \sum_j \frac{f_j}{\omega_j^2 - \omega^2 - i\gamma_j\omega}. \quad (2.6)$$

For a dispersive medium, a travelling plane wave is described as

$$\tilde{\mathbf{E}}(z, t) = \tilde{\mathbf{E}}_0 e^{i(\tilde{k}z - \omega t)} \quad \text{with} \quad \tilde{k} = \sqrt{\tilde{\epsilon}\mu_0}\omega, \quad (2.7)$$

where  $k$  is the complex wave number. With  $k$  written in its real and imaginary parts Eq. (2.7) becomes

$$\tilde{\mathbf{E}}(z, t) = \tilde{\mathbf{E}}_0 e^{-\kappa z} e^{i(kz - \omega t)}. \quad (2.8)$$

We can see that the wave is attenuated, with an intensity absorption coefficient of  $\alpha = 2\kappa$ , and a refractive index of  $n = ck/\omega$ . Returning to Eq. (2.6), we can use the binomial expansion,  $\sqrt{1+x} \cong 1 + x/2$ , to express the complex wave number;

$$\tilde{k} = \frac{\omega}{c} \sqrt{\tilde{\epsilon}} \cong \frac{\omega}{c} \left[ 1 + \frac{Nq^2}{2m\epsilon_0} \sum_j \frac{f_j}{\omega_j^2 - \omega^2 - i\gamma_j\omega} \right]. \quad (2.9)$$

The real and imaginary parts provide expressions for the refractive index and absorption coefficient;

$$n \cong 1 + \frac{Nq^2}{2m\epsilon_0} \sum_j \frac{f_j (\omega_j^2 - \omega^2)}{(\omega_j^2 - \omega^2)^2 + \gamma_j^2 \omega^2}, \quad (2.10)$$

$$\alpha = \frac{Nq^2\omega^2}{m\epsilon_0c} \sum_j \frac{f_j\gamma_j}{(\omega_j^2 - \omega^2)^2 + \gamma_j^2\omega^2}. \quad (2.11)$$

Examining the behaviour of these functions allows us to interpret the associated physics. Figure 2.1 shows both relationships plotted with arbitrary axis and constants. Peak absorption occurs on resonance where  $\omega = \omega_j$ , as the bound electrons are being driven at their natural frequency, and consequently the energy loss to damping is at a maximum. Interestingly the refractive index sees a sharp drop in this region, known as anomalous dispersion as in the other regions there is a gradual rise with frequency.

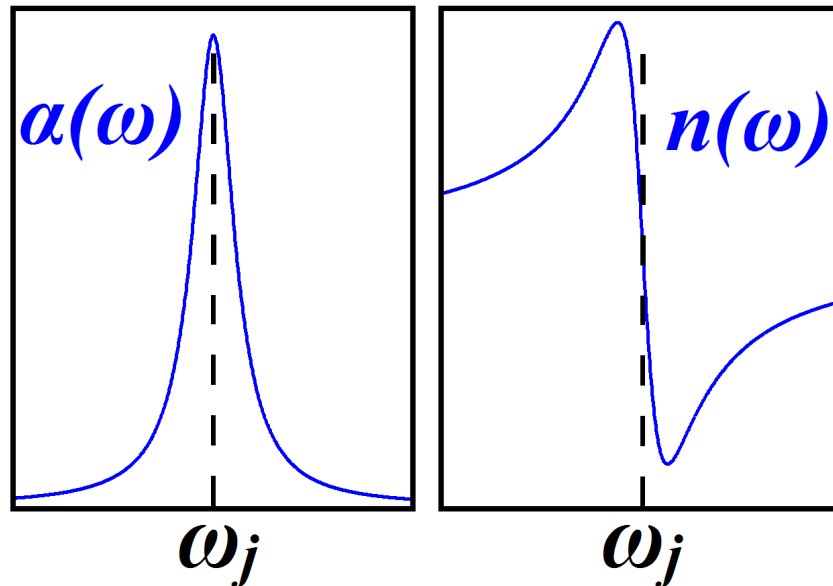


**Figure 2.1 | The frequency dependent absorption coefficient and refractive index for a non-conducting medium.**

Crystalline materials form a special case for optical absorption. A crystalline structure is a periodically ordered material which will possess an electronic band structure that is a set of allowed energy levels which electrons can occupy. These allowed energy levels form quasi-continuous ‘bands’ in energy-momentum space, markedly different from isolated atoms which possess discrete energy levels. The arrangement of these electronic bands has consequences for conduction. Insulators are materials which do not have continuous bands across momentum-energy space but possess a ‘band-gap’, a region of energies where there are no allowed states which effectively prevents thermal excitation

of electrons into conducting states. Conducting materials have continuous bands, or no band-gap, allowing the transfer of electrons in different directions and in energy. A semiconductor is a material where the band-gap is small, allowing for limited thermal excitation of electrons into conducting states. Figure 2.2 illustrates the differences in the band structure of a conducting and insulating material [5].

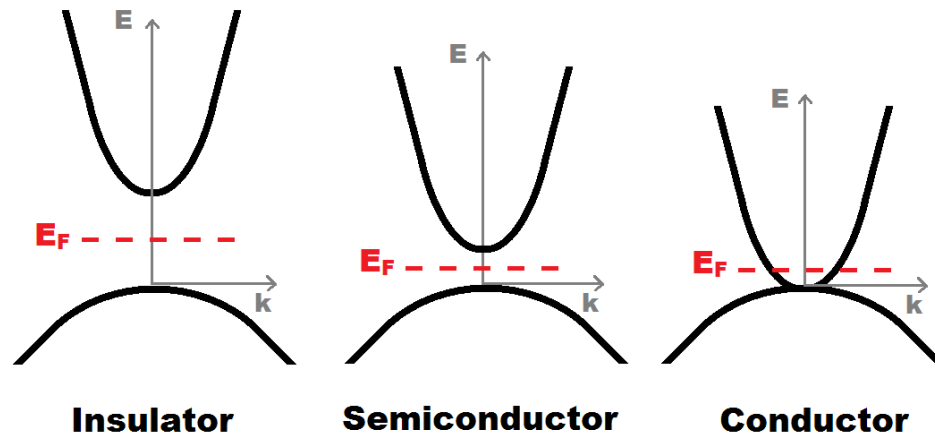


**Figure 2.2 | A simplified band diagram of a conductor, semiconductor and insulator.  $E_F$  is the Fermi level.**

The presence of a band-gap has consequences for optical absorption. A photon with energy less than the band-gap will not be absorbed as the excited electron would have no state to occupy. Consequently, bulk crystalline material is nearly transparent to sub-band-gap photons. For a photon that possesses energy greater than the band-gap, absorption can readily occur. This involves a valance band electron being excited to an energy above the band-gap in the conduction band, forming an electron-hole pair. The existence of a band-gap can provide a material with a rather sudden drop-off in optical absorption as the energy of the photon is reduced below the band-gap. This is shown in Figure 2.3, where the optical absorption versus wavelength can be seen for different semiconductor materials.

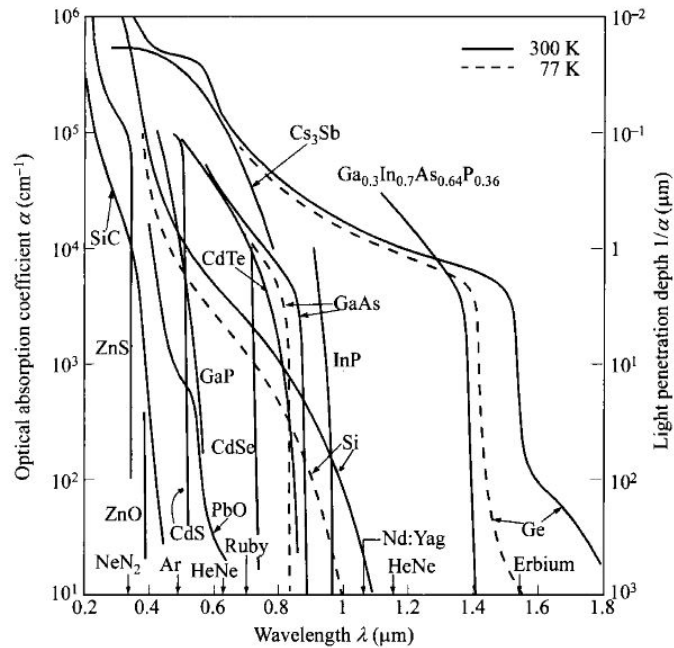


**Figure 2.3 | Optical absorption versus wavelength for various semiconductor materials. Figure reproduced from [6] ©1972 North-Holland.**

Interestingly in Figure 2.3 the behaviour of silicon is noticeably different than that of GaAs and InP. This is because silicon possesses an ‘indirect’ band-gap. A direct band-gap occurs if the lowest energy point in the conduction band aligns in momentum space with the highest energy point of the valence band in energy-momentum space, illustrated in Figure 2.4. In silicon these two points are offset, consequently a photon with the minimum energy to cross the band-gap cannot complete the transition alone. A momentum transfer must occur through a phonon (quantized lattice vibration) interaction. This indirect process is naturally less efficient than the direct process. The sloped absorption spectra in Figure 2.3 is related to this indirect absorption, as the photon energy increases the momentum mismatch decreases making transition more likely.

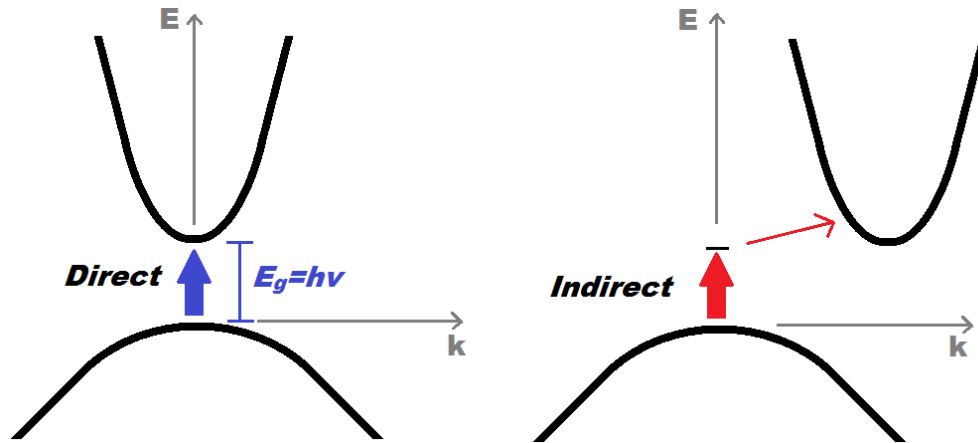


Figure 2.4 | A simplified band diagram comparison of direct and indirect optical absorption. The indirect transition requires an additional momentum transfer step through a phonon interaction.

### 2.1.2 Free carrier absorption

In addition to direct and indirect processes absorption also occurs due to the presence of free carriers. In this case photon energy is transferred to the free carrier, i.e. in the case of electrons those that are already in the conduction band. For a semiconductor at a non-zero temperature there will be some equilibrium population of free carriers due to thermal excitation [5]. This is given by

$$n_0 = \int_{E_c}^{\infty} f(E)N(E)dE, \quad (2.12)$$

where  $N(E)$  is the density of states and  $f(E)$  is the Fermi-Dirac distribution function described by

$$f(E) = \frac{1}{1 + e^{(E-E_f)/kT}}. \quad (2.13)$$

From Eq. (2.12) an approximation for the equilibrium concentration of electrons in the conduction band can be written for small values of  $kT$  (0.026 eV at room temperature), such that

$$n_0 = 2 \left( \frac{2\pi m_n^* kT}{h^2} \right)^{3/2} e^{-\left(\frac{E_c - E_f}{kT}\right)}, \quad (2.14)$$

where  $m_n$  is the electron effective mass and  $E_c - E_f$  is the energy difference between the conduction band and the Fermi level. The first bracketed term represents the ‘effective density of states’. Similarly the expression can be written for holes, where  $E_v$  is the valence band energy, such that

$$p_0 = 2 \left( \frac{2\pi m_p^* kT}{h^2} \right)^{3/2} e^{-\left(\frac{E_f - E_v}{kT}\right)}. \quad (2.15)$$

The addition of dopants to silicon can introduce far more free carriers than are present due to thermal excitation. Furthermore, photogeneration of carriers may occur from other absorption methods, which in turn contribute to the concentration of free carriers.

In addition to the increase in optical absorption (the imaginary part of the refractive index) the real part of the refractive index is also affected by free carriers. These processes contribute collectively to the phenomenon known as plasma dispersion. Soref [7] experimentally determined this behaviour in silicon and formulated the important empirical relations given by:

$$\Delta\alpha = [8.5 \times 10^{-18} \Delta N_e + 6 \times 10^{-18} \Delta N_h] \quad (cm^{-1}), \quad (2.16)$$

$$\Delta n = -[8.8 \times 10^{-22} \Delta N_e + 8.5 \times 10^{-18} \Delta N_h^{0.8}]. \quad (2.17)$$

The change in refractive index is key to the construction of devices such as modulators and variable optical attenuators. It is also important when attempting to understand dynamic behaviour in optoelectronics, as many devices exhibit undesirable behaviour due to the presence of carriers.

### 2.1.3 Two-photon absorption

In a crystalline material a photon of energy smaller than the band-gap is not absorbed as it has insufficient energy to excite an electron to the conduction band. However, two photons with combined energy greater than the band-gap can simultaneously be absorbed. This is known as ‘two-photon absorption’ (TPA) and the strength of this effect is dependent on the intensity of light, or the electric field strength squared. The time varying carrier population density can be described as Eq. 2.18 [8],

$$\frac{dN(t)}{dt} = \frac{\beta}{2h\nu} I^2(t) - \frac{N(t)}{\tau}, \quad (2.18)$$

where  $I$  is the optical intensity,  $N(t)$  is the time varying free carrier population density,  $\tau$  is the free carrier lifetime,  $h\nu$  is the photon energy and  $\beta$  is the TPA coefficient which is approximately 0.8 cm/GW at telecommunications wavelengths [9]. Due to the compact dimensions of SOI waveguides, non-linear effects such as TPA require close consideration. A typical waveguide will have a cross section of less than 0.2  $\mu\text{m}^2$ , therefore a seemingly low coupled average power will result in a high power density.

For ‘typical’ average power levels in silicon waveguides ( $\sim 1$  mW or less) the effect of TPA can mostly be ignored. However detrimental absorption effects will occur for devices which exploit short pulse trains, such as Raman lasers [10]. TPA can be beneficial in some cases, as it allows photodetection where it otherwise won’t occur. As mentioned in chapter 1, microresonator devices with their enhanced intensity can exploit TPA for detection in silicon.

### 2.1.4 Absorption through deep-level defects

A crystalline material can absorb a sub-band-gap photon through the presence of lattice defects. Defects can exist in several forms; this includes imperfections in the lattice, such as vacancies or interstitial atoms, impurity atoms present through contamination but most commonly from impurities intentionally introduced through ion implantation or

during growth. All of these types of defects disrupt the intrinsic band structure, and create energy levels within the band-gap.

A defect level is known as ‘deep’ when it is of much larger energy than the thermal energy ( $kT \approx 0.026 \text{ eV}$  at room temperature), and therefore according to the Fermi-Dirac distribution function will not rapidly ionize at room temperature. Shallow levels are those which are easily ionized at room temperature, such as the commonly used dopants boron and phosphorous.

Optical absorption through deep-levels in silicon has been studied for some time. Fan and Ramdas observed sub-band-gap absorption in silicon irradiated with deuterons, reported in work published in 1959. Absorption occurred with photon energies as little as 0.41 eV, corresponding to wavelengths of  $\approx 3 \mu\text{m}$  [11]. This behaviour is described in Figure 2.5. Later work showed that ion implantation could produce defects such as the silicon divacancy, which is formed by two adjacent vacancies in the diamond lattice structure of silicon and is responsible for an absorption peak at  $1.8 \mu\text{m}$  [12]. The silicon divacancy defect has been attributed to energy levels 0.23 eV below the conduction band, 0.41 eV below the conduction band and 0.23 eV above the valence band [13].

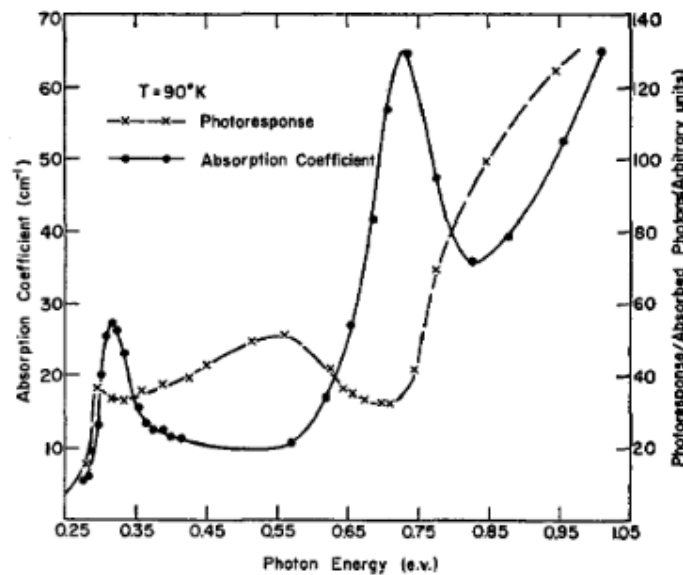
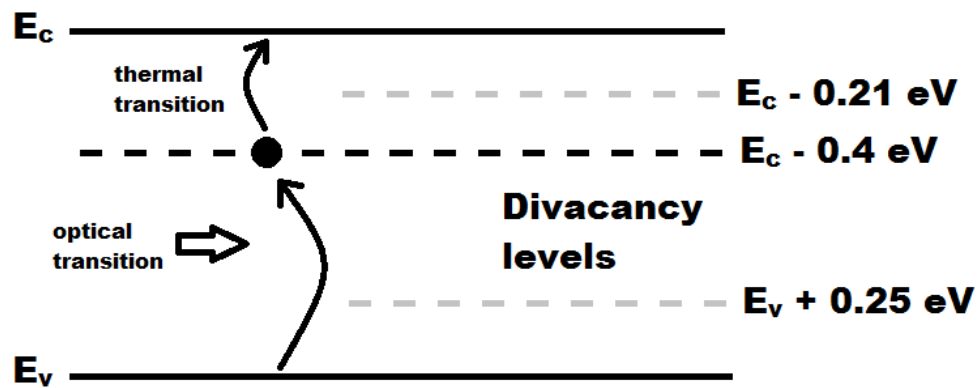


Figure 2.5 | The photoconductance and absorption spectra from *p*-type silicon irradiated with neutrons. Reproduced from [11] ©1959 AIP.

A simple schematic model for optical absorption through a defect is shown in Figure 2.6. A deep-level in the lower half of the band-gap could be filled via thermal excitation from the valence band, followed by photon excitation to the conduction band. Alternatively a deep-level in the upper half of the band-gap could be filled by a photon excitation, the electron being subsequently thermally excited to the conduction band. Deep-level-transient spectroscopy experiments have shown that for 1.55  $\mu\text{m}$  light the latter process dominates in the case of silicon containing divacancies [14].



**Figure 2.6 | A simple model of the optical excitation process through a deep-level. The known levels of the silicon divacancy are labeled.**

The controlled introduction of deep-level defects is very useful for the formation of silicon waveguide detectors. Ion implantation can be used to target specific regions, leaving the remaining silicon waveguides unaffected. A silicon waveguide based  $p-i-n$  model was developed by Logan *et al.* [15] which implemented a mathematical formulation of the model described in Figure 2.6.

Metal impurities are another route to introducing detection capability at longer wavelengths. It has been shown that gold and zinc offer detection through mid-gap states [16, 17]. However the use of such impurities are detrimental for CMOS electronics. Gold is viewed as a contaminant because it is able to rapidly diffuse through silicon at low temperature, leading to the introduction of deep-level defects in undesired locations. A detector made with structural defects such as the divacancy does not face such issues as it

can be easily incorporated into waveguide devices with ion implantation and thermal stability has been shown to beyond 200 °C [18].

The work in this thesis involves implantation conditions and subsequent annealing trends previously observed in defect mediated detector work [14, 15, 18], where the primary defect was identified as the divacancy. It is assumed that the divacancy is the dominant, active defect in all of the devices described here utilizing bulk defects.

### **2.1.5 Surface-state absorption**

One of the assumptions for an ideal crystal is that it possesses infinite periodicity. In a real crystal structure there must be a termination (surface or interface) where atoms will be left with unsatisfied bonds. Electron wavefunctions at the surface will be disrupted and not form continuous bands as in bulk material, resulting in electronic levels within the band-gap. These levels are known as surface states, or interface states if another material system is present (e.g. silicon - silicon dioxide).

Surface-state absorption has been measured in the case of a cleaved silicon surface in vacuum [19], where an absorption peak was observed at an energy of 0.5 eV and was seen to reduce in intensity after surface oxidation. This 0.5 eV state has been attributed to the silicon dangling bond, while a 0.3 eV and a 0.7 eV transition have been identified due to the silicon-oxygen bond [20]. For silicon, a thin layer of surface oxidation occurs naturally under exposure to air at room temperature, the thickness of which is on the order of nanometers. This ‘native’ oxide surface lacks uniformity and leaves some silicon bonds unsatisfied. Alternatively, high temperature oxidation processes produce a thicker and more uniform layer.

Much of the historical efforts in silicon processing have been directed towards reducing the concentration of electronically active surface states. These are undesirable in most devices, as they act as recombination centers and lower operating efficiency. Surface chemistry becomes increasingly important for nanophotonic devices as the bulk material volume is lowered. Surface-state absorption has been studied in microresonators

where it was found to play a significant role beyond scattering due to roughness. In a study by Borselli *et al.* microdisk resonators were subjected to various surface treatment, including hydrogen fluoride to remove the silicon-dioxide layer and  $\text{H}_2\text{O}_2 + \text{H}_2\text{SO}_4$  to oxidize the surface [21]. While in many devices surface states are undesirable, in this thesis this phenomenon is used to create a photodetector sensitive to sub-band-gap photons.

## 2.2 Photodiodes

This section will introduce the basic physics of the photodiode. For further background the reader may refer to the texts *Physics of semiconductor devices* by Sze [5] and *Solid state electronics* by Streetman and Banerjee [22].

### 2.2.1 P-N junction

Semiconductor carrier concentrations can be controlled through the use of dopant atoms. Acceptors are atoms which occupy a lattice site and possess one less electron than the host semiconductor, thus they introduce a ‘hole’ which is a site to capture a free electron. Donors are atoms with an extra electron and when occupying a lattice site they introduce a free electron. Dopants are typically introduced into silicon through ion implantation, allowing for the creation of an abrupt junction between a *p* doped (acceptor) and *n* doped (donor) region. At this junction there will be an initial diffusion current due to the imbalance in free carrier concentration. Electrons will move from the *n* region to the *p* region, while holes will move from the *p* region to the *n* region. This diffusion current will reach an equilibrium as the displaced charge establishes an electric field which introduces a drift current in the opposite direction. At this equilibrium, the drift and diffusion currents are equal and there is a contact potential  $V_0$  across a region that has been cleared of free charge due to this field, known as the depletion region. A schematic of these processes is shown in Figure 2.7.

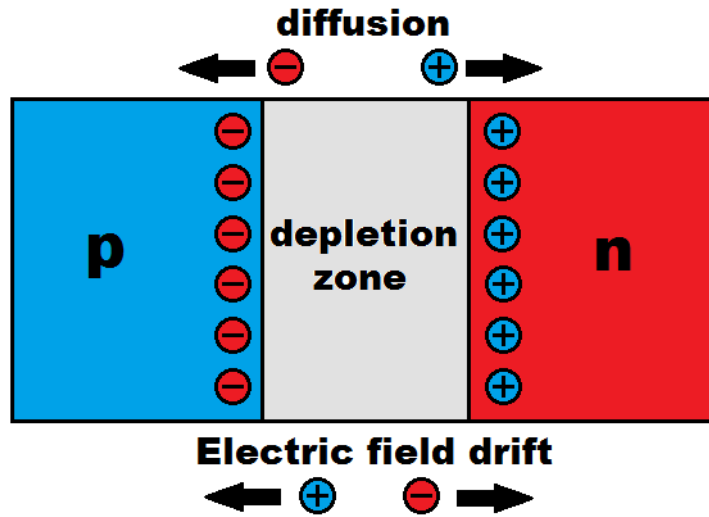


Figure 2.7 | A schematic diagram of an abrupt  $p$ - $n$  junction. The diffusion of carriers results in the presence of an electric field and a region depleted of charge carriers.

The  $p$ - $n$  junction at equilibrium is a potential barrier and performs as a rectifier. Applying a potential to the positive side reduces the potential barrier, allowing for an increased diffusion current. While a potential applied to the negative side further increases this barrier. In the simple case, the current flowing through a  $p$ - $n$  diode can be described by

$$I = I_s \left( e^{qV/kT} - 1 \right), \quad (2.19)$$

where  $I_s$  is the saturation current and  $V$  is the applied bias voltage. For a large negative bias voltage the current approaches  $I_s$ , which is due to drift across the depletion region.

A  $p$ - $n$  junction can serve as a photodiode. If an incident photon excites an electron-hole pair the electric field of the junction can separate the charge preventing recombination and resulting in an observable current. A schematic band diagram of a  $p$ - $n$  photodetector is shown in Figure 2.8. Photo-generation can occur both inside and outside the junction. If carrier generation occurs outside but nearby the junction, then through diffusion there is a possibility for a carrier to reach the depletion region and contribute to photocurrent. On average, electron-hole pair generation will contribute to photocurrent if

it occurs within one diffusion length of the junction. Alternatively, if carriers are generated within the depletion region they are not likely to recombine as the drift field separates them, resulting in a more efficient process. For a  $p-n$  junction the depletion region width is described by

$$W = \left[ \frac{2\epsilon(V_0 - V)}{q} \left( \frac{1}{N_a} + \frac{1}{N_d} \right) \right]^{1/2}, \quad (2.20)$$

where  $V_0$  is the built in junction potential,  $V$  is the applied potential,  $\epsilon$  is the electric permittivity, and  $N_a$  and  $N_d$  are the acceptor and donor concentrations respectively. This width is restrictively small for a photodiode; a larger region is necessary to increase the efficiency of the device.

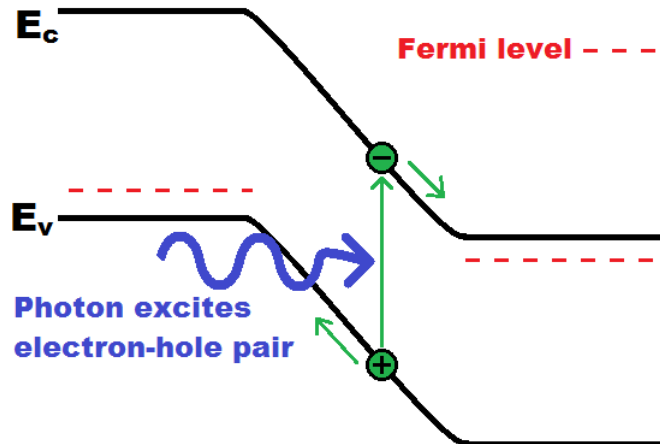


**Figure 2.8 | A simplified band diagram of a  $p-n$  junction showing photodetection. A photon excites an electron from the valence band to the conduction band and the electric field within the depletion region serves to separate the charge and prevent recombination.**

### 2.2.2 P-I-N photodetector

A  $p-i-n$  photodetector is a modified  $p-n$  junction which introduces an extended intrinsic region in between the doped regions. This enlarges the region subject to the drift field thereby enhancing the sensitivity of the device. This larger intrinsic region allows for waveguide based detectors, as the doped regions are positioned where they will not

overlap with the optical mode, maximizing the absorption which occurs in the intrinsic region. Figure 2.9 is a schematic cross-sectional diagram of an SOI waveguide based  $p-i-n$  photodiode. Such a waveguide can be made arbitrarily long for complete absorption of the incident light.

The use of a waveguide structure is important for defect-based photodetectors. The waveguide structure allows for the use of relatively low absorption materials, such as devices found in this thesis. The  $p-i-n$  junction positioning across the waveguide allows the absorption length to be independent from the carrier extraction length, which is not the case for a conventional top-illuminated vertical-junction photodiode. Maintaining a short carrier extraction length is crucial for both operation speed and device efficiency.

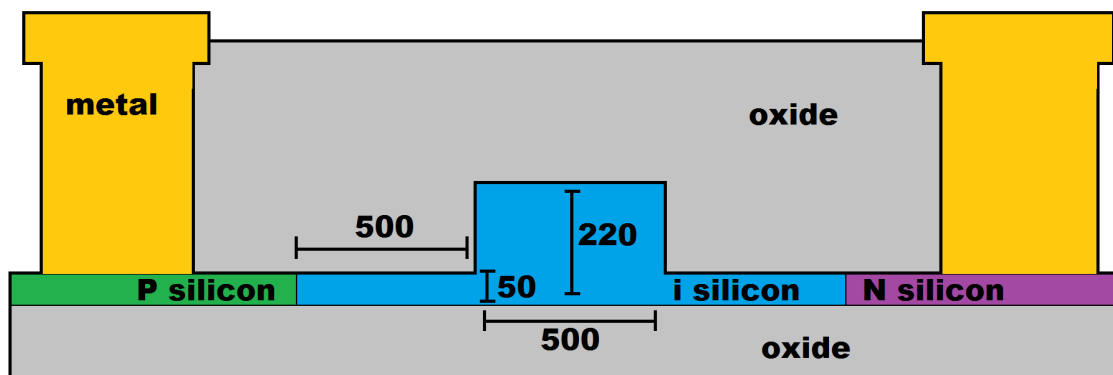


Figure 2.9 | A schematic cross section of a  $p-i-n$  waveguide photodiode. Approximate dimensions are labeled in nanometers.

### 2.2.3 Quantum efficiency

The efficacy of a photodetector is described by its quantum efficiency ( $QE$ ), which can be defined as either *external* or *internal*. External  $QE$  is the number of electron-hole pairs collected to produce photocurrent, divided by the number of incident photons. The internal  $QE$  is defined as the ratio of generated electron-hole pairs to absorbed photons. The internal  $QE$  describes the effectiveness of the medium to absorb photons and produce electron-hole pairs but does not describe genuine device operation, rather its potential. External  $QE$  encapsulates the true device effectiveness by including detrimental factors

such as carrier recombination and non-absorbed light. For a defect-based silicon waveguide *p-i-n* photodetector the external  $QE$  is given by

$$\eta_{ext} = \Gamma\chi(1 - e^{-\alpha L})\gamma, \quad (2.21)$$

where  $\Gamma$  is the modal confinement factor,  $\chi$  is the carrier extraction efficiency as the presence of defects will cause recombination, and  $\gamma$  is the fraction of absorption that leads to carrier generation.  $L$  is the length of the detector and  $\alpha$  is the absorption coefficient.

An alternative metric to characterize a photodetector is the *responsivity*, which is the ratio of current produced to incident optical power (Amperes/Watt). The current flowing in a detector is given by

$$I_p = \eta q \Phi = \eta q \frac{P}{h\nu}, \quad (2.22)$$

where  $\eta$  is the quantum efficiency,  $q$  is the electron charge,  $\Phi$  is photon flux,  $P$  is optical power and  $h\nu$  is the energy per photon. The responsivity  $R$  is then given by

$$R = \frac{\eta q}{h\nu} = \eta \frac{\lambda_0}{1.24}, \quad (2.23)$$

where  $\lambda_0$  is the photon wavelength in microns. From this we can see that for a photodetector operating in the telecommunications windows, a responsivity approaching 1 A/W represents high efficiency. Further gains in efficiency require carrier multiplication.

#### 2.2.4 Operation speed limitations

The operation speed of a *p-i-n* photodetector is limited by several factors. These include the time required for carrier extraction, the  $RC$  time constant due to the electrical circuit properties and the time delay from the diffusion current component (if present).

Avalanche multiplication further increases the time for carrier extraction which will be discussed in the next section.

A light pulse incident on a photodetector will generate electron-hole pairs across the device. The speed at which these carriers can be collected represents a limit on device operation. In terms of communication signals, the majority of the carriers must be swept out of the absorption region before the next information ‘*bit*’ arrives. The carriers are subject to an electric field and will drift across the junction with an average velocity of  $v_d = \mu E$ , where  $E$  is the electric field and  $\mu$  is the carrier mobility. This relation is valid for low electric field strengths, for higher fields ( $> 10^4$  V/m in silicon) the drift velocity is sub-linear and will reach a saturation value near the thermal velocity of approximately  $10^7$  cm/s; in which case a device with a width of  $1 \mu\text{m}$  would have a transit time of 10 ps. At this point the maximum carrier speed is limited by scattering events. Further increases of electric field strength result in energy being imparted to the lattice through collisions, rather than increasing the momentum of carriers.

The  $RC$  time constant imposes a limit on the operation speed of an electric circuit. The equivalent circuit of a photodiode is shown in Figure 2.10.

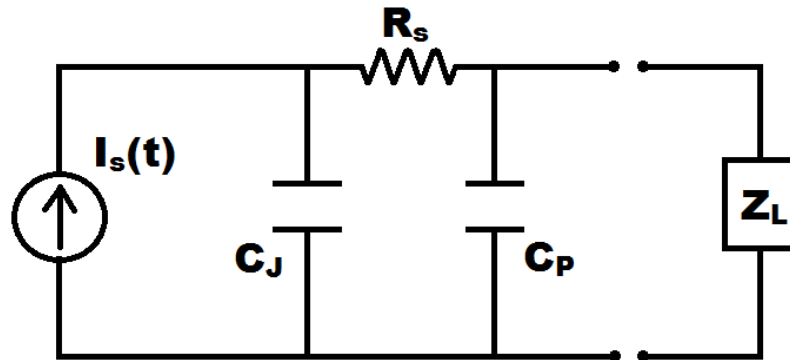


Figure 2.10 | An equivalent electric circuit of a photodiode.

In Figure 2.10  $C_J$  is the junction capacitance,  $C_P$  is the parasitic capacitance due to the metallic structures.  $R_s$  is the resistance due to the metal contacts and the bulk silicon. The electrical 3 dB bandwidth is given by

$$f_{3dB} = \frac{1}{2\pi(R_L + R_S)(C_p + C_j)}. \quad (2.24)$$

A photodiode can also be limited by diffusion current if a portion of the light is absorbed in the doped  $p$  and  $n$  regions. Without a high electric field some carriers will diffuse slowly towards the junction, while others will simply recombine. The carriers that are able to reach the junction will cause a slow tail to the detector's time response. The diffusion current  $J$  for electrons and holes is given by Eq. (2.25) and Eq. (2.26) respectively,

$$J_e = qD_e \frac{\partial n}{\partial x} = qD_e \frac{\Delta n}{L_e}, \quad (2.25)$$

$$J_h = qD_h \frac{\partial p}{\partial x} = qD_h \frac{\Delta p}{L_h}, \quad (2.26)$$

where  $\Delta n$  and  $\Delta p$  are the non-equilibrium carrier concentrations,  $D$  is the diffusivity,  $q$  is electron charge, and  $L$  is the diffusion length or the average length a carrier will travel before recombination. By using the Einstein relation given by Eq. (2.27),

$$D = \frac{\mu_e k_B T}{q}, \quad (2.27)$$

the diffusion current can be rewritten in terms of mobility, such that

$$J_{Dif} = qn\mu_e \left( \frac{k_B T}{qL_e} \right). \quad (2.28)$$

where  $n$  is the density of generated photocarriers,  $\mu_e$  is electron mobility,  $k_B$  is Boltzmann's constant and  $T$  is temperature. This diffusion current,  $J_{Dif}$ , can be compared to the drift current within the junction given by Eq. (2.29), where  $E$  is the electric field.

$$\vec{J}_{drift} = qn\mu_e \vec{E} \quad (2.29)$$

For waveguide based avalanche detectors, electric fields exceed  $10^5$  V/cm which is sufficient for carrier saturation velocity to be reached, where  $k_B T / qL_e$  is on the order of 10 to  $10^2$  but depends ultimately on dopant concentration.

## 2.3 Avalanche photodetectors

### 2.3.1 Avalanche multiplication

When a photodiode is operated in high reverse bias, avalanche breakdown can occur. With a sufficient electric field strength free carriers can be provided with enough kinetic energy that impact ionization occurs. This entails a scattering event with a lattice atom, where the incident carrier generates a new electron-hole pair. The result is carrier multiplication as a single incident carrier can generate two additional carriers which are then separated by the electric field. The electrons are swept to the  $n$  side while holes are swept to the  $p$  side of the diode, during which further multiplication events can occur leading to an ‘avalanche’. A schematic of this process is shown in Figure 2.11, where a single optical generation event leads to three further impact ionization events.

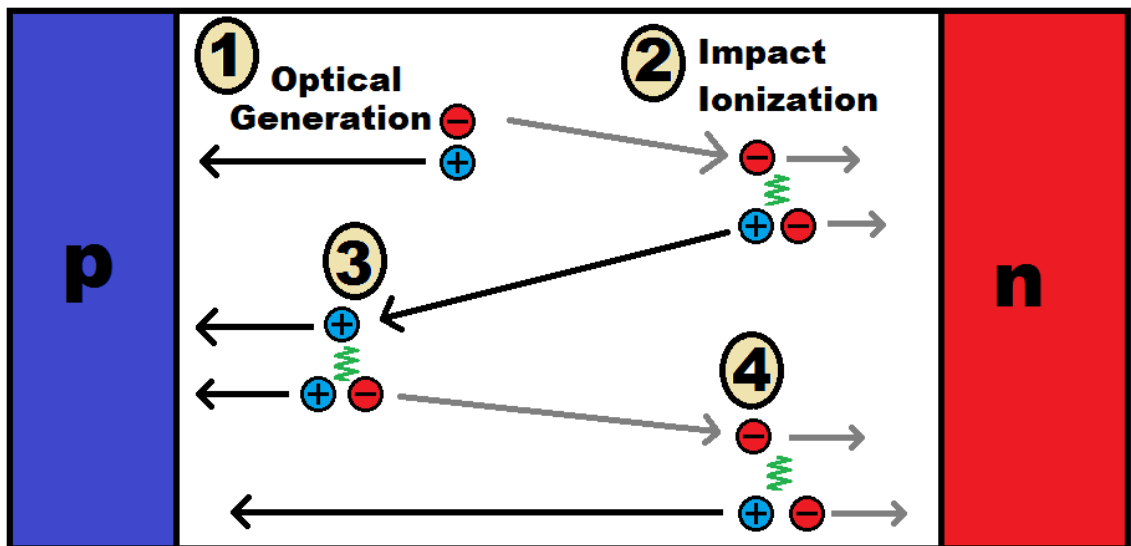


Figure 2.11 | A conceptual diagram of the avalanche multiplication process. An optical generation event (labeled 1) is followed by impact ionization events (labeled 2-4).

Impact ionization can be characterized by a set of coefficients for electrons and holes,  $\alpha_n$  and  $\alpha_p$ . These coefficients are material dependant and describe the average number of ionization events per distance travelled by a carrier. For the case of electron injection at low frequencies the multiplication factor  $M$  is given by

$$M = \frac{(1 - \alpha_p / \alpha_n) \exp[\alpha_n W_D (1 - \alpha_p / \alpha_n)]}{1 - (\alpha_p / \alpha_n) \exp[\alpha_n W_D (1 - \alpha_p / \alpha_n)]}, \quad (2.30)$$

where  $W_D$  is the depletion width [5]. This expression describes the ultimate breakdown voltage of the device, which occurs when  $M$  approaches infinity. If the ionization coefficients are equal, now defined as  $\alpha$ , then Eq. 2.30 can be simplified to Eq. 2.31 and the breakdown voltage occurs when  $\alpha W_D = 1$  and

$$M = \frac{1}{1 - \alpha W_D}. \quad (2.31)$$

### 2.3.2 Avalanche noise

Avalanche breakdown is a process driven by independent impact ionization events. For a given carrier crossing the multiplication region, the number of impact events will vary. This introduces a noise source, described as the *excess noise factor*, which is given in Eq. (2.32) as the mean-square of the multiplication factor over the square-mean of the multiplication factor

$$F(M) = \frac{\langle M^2 \rangle}{\langle M \rangle^2}. \quad (2.32)$$

The excess noise factor  $F$  is dependent on both the multiplication factor and the carrier ionization ratio  $k = \alpha_p / \alpha_n$ . In the case of electron injection, McIntyre [23] showed that the excess noise factor can be expressed as Eq. (2.33)

$$F = M \left[ 1 - (1-k) \left( \frac{M-1}{M} \right)^2 \right] \quad (2.33)$$

$$F \approx kM + \left( 2 - \frac{1}{M} \right) (1-k)$$

From this equation we can see that if  $k=1$ , when  $\alpha_n = \alpha_p$ , then  $F = M$ . If hole ionization is limited and  $\alpha_p=0$  then  $k=0$  and  $F = 2$  for large values of  $M$ . In general, a small  $k$  value is required to minimize the excess noise factor. This is good news for silicon based avalanche detectors as they possess a smaller  $k$  value than alternative materials such as germanium. Varying optical absorption and carrier multiplication properties between materials such as silicon and germanium have led to separate absorption and multiplication structures (SAM) for avalanche photodetectors. In this scheme an efficient absorber material (e.g. germanium) is used to generate the initial photocurrent, while carrier multiplication occurs in an adjacent region of a material possessing a favourable ionization ratio (e.g. silicon).

### 2.3.3 Avalanche-limited transit time

In a non-avalanche diode the carrier transit time limited bandwidth is dependent on the time for a single pass across the device. In an avalanche device carrier generation is ongoing after the pulse of light has been absorbed. The avalanche transit time will be dependent on the ionization ratio, the further the ratio is from  $k=1$  the shorter the transit time will be. For example, if only electrons are multiplying ( $k=0$ ) then the carrier transit time would be similar to the non-avalanche case, as the generated holes travelling opposite to the electrons would not cause further ionization events.

This effect leads to a bandwidth limitation and was characterized by Emmons [24]. If the steady-state multiplication factor  $M_0 < \alpha_n/\alpha_p$  then bandwidth has little dependence on the multiplication. If  $M_0 > \alpha_n/\alpha_p$  then a constant gain-bandwidth product is seen. In this case, the multiplication as a function of frequency can be expressed as Eq. (2.34),

$$M(\omega) = M_0 \left[ 1 + (\omega^2 M_0^2 \tau_{eff})^2 \right]^{-1/2}, \quad (2.34)$$

where  $\tau_{eff}$  is the effective transit time, which is given by

$$\tau_{eff} = N \left( \frac{\alpha_p}{\alpha_n} \right) \tau, \quad (2.35)$$

where  $\tau$  is the carrier single pass transit time through the multiplication region and  $N$  is a number varying from 1/3 to 2 depending on the ionization coefficient ratio [24].

## 2.4 Optical resonators in silicon

The availability of high quality resonators is one of the main benefits of the silicon-on-insulator platform. The most common resonant structure is the ring resonator which is extensively used for modulation and filtering. This section will review the fundamentals of the ring resonator. For a more detailed treatment of waveguide resonators, the reader may refer to *Optical microresonators: theory, fabrication, and applications* by Heebner [25] and *Photonics: Optical Electronics in Modern Communications* by Yariv [26]. The contents of this section follow from these works, primarily from [25].

### 2.4.1 Ring resonators

To understand the ring resonator it is instructive to briefly consider the analogous structure in free space optics, the Fabry-Perot cavity, which consists of two partially reflective surfaces as input/output couplers. This structure will introduce constructive and destructive interference, which provides increased optical intensity at resonant frequencies. The two partially reflective surfaces are directly analogous to a microring where the ring itself is the cavity and the input/output is acquired through evanescent coupling. Evanescent coupling involves waveguides placed within close proximity of each other, such that there is significant overlap of the exponentially decaying electric

fields associated with the propagating modes. Figure 2.12 shows schematic diagrams of both a Fabry-Perot cavity and a microring resonator with two coupling waveguides.

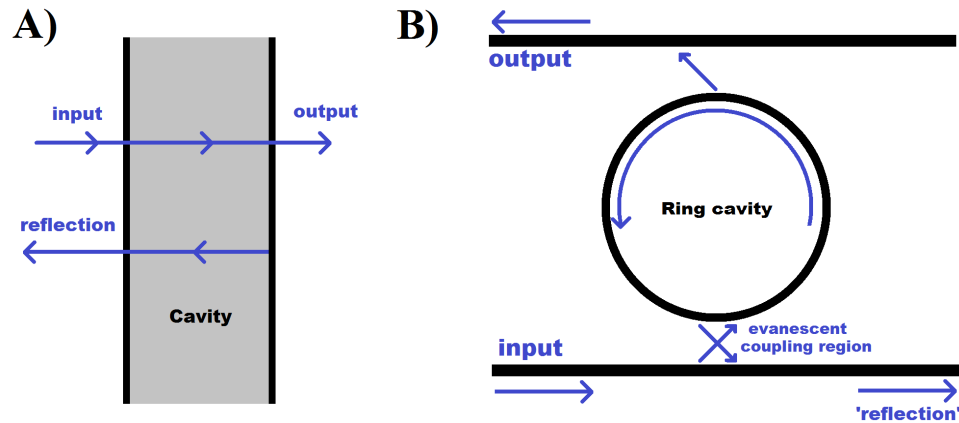


**Figure 2.12 | Schematic diagrams of (A) the Fabry-Perot resonator and (B) the add-drop microring resonator. The two structures are analogous as each consists of a cavity with two couplers that are partially transmissive.**

There are two common configurations for ring resonators, the *add-drop* resonator, consisting of two bus waveguides and a ring as shown in Figure 2.12; and the *all-pass* resonator consisting of a single bus waveguide and a ring waveguide.

#### 2.4.2 All-pass microring resonator

The all-pass resonator consists of a cavity and a single bus waveguide. Light travelling along the waveguide is partially coupled to the ring waveguide where it circulates and is partially coupled back out to the waveguide. With a coherent light source, constructive and destructive interference occur in the ring and on the latter section of the bus waveguide. Figure 2.13 shows the all pass configuration with the electric fields labeled

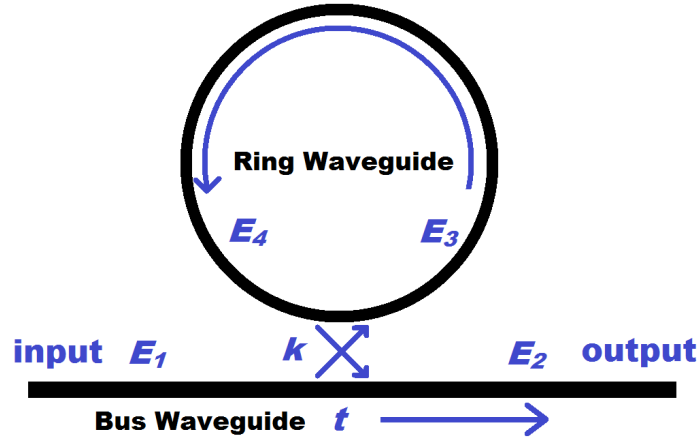


Figure 2.13 | A schematic diagram of an all-pass ring resonator with the electric field coefficients  $E$ , cross-coupling coefficient  $k$  and self-coupling (transmission) coefficient  $t$ .

Considering Figure 2.13 we can write the transfer matrix that describes the electric field coupling,

$$\begin{pmatrix} E_4 \\ E_2 \end{pmatrix} = \begin{pmatrix} t & ik \\ ik & t \end{pmatrix} \begin{pmatrix} E_3 \\ E_1 \end{pmatrix}, \quad (2.36)$$

where  $k$  and  $t$  are the cross and self coupling coefficients respectively, which for energy conservation must satisfy the relation  $k^2 + t^2 = 1$ . Within the ring, the field  $E_4$  can be related to  $E_3$ , the field entering the ring as  $E_4$  travels the circumference of the ring and evolves to  $E_3$  after some attenuation and phase change. This is given by

$$E_3 = e^{-\frac{\alpha}{2}2\pi r} e^{i\beta 2\pi r} E_4 = ae^{i\delta} E_4, \quad (2.37)$$

where  $r$  is the ring radius,  $\alpha$  is the optical power loss coefficient of the waveguide, 'a' is the single round trip loss coefficient for the electric field through the resonator,  $\beta$  is the propagation constant  $\beta = 2\pi n_{\text{eff}}/\lambda$  and  $\delta$  is the round trip phase change. From Eq. (2.36) and Eq. (2.37), the ratio of the fields  $E_2$  and  $E_1$  can be solved which provides a relation for the transmitted field through the bus waveguide,

$$\frac{E_2}{E_1} = \frac{ita}{1 - kte^{i\delta}}. \quad (2.38)$$

The intensity of the transmitted optical field is then

$$\frac{I}{I_0} = \left| \frac{E_2}{E_1} \right|^2 = \frac{a^2 + t^2 - 2ta \cos(\delta)}{1 + (ta)^2 - 2ta \cos(\delta)}. \quad (2.39)$$

We can look at the electric field within the ring, the ratio of  $E_3$  to  $E_1$  which is given by

$$\frac{E_3}{E_1} = \frac{ikae^{i\delta}}{1 - tae^{i\delta}}. \quad (2.40)$$

The intensity is then given by the square of the field

$$\frac{I_3}{I_1} = \left| \frac{E_3}{E_1} \right|^2 = \frac{(1 - t^2)a^2}{1 + (ta)^2 - 2ta \cos(\delta)}. \quad (2.41)$$

When the resonance condition is satisfied,  $\delta = 2\pi m$  where  $m$  is an integer, the cosine term goes to 1. By considering the low loss case where  $a \approx 1$  the equation simplifies to

$$BUF = \frac{I_3}{I_1} = \frac{1+t}{1-t}. \quad (2.42)$$

This quantity is known as the ‘*Build-up factor*’ (BUF) and tells us that the power within the ring can be greatly enhanced when the coupling to the ring is small. It is important to note that as there is no power source within the ring, the average power over the spectrum must remain the same, resulting in off resonance intensity lower than the input.

### 2.4.3 Coupling condition

By examining the relation for transmitted optical intensity we can examine the impact of the coupling coefficients. If we consider Eq. (2.39) and apply the resonance condition,  $\delta = 2\pi m$ , the cosine terms equate to 1 and we are left with Eq. (2.43),

$$\frac{I}{I_0} = \left| \frac{E_2}{E_1} \right|^2 = \frac{a^2 + t^2 - 2ta}{1 + (ta)^2 - 2ta} = \frac{(a-t)^2}{(1-ta)^2}. \quad (2.43)$$

From this relationship we can see that if  $a=t$  then the transmission intensity will go to zero. This special case is known as critical coupling. It is a commonly desired trait for a ring resonator as it provides the maximum achievable extinction ratio, or the intensity ratio on-resonance versus off-resonance. The coupling coefficient and loss within the ring are design parameters which may be altered to achieve critical coupling. In an SOI microring achieving this condition is a challenge as waveguide fabrication tolerances are present. For an SOI rib waveguide there will be variation in the waveguide width due to photolithography variations, the silicon slab region thickness due to etching variations and also the waveguide height will vary due to the original SOI thickness variation. All such variations affect the evanescent coupling strength. Waveguide optical loss is primarily from sidewall roughness and bending loss occurs for small radius rings ( $r < 5\mu\text{m}$ ). However even these relatively constant fabrication parameters lead to uncertainty in cumulative loss, as the optical mode profile overlap with the loss sources will change depending on the waveguide dimensions.

#### 2.4.4 Free spectral range

The separation between adjacent resonance frequencies is known as the *free spectral range* ( $FSR = \Delta\omega = \omega_2 - \omega_1$ ). Light circulating at adjacent resonance frequencies will be subject to the phase relation given by,

$$2\pi = \beta_2 L - \beta_1 L \quad \text{where} \quad \beta = \frac{n\omega}{c}. \quad (2.44)$$

When dealing with nanophotonic waveguides, significant dispersion is present and cannot be ignored. The refractive index (or effective index of the optical mode) will vary with wavelength, and on the scale of the *FSR* this variation is approximately linear and given by

$$n = n_0 + \frac{\Delta\omega}{2} \frac{dn}{d\omega}, \quad (2.45)$$

where  $n_0 = n(\omega_0)$  and  $\omega_0 = \frac{\omega_2 + \omega_1}{2}$ . Substituting Eq. (2.45) into Eq. (2.44) yields

$$\frac{2\pi c}{L} = n_2\omega_2 - n_1\omega_1 = \omega_2 \left( n_0 + \frac{\Delta\omega}{2} \frac{dn}{d\omega} \right) - \omega_1 \left( n_0 - \frac{\Delta\omega}{2} \frac{dn}{d\omega} \right) \quad (2.46)$$

$$\frac{2\pi c}{L} = \Delta\omega \left( n_0 + \omega_0 \frac{dn}{d\omega} \right). \quad (2.47)$$

Rearranging to solve for  $\Delta\omega$  gives

$$\Delta\omega = \frac{2\pi c}{L \left( n_0 + \omega_0 \frac{dn}{d\omega} \right)} = \frac{2\pi c}{Ln_g}, \quad (2.48)$$

the quantity  $n_g$  is known as the group index, and for a nanophotonic SOI waveguide is significantly larger than the effective index, often  $> 50\%$  depending on the waveguide dimensions. The FSR can also be described in terms of wavelength, given by Eq. (2.49) in terms of frequency and wavelength,

$$FSR = \Delta\nu = \frac{c}{Ln_g} \quad \Delta\lambda = -\frac{\lambda_0^2}{Ln_g}. \quad (2.49)$$

### 2.4.5 Quality factor

The quality factor ( $Q$ ) represents the sharpness of a resonance. The definition is given by the ratio of the stored energy in the resonator versus the energy lost per cycle,

$$Q = 2\pi \frac{\text{Energy stored within resonator}}{\text{Energy lost per cycle}}, \quad (2.50)$$

which can also be expressed in terms of wavelength or frequency for a given resonance located at  $\lambda_0$  with a Full-Width Half-Depth of  $\Delta\lambda$ ,

$$Q = \frac{\omega_0}{\Delta\omega} = \frac{\lambda_0}{\Delta\lambda}. \quad (2.51)$$

A higher  $Q$  represents a longer photon lifetime within the resonator, with the relationship given by

$$t_{\text{phot}} = \frac{Q}{\omega} = \frac{Q\lambda}{2\pi c}, \quad (2.52)$$

which sets a corresponding bandwidth limitation of

$$\nu_c = \frac{1}{2\pi t_{\text{phot}}}. \quad (2.53)$$

#### 2.4.6 Racetrack resonators

The shape of the resonator itself is not fundamental to operation, provided the waveguide dimensions remain the same. Rings are typically used as they minimize surface area occupied and resonator length for a given bend radius. Eq. 2.49 tells us that to maximize  $FSR$ , as is often desirable for both filters and modulators, then the resonator length must be minimized. Typical resonator dimensions are on the order of  $10 \mu\text{m}$  for the ring radius. Below a bend radius of  $5 \mu\text{m}$ , physical space to incorporate the modulator structure becomes a consideration but more importantly the optical loss of the waveguide increases.

A common alternative to the microring is the racetrack resonator, which introduces a longer coupling region as opposed to the ‘point’ coupler of a ring. The benefit of a

racetrack is that a longer coupling region can simplify design and simulation. With a point coupler, changing the coupling coefficient requires a change in coupling gap whereas a racetrack coupler can simply be made longer, without introducing variation in the coupling gap. In terms of design, changing the coupling gap in a ring requires computationally intensive numerical simulation, as the point coupler cannot be well described analytically. However in a racetrack coupler, the parallel waveguides can be described with a coupling strength per unit length, allowing for simple variation of the coupler length to adjust the coupling strength. In this thesis racetrack resonators are used in chapter 3. These racetrack devices are in the add-drop configuration, which modifies the transmission equation. For a resonator with two identical couplers, the transmission function can be simply modified from the all-pass resonator (Eq. 2.39) by including an additional source of loss, that is the new coupler. The loss coefficient  $a$  is replaced with  $at$ , leaving

$$\frac{I_{transmitted}}{I_0} = \frac{t^2 + a^2 t^2 - 2at^2 \cos \delta}{1 + a^2 t^4 - 2at^2 \cos \delta}. \quad (2.54)$$

An SEM image of an SOI racetrack resonator is shown in Figure 2.14. The resonator is in an add-drop configuration with identical couplers.

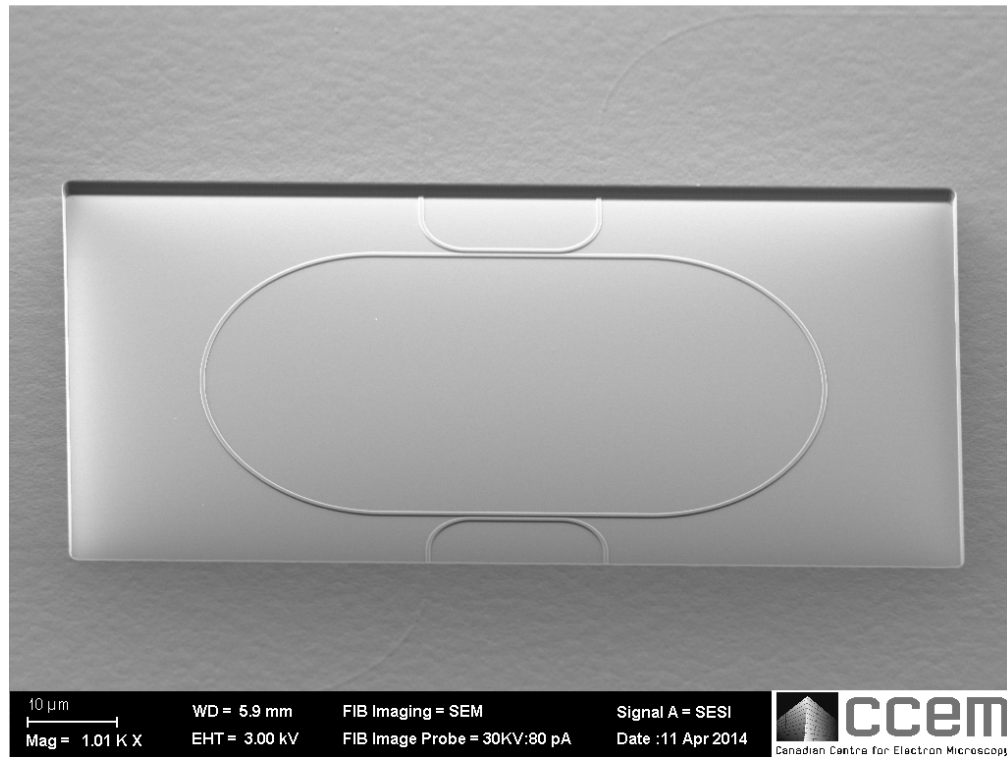


**Figure 2.14 | An SEM image of an SOI racetrack resonator in an add-drop configuration. The oxide cladding has been removed in the rectangular region.**

## 2.5 High-speed measurement instrumentation

### 2.5.1 Modulation patterns

There are multiple methods in which signals can be encoded onto a carrier wave. This thesis does not concern modulation techniques specifically, so this will be a brief overview to provide context for subsequent measurements.

The simplest format for encoding data optically is *amplitude shift keying*, that is changing the optical power level of the signal from one state to another. This approach allows for various amplitude levels to be defined, but commonly an on-off keying (OOK) approach is taken which allows for binary transmission. An important distinction is that of return to zero (RZ), or non-return to zero (NRZ). RZ signals may fluctuate between +1 and -1 for instance, with a rest state in between each bit at zero. This rest state signifies

the timing for each bit, meaning an external clock source is not required. NRZ signals alternate between levels without returning to a rest state at zero. This approach requires an external clock, but without the presence of the ‘0’ symbols the effective bit rate is higher.

This raises the distinction between symbol rate (or baud rate), and bit rate. The bit rate represents the actual data transmitted while the symbol rate represents how rapidly the carrier wave is being modulated. For example, an OOK-RZ signal has a symbol rate twice that of the bit rate and for an OOK-NRZ signal the symbol rate equals the bit rate.

The use of OOK has fundamental limits. For example, increasing the symbol rate results in a broadened laser spectrum. A wider spectrum results in more noise in a channel, and thus lowers the sensitivity of the system. More advanced techniques that employ phase modulation deliver data rates which surpass the capabilities of amplitude shift keying. The use of *phase shift keying* can deliver bit rates above the symbol rate. Measurements in this thesis make exclusive use of OOK-NRZ.

### **2.5.2 Frequency response characterization**

Measuring the frequency response characteristic of a device is carried out using a network analyzer. This tool provides a generated signal to apply to a system under test, the output signal from the system is then compared with the original signal’s amplitude and phase (if desired). The output signal from a network analyzer is not a bit pattern, but a sine wave signal which can vary in frequency to cover the spectrum of interest.

For measurements in this thesis, it is desirable to know how a photodiode will respond to a modulated input signal. To do this, the output signal of the network analyzer drives an optical modulator. The photodiode then receives the modulated optical signal, converting it back to an electrical one which the network analyzer receives and compares with the original output. This measurement is done while varying the output frequency, such that the limit of operation can be determined. This is known as an  $S_{21}$  parameter measurement, and it provides the transmitted gain or loss of the device under test. The S-

parameter or scattering-parameter name arises from the matrix associated with a multiple port device. Figure 2.15.A shows a 2 port device with incident and reflected waves. For example, the  $S_{11}$  parameter would be the reflected signal from the device back to the network analyzer. S-parameters are complex quantities, but in this thesis we are concerned with the real part (amplitude). Figure 2.15.B shows an example spectrum from a network analyzer, where the measurement frequency is swept up to 10 GHz and the  $S_{21}$  parameter is recorded. A general performance metric is the ‘3 dB bandwidth’, which is the frequency where the device response drops to half power [27].

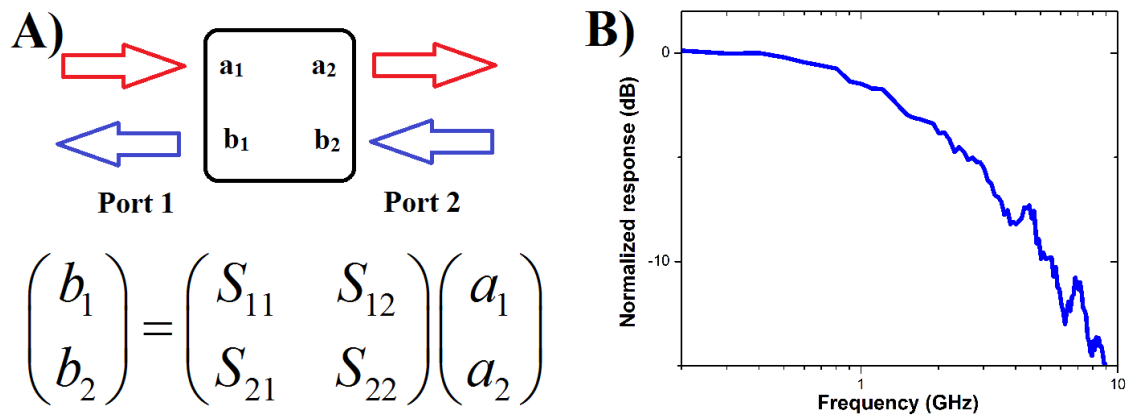


Figure 2.15 | A) Transmission and reflection parameters for a 2-port device under test. B) A sample  $S_{21}$  measurement from a network analyzer.

### 2.5.3 Eye diagrams and bit-error rate measurement

Network analyzers provide key information on the frequency response of devices but are not sufficient to fully determine the quality of a device. Measurement of a transmitted bit pattern is necessary to provide a test under actual operating conditions. Compared to the network analyzer, a bit pattern provides a non-uniform and larger signal which can expose faults in the device under test.

Examining a lengthy bit pattern one bit at a time is not the most convenient approach. For experimental purposes it is convenient to use an *eye diagram*, which contains every sequence of 0's and 1's in a bit pattern in one image. It does not contain separate information from a full bit pattern, rather an eye diagram superimposes each instance onto

a single image so it may be analyzed efficiently. A wide open eye represents a well behaved device, as 0's and 1's are clearly defined. While a 'closed' eye represents poor operation, as 0's and 1's are indistinguishable. An eye diagram allows for the evaluation of pattern-dependent behaviour, for example a device may respond differently to a '0' following a single '1', than a '0' following a sequence of multiple '1' symbols. Furthermore, it provides for a characterization of noise, rise/fall time (often defined 90% to 10%), and jitter of the signal [28]. Figure 2.16 shows an eye diagram with sample metrics labeled.

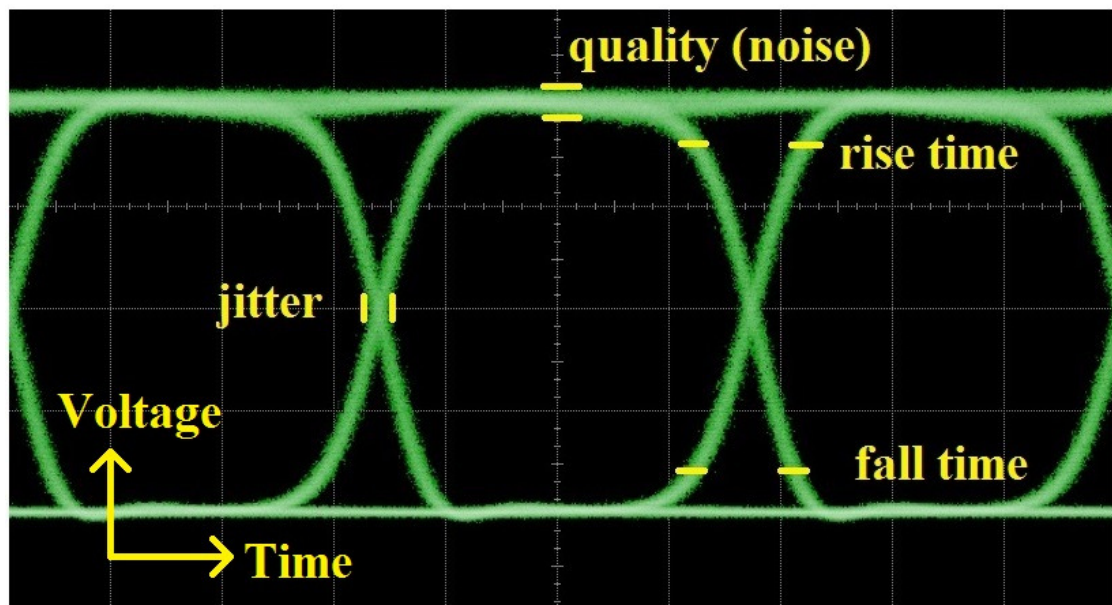


Figure 2.16 | An example eye diagram. Relevant metrics obtainable from the diagram are labelled.

The eye diagram provides a significant amount of information on the quality of operation, yet in order to rigorously evaluate a component a bit-error rate test (BERT) is employed. In this test, a generated bit pattern is input to the DUT and the output is compared to the original signal, with an error being a bit that doesn't correspond with the original sequence. This approach directly tests the communications capability of the device. In the case of a photodiode, a common metric is to evaluate the bit-error rate versus received optical power.

The acceptable bit-error rate of a device depends on the application but in general one error per terabit (an error rate of  $10^{-12}$ ) may be considered ‘error free’. Encoding techniques, such as forward error correction (FEC) allow for a greatly increased device error rate by encoding data into a longer bit-stream. For example the RS(255, 239) code takes a sequence of 239 bits and encodes them into 255 bits. In this scheme communication with a BER less than  $10^{-12}$  requires an original uncoded BER of less than  $10^{-4}$  [29]. This results in a 7% ‘overhead’ in the data rate, but the relaxed BER requirement can offer greater utility. For example, if a photodiode can operate with lower received optical power then it may be placed at the end of a longer link. In integrated applications where electrical power consumption is critical, it would allow for a lower power laser.

## 2.6 Simulation tools

Commercial software simulation tools were used in the course of this thesis work. For waveguide simulation RSoft Beamprop was used to provide optical mode profiles. RSoft Fullwave was used for finite-difference time-domain (FDTD) simulations of resonant devices (<http://optics.synopsys.com/rsoft/>). Ion implantation parameters were obtained through the use of SRIM (Stopping and range of ions in matter) software ([www.srim.org](http://www.srim.org)) [30]. Electrical simulations of *p-i-n* junctions were performed with Silvaco ATLAS ([www.silvaco.com](http://www.silvaco.com)).

## 2.7 Summary

This chapter has provided the necessary background for understanding the following chapters. The remainder of this thesis will describe the fabrication and experimental characterization of defect-mediated photodiodes.

## References

1. Hunsperger, R.G. Integrated optics: theory and technology. *Springer* (2002).
2. Okamoto, K. Fundamentals of optical waveguides. *Academic press* (2010).
3. Plummer, J.D., Deal, M.D. and Griffin, P. Silicon VLSI technology: fundamentals, practice, and modeling. *Prentice Hall* (2000).
4. Griffiths, D.J. Introduction to electrodynamics, Vol. 3. *Prentice Hall* (1998).
5. Sze, S.M., and Kwok, K.N. Physics of semiconductor devices 3rd Edition. *John Wiley & Sons* (2007).
6. Melchior, H. ‘Demodulation and Photodetection Techniques’ in Arecchi, F.T. and Schulz-Dubois, E.O. Laser Handbook Vol. 1, North-Holland, 725-835 (1972).
7. Soref, R.A. and Bennett, B.R. Electrooptical effects in silicon. *IEEE J. Quantum Elec.* **23(1)**,123-129 (1987).
8. Dekker, R. *et al.* Ultrafast nonlinear all-optical processes in silicon-on-insulator waveguides. *J. Phys. D: Appl. Phys.* **40(R49)** (2007).
9. Bristow, A.D., Rotenberg, N. and Van Driel, H.M. Two-photon absorption and Kerr coefficients of silicon for 850–2200 nm. *Appl. Phys. Lett.* **90(19)**, 191104-191104 (2007).
10. Liang, T.K. and Tsang, H.K. Role of free carriers from two-photon absorption in Raman amplification in silicon-on-insulator waveguides. *Appl. Phys. Lett.* **84(15)** 2745-2747 (2004).
11. Fan, H.Y. and Ramdas, A.K. Infrared absorption and photoconductivity in irradiated silicon. *J. Appl. Phys.* **30(8)**, 1127-1134 (1959).
12. Stein, H.J., Vook, F.L. and Borders, J.A. Direct evidence of divacancy formation in silicon by ion implantation. *Appl. Phys. Lett.* **14(10)**, 328-330 (1969).
13. Troxell, J.R. Ion-implantation associated defect production in silicon. *Solid-State Electron.* **26(6)**, 539-548 (1983).
14. Doylend, J.K. Characterization and integration of defect-mediated photodetectors for silicon photonic circuits. PhD. Thesis, *McMaster University* (2011).

15. Logan, D.F., Jessop, P.E. and Knights, A.P. Modeling defect enhanced detection at 1550 nm in integrated silicon waveguide photodetectors. *J. Lightwave Technol.* **27(7)**, 930-937 (2009).
16. Mailoa, J.P. *et al.* Room-temperature sub-band gap optoelectronic response of hyperdoped silicon. *Nature Commun.* **5**, 1-8 (2014).
17. Grote, R.R. *et al.* Extrinsic photodiodes for integrated mid-infrared silicon photonics." *Optica* **1(4)**, 264-267 (2014).
18. Foster, P.J. *et al.* Optical attenuation in defect-engineered silicon rib waveguides. *J. Appl. Phys.* **99(7)**, 073101 (2006).
19. Chiarotti, G. *et al.* Optical absorption of surface states in ultrahigh vacuum cleaved (111) surfaces of Ge and Si. *Phys. Rev. B.* **4(10)**, 3398 (1971).
20. Yamashita, Y. *et al.* Spectroscopic observation of interface states of ultrathin silicon oxide. *J. Appl. Phys.* **79(9)**, 7051-7057 (1996).
21. Borselli, M., Johnson, T.J. and Painter, O. Measuring the role of surface chemistry in silicon microphotronics. *Appl. Phys Lett.* **88(13)**, 131114-131114 (2006).
22. Streetman, B.G. and Banerjee, S. Solid state electronic devices. Vol. 4. *Prentice Hall* (2000).
23. McIntyre, R.J. Multiplication noise in uniform avalanche diodes. *IEEE T. Electron. Dev.* **13(1)** 164-168 (1966).
24. Emmons, R.B. Avalanche-photodiode frequency response. *J. Appl. Phys.* **38**, 3705-3714 (1967).
25. Heebner, J., Grover, R. and Ibrahim, T.A. Optical microresonators: theory, fabrication, and applications. *Springer* (2008).
26. Yariv, A. and Yeh, P. Photonics: Optical Electronics in Modern Communications. *Oxford University Press* (2007).
27. Hui, R. and O'Sullivan, M. Fiber optic measurement techniques. *Elsevier Academic Press* (2009).
28. Azadeh, M. Fiber optics engineering. *Springer* (2009).

29. Smith, B.P. and Kschischang, F.R. Future prospects for FEC in fiber-optic communications. *IEEE J. Sel. Topics. Quantum Electron.* **16(5)**, 1245-1257 (2010).
30. Ziegler, J.F., Ziegler, M.D. and Biersack, J.P. SRIM–The stopping and range of ions in matter (2010). *Nucl. Instrum. Meth. B.* **268(11)**, 1818-1823 (2010).

# Chapter 3 Resonant Detection via Mid-gap Lattice Defects

## Overview

This chapter reports results on defect mediated detection in SOI waveguide resonant devices. First described is a study of the impact of the introduction of ion implantation induced defects in silicon ring resonators; work which determined the refractive index changes introduced by such defects for the first time. The chapter then describes fabrication of ring and disk resonator based photodetectors for both continuous-wave and high-speed operation. These devices perform in line with expectation for continuous-wave operation but exhibit instability at high speed. This is followed by an examination of the potential causes and finally a summary of the utility of these devices considering these limitations. This work represents the first detailed description of this instability.

Results from this work have been reported by the author in the following research journal publications.

Ackert, J.J. *et al.* Defect-mediated resonance shift of silicon-on-insulator racetrack resonators. *Opt. Express* **19(13)**, 11969-11976 (2011).

Ackert, J.J. *et al.* Silicon-on-insulator microring resonator defect-based photodetector with 3.5-GHz bandwidth. *J. Nanophotonics* **5(1)**, 059507-059507 (2011).

## **3.1 The effect of lattice defects on the refractive index of silicon waveguides**

### **3.1.1 Introduction**

Ion implantation has been used previously for intentional introduction of lattice defects in silicon for purposes of sub-band-gap photodetection [1, 2]. This technique of defect engineering has also been used for other applications such as modifying carrier lifetime [3]. In this chapter the effects of low dose ion implantation on the refractive index in silicon waveguides for wavelengths around 1550 nm are determined for the first time. This is achieved by inert ion implantation of silicon-on-insulator (SOI) racetrack resonators and observing the resonance condition shift which allows for the determination of both the real and imaginary parts of the refractive index. This data defines useful knowledge when incorporating defects into resonant detectors, as described later in this chapter, and for more general use of defect engineering in silicon photonics.

Further, the deliberate introduction of lattice defects could be utilized to alter devices post fabrication. For example, ring resonators are very sensitive to refractive index changes. Variation in waveguide dimensions lead to small changes in the effective index of the guided optical mode, and large displacements of resonance wavelengths. Ring and racetrack resonators are sensitive to the coupling condition which depends on the physical gap between the bus waveguide and ring waveguide. Introducing a low level of defects after fabrication could increase the loss of a ring and change its coupling condition in a controlled manner which would allow for the post-fabrication correction of device characteristics; a technique known as ‘trimming’.

### **3.1.2 Device fabrication and experimental methods**

For this experimental work, add-drop SOI racetrack resonators were employed, consisting of 30  $\mu\text{m}$  radius bends and either 15  $\mu\text{m}$  or 40  $\mu\text{m}$  long coupling regions. The

fabrication was facilitated by CMC Microsystems and carried out at IMEC in Leuven, Belgium. The silicon waveguide was 220 nm high, over a 2  $\mu\text{m}$  thick layer of buried oxide. The waveguides had a nominal width of 450 nm and were patterned using 193 nm ultraviolet lithography.

Post-fabrication inert ion implantation was carried out at the Tandetron Laboratory at Western University. The high implantation energies of up to 4 MeV available on this tool allow for the implanted ion species to penetrate through the cladding and waveguide and reside in the buried oxide, ensuring only structural defects in the silicon waveguide. Photolithography carried out at McMaster University was used to define ion implantation windows such that the coupling region between the bus waveguide and racetrack could remain unaffected by the implantation. This ensures the coupling coefficients of the device would not change, so that the quality factor ( $Q$ ) and ring loss can be determined. Figure 3.1 shows the photomask layout for the implantation as well as an SEM image of a racetrack. Several chips underwent the ion implantation process with varying dose below the amorphization threshold [4], at energies of 350 keV for boron ions and 700 keV for silicon ions.

The samples in this section are listed with an implant dose and species along with a prefix A or B, which represents the total resonator lengths of 218 and 268  $\mu\text{m}$  respectively. For example, a device labeled A/3E14- boron describes a resonator of length 218  $\mu\text{m}$  which has undergone a boron ion implantation with a dose of  $3 \times 10^{14} \text{ cm}^{-2}$ .

After ion implantation the hardened photoresist mask required removal using a ‘piranha etch’ solution of  $\text{H}_2\text{SO}_4 + \text{H}_2\text{O}_2$ . This is an exothermic reaction, the heat from which determined the baseline annealing temperature of 100  $^\circ\text{C}$ . After this process each sample was annealed in sequential steps of 25  $^\circ\text{C}$  up to a maximum of 300  $^\circ\text{C}$ , with a duration of 5 minutes. Between each step the sample was optically characterized at room temperature using a tunable laser and fiber coupling setup. Light was coupled on and off the chip via shallow etched gratings. The tunable laser was a NewFocus 6427, which

covers the wavelength range from 1520-1570 nm with a 1 pm resolution and an absolute wavelength stability better than 5 pm over an hour.

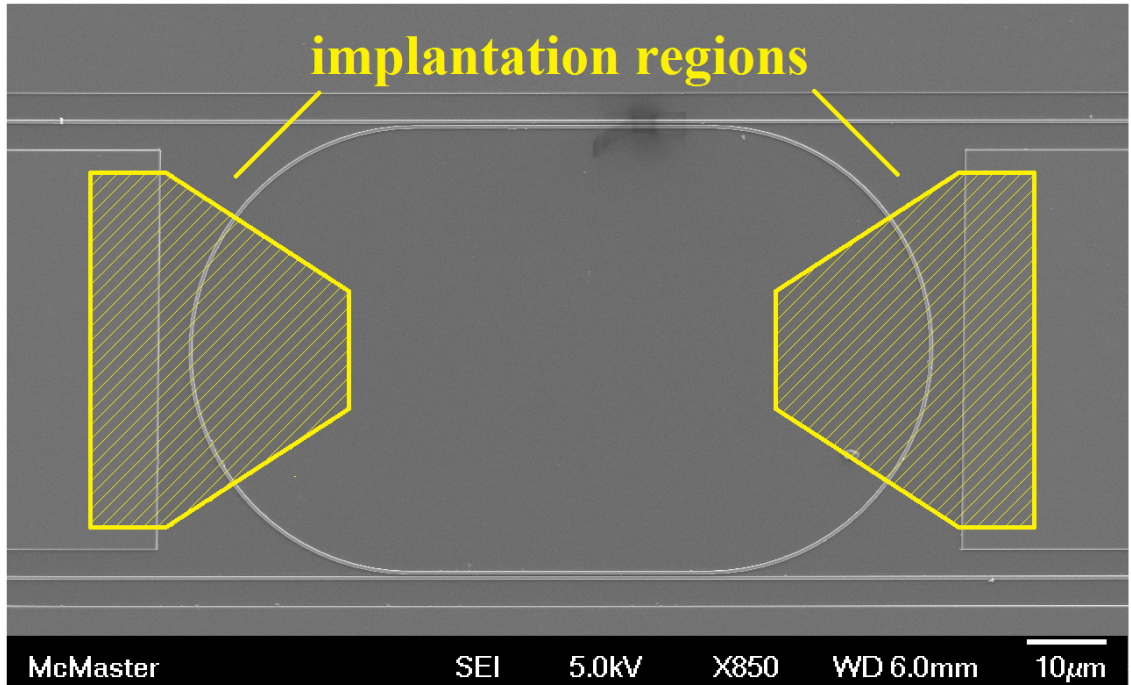
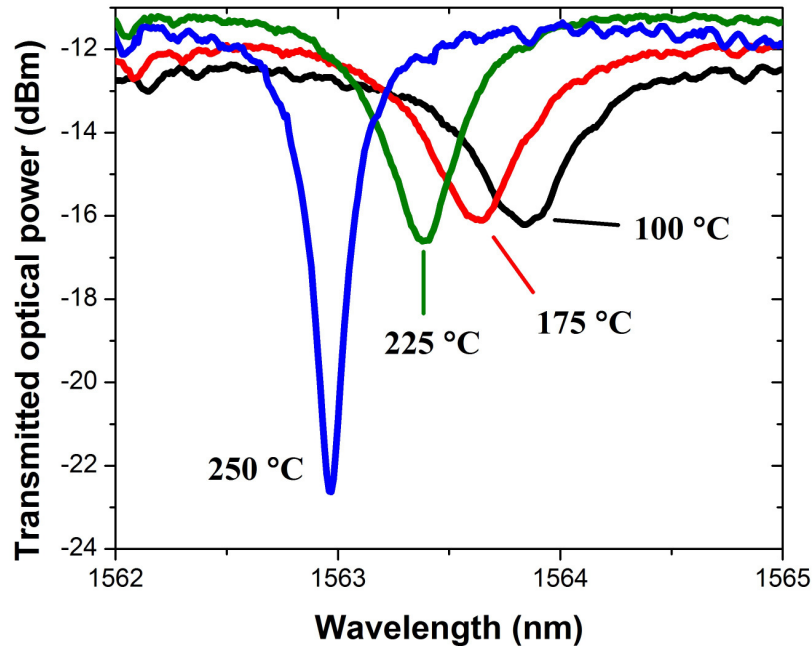


Figure 3.1 | An SEM image of a racetrack resonator with an overlay of the photomask used for ion implantation. The image was taken at the Canadian Centre for Electron Microscopy.

### 3.1.3 Experimental results

After ion implantation and the subsequent annealing procedure two distinct effects on the resonator behaviour are observed. Firstly a resonance shift after ion implantation, which returns toward the original position as the sample is annealed. Specifically, the resonance is shifted to a higher wavelength after ion implantation (red-shift), and moves progressively lower with annealing temperature increase. Second, the quality factor ( $Q$ ) of the ring is diminished after implantation (evident by the broadening of the resonance peak). This is an expected result considering previous work showing increased optical absorption with ion implantation in a silicon waveguide [5]. As the annealing temperature increases the defect concentration of defects is lowered and the  $Q$  returns towards the pre-implanted value.

As an example of this behaviour Figure 3.2 shows optical spectra for the device A/3E14-boron. The transmitted power versus wavelength is shown for several annealing temperatures.



**Figure 3.2 | Post ion implantation optical transmission spectra for device A/3E14-boron. As the annealing temperature is increased the  $Q$  increases and the resonance shifts lower in wavelength. This trend is representative of other implanted devices, as well as those that received a silicon implant.**

A summary of results for different devices is shown in Figure 3.3 where a comparison of resonance shift versus annealing temperature is plotted for three nominally identical resonators (i.e. identical prior to post-fabrication ion implantation). Each resonator was from a different chip and received a different implantation dose. A clear increase in resonance shift is seen as the implantation dose is increased. This indicates that the concentration of lattice defects in the silicon influences the real part of the refractive index. After ion implantation the shift in refractive index is positive, with a reduction towards the original value upon annealing.

In Figure 3.3b the optical loss of the racetrack resonators versus annealing temperature is shown for multiple chips. To extract the loss value the resonator spectra were fit to the analytical expression for optical transmission of an add-drop resonator with

identical couplers. This expression was given in chapter 2, but shown again here as Eq. (3.1);

$$\frac{P_{in}}{P_{out}} = \gamma \frac{t^2 + A^2 t^2 - 2At^2 \cos \delta}{1 + A^2 t^4 - 2At^2 \cos \delta} \quad (3.1)$$

where,  $P_{out}$  is output power,  $P_{in}$  is input power,  $\gamma$  is the insertion loss,  $t$  is the transmission coefficient,  $A = \exp(\alpha L)$  with  $L$  as the resonator length,  $\alpha$  the loss coefficient, and the phase  $\delta = 2\pi n_{eff} L / \lambda$ . Upon fitting it was found that the transmission coefficient did not change with annealing. This was expected as the region was masked during implantation. The values of loss in Figure 3.3 can be compared to a model introduced by Foster *et al.* [5]. This model estimates loss due to lattice defects for a range of implantation conditions of varying ion species, dose and energy. From Figure 3.3 we can compare the values for the baseline annealing temperature as this most closely represents the post-implantation condition. From the Foster model we would expect 23, 96 and 152 dBcm<sup>-1</sup>, for increasing ion dose respectively. The measured values from Figure 3.3 are 71, 239 and 301 dBcm<sup>-1</sup>, approximately twice the loss predicted from the model. Considering the different experimental conditions used by Foster, this discrepancy is not surprising. The Foster model has also underestimated loss previously when compared to experimental results [5].

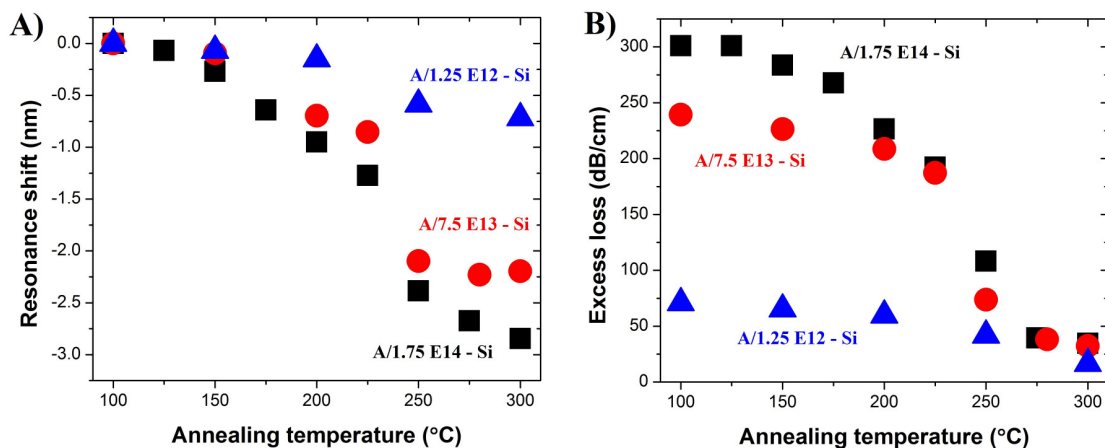


**Figure 3.3 | Three nominally identical racetrack resonators implanted with silicon at 700 keV. The marker size is indicative of the uncertainty. A) Resonance shift relative to the implanted state as a function of annealing temperature. B) The total optical loss of the racetrack resonators.**

As the devices are annealed at increasingly higher temperatures the optical loss trends downward, consistent with the trend of resonance shift and annealing. The abrupt decrease in both loss and resonance shift after annealing at 200 °C suggests that the deep-level responsible for these changes is the silicon divacancy. The divacancy has previously been observed as the primary optically active defect after low dose ion implantation in silicon [6].

The  $Q$  may be used to assess the optical loss within the resonator. Values of  $Q$  were extracted from the resonance linewidth (obtained through fitting a Lorentzian function) and plotted in Figure 3.4 for two devices representative of the group. As the devices are annealed there is an increase in the  $Q$  and a corresponding blue-shift in resonance wavelength.

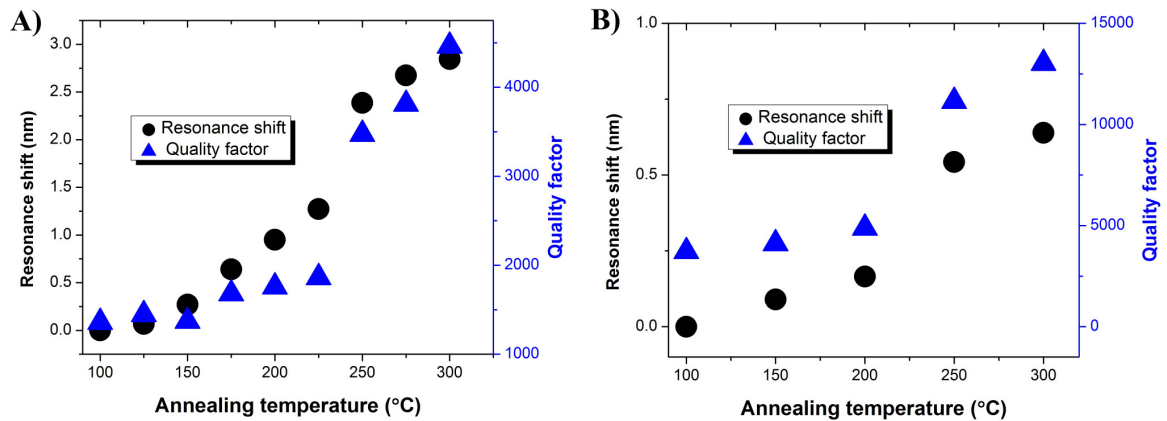


**Figure 3.4 | Quality factor and resonance blue-shift (relative to the implanted state) versus annealing temperature for devices. A) A/1.5 E14-Si B) B/1.25 E12-Si. The marker size is indicative of the uncertainty.**

### 3.1.4 Determination of the real component of the refractive index

To convert the measured resonance shift to a change in the real part of the refractive index we first need to determine how the effective index of the waveguide mode changes with refractive index in the silicon. The ion implantation is assumed to produce a significant change only in the refractive index of the silicon and not the buried oxide. In Figure 3.5 a simulation of the change in waveguide effective index is plotted versus the

change in the refractive index of silicon. This simulation was obtained with a waveguide modesolver [7] implemented in Matlab, the results were verified with Rsoft Beamprop software. The resulting slope is,  $dn_{eff}/dn_{si} = 1.177$ . This figure is known as the effective index susceptibility and has been previously discussed as a way to portray effective index changes in silicon waveguides due to changes in the core refractive index [8]. The effective susceptibility found here and plotted in Figure 3.5 tells us that the change in effective index is 17% larger than that of the core.

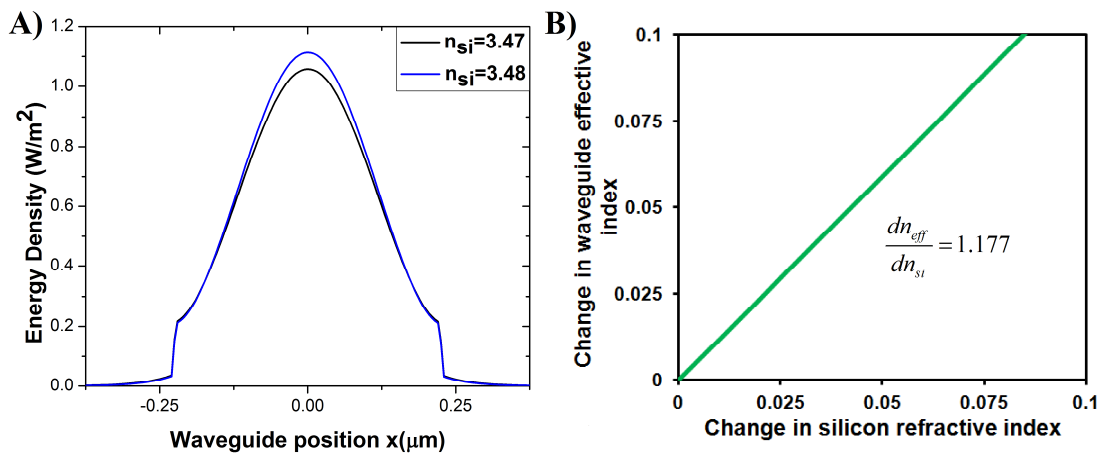


**Figure 3.5 | A simulation of the change in effective index as a function of change in the real part of the refractive index of silicon in a 450 x 220 nm SOI waveguide for a wavelength of 1563 nm.**

We can derive an expression to relate the change in refractive index to the change in resonance wavelength. For a resonator with a uniform non-dispersive medium with refractive index  $n$ , length  $L$  and mode index  $m$ , the mode condition at wavelength  $\lambda$  is given by

$$m\pi = \frac{2nL}{\lambda_m}. \quad (3.2)$$

A change in index of refraction leads to a change in resonance wavelength,

$$\frac{d\lambda}{dn} = \frac{L}{m} = \frac{\lambda}{n}. \quad (3.3)$$

For a resonator with dispersion (waveguide, material), the mode condition is given by

$$m\pi = \frac{2n_{eff}L}{\lambda_m}, \quad (3.4)$$

and the free-spectral range is

$$FSR = \frac{-\lambda^2}{Ln_g}, \quad (3.5)$$

with the group index  $n_g$  given by

$$n_g = n_{eff} - \lambda \frac{dn_{eff}}{d\lambda}. \quad (3.6)$$

We then rearrange Eq. (3.6) to solve for  $n_{eff}$ , and add a term to consider the effective index susceptibility, providing

$$n_{eff} = n_g + \lambda \frac{dn_{eff}}{d\lambda} + \Delta n_{Si} \frac{dn_{eff}}{dn_{Si}}. \quad (3.7)$$

From the mode condition given by Eq. (3.4), we know that the ratio  $n_{eff}/\lambda_m$  is equal for the initial wavelength  $\lambda_0$  to the shifted wavelength  $\lambda_0 + \Delta\lambda$ , therefore with Eq. (3.7) we can write

$$\frac{n_g + \lambda_0 \frac{dn_{eff}}{d\lambda}}{\lambda_0} = \frac{n_g + (\lambda_0 + \Delta\lambda) \frac{dn_{eff}}{d\lambda} + \Delta n_{Si} \frac{dn_{eff}}{dn_{Si}}}{\lambda_0 + \Delta\lambda}. \quad (3.8)$$

This equation can be solved for the wavelength shift, leading to

$$\frac{\Delta\lambda}{\lambda} = \frac{\Delta n_{Si}}{n_g} \frac{dn_{eff}}{dn_{Si}}. \quad (3.9)$$

For the case where the silicon index change equals the effective index change, this equation simplifies to a form shown previously by Gardes *et al.* [8],

$$\frac{\Delta\lambda}{\lambda_0} = \frac{\Delta n_{eff}}{n_g}. \quad (3.10)$$

To summarize Eq. (3.9), the shift in refractive index is determined by three factors: (1) the shift in material refractive index; (2) the material and waveguide dispersion and (3)

the change in mode profile resulting from a change in material index. The same effect is found for temperature dependence of waveguide-based resonant devices [9].

With Eq. (3.9) we can determine the maximum index shift for the resonators for each dose. Through the resonator's free spectral range, a group index of 4.545 was found at a wavelength of 1563 nm. From Figure 3.3 the implantation doses of silicon were  $1.25 \times 10^{12} \text{ cm}^{-2}$ ,  $7.5 \times 10^{13} \text{ cm}^{-2}$  and  $1.75 \times 10^{14} \text{ cm}^{-2}$ , while the respective resonant shifts were  $\Delta\lambda = 0.7 \text{ nm}$ ,  $2.2 \text{ nm}$  and  $2.9 \text{ nm}$ . The implantation regions covered one third of the resonator length, resulting in a shift in refractive index of  $\Delta n_{\text{Si}} = 0.005$ ,  $0.016$  and  $0.021$  respectively.

### 3.1.5 Discussion

Through ion implantation in add-drop SOI racetrack resonators, the refractive index shift and optical loss due to deep-level defects was determined directly in silicon waveguides for the first time.

A shift in the real part of the refractive index of 0.005 was observed for a silicon implantation with a dose of  $1.25 \times 10^{12} \text{ cm}^{-2}$ . The Soref relations [10] indicate that a concentration of  $3 \times 10^{18} \text{ cm}^{-3}$  holes, or alternatively  $5.9 \times 10^{18} \text{ cm}^{-3}$  electrons would be required to achieve the same shift in index. We can compare this to the concentration of defects using a relation found by Foster [5] that describes the vacancy type defect concentration  $C_D$  as

$$C_D = (2.79 \times 10^{10}) \phi_A^{0.63}, \quad (3.11)$$

where  $\phi_A$  is the adjusted ion dose, found by multiplying the actual dose by the number of vacancies per angstrom per ion obtained with “The stopping range of ions in matter” (SRIM) code [11]. For the chosen implantation condition (silicon at 700 keV), a factor of 0.2 vacancies per angstrom per ion is found with SRIM, resulting in  $C_D = 4.2 \times 10^{17} \text{ cm}^{-2}$ .

We note that the higher dose of silicon at  $1.75 \times 10^{14} \text{ cm}^{-2}$  only produced an index shift four times larger for a dose approximately 100 times greater, indicating that the

composition of defects produced is dependent on dose, a result reflected in the performance of defect mediated detectors as a function of dose.

The results are important for future designs of resonant devices in general as defects may be used for device modification, or ‘trimming’ after fabrication. A low concentration of defects could be introduced and subsequently annealed to alter the real and imaginary refractive index of a device. This information is also useful in the design of resonant defect-based detectors, information on which constitutes the remainder of this chapter. Specifically, understanding the optical loss in the ring allows the designer to choose the correct coupling gap while the real part of the refractive index will influence the free spectral range and resonance location.

## **3.2 High-speed resonant detection via defect states in silicon ring resonators**

### **3.2.1 Overview**

Defect based silicon ring resonator detectors have been previously studied and characterized for continuous-wave conditions. Characterization of the detector response at high speed has been reported previously only once in a conference proceedings paper [12], and this effort provided few details. In this section a defect based SOI waveguide ring resonator is described which is found to operate with an open eye diagram at 5 Gbit/s with a small signal 3 dB bandwidth of 3.5 GHz at a reverse bias of 15 V. A detailed analysis of the results discovered a previously unknown, fundamental limitation of such devices under high frequency operation.

### **3.2.2 Device fabrication and experimental methods**

The resonators were fabricated via CMC microsystems at CEA-LETI, Grenoble, France using 193 nm deep-ultraviolet lithography on SOI wafers with a top silicon

thickness of 220 nm and a buried oxide layer of 2  $\mu\text{m}$ . The silicon waveguides were created from a 170 nm etch, leaving a slab height of 50 nm. A 1  $\mu\text{m}$  thick oxide layer was deposited over the waveguides to isolate them from an Al/Cu metal contact layer. Boron and phosphorous ion implantations at a dose of  $2 \times 10^{14} \text{ cm}^{-2}$  formed the electrical doped regions of the photodiodes. To allow for absorption in the infrared, inert ion implantation was used to create deep-level defects. Boron ions were implanted at an energy of 350 keV and a dose of  $1 \times 10^{13} \text{ cm}^{-2}$ . Light was coupled on and off the waveguides with shallow etch grating couplers designed for the transverse electric (TE) mode at a wavelength of 1550 nm, with a total device throughput loss of 16 dB. An optical micrograph of the ring can be seen in Figure 3.6.

The photodiodes were incorporated onto 40  $\mu\text{m}$  diameter rings with a waveguide width of 500 nm and a coupling gap of 200 nm. The quality factor was measured to be approximately 10,000 and the free spectral range was  $4.98 \pm 0.02 \text{ nm}$ . The photodiode makes up approximately 2/3 of the ring circumference (extending beyond the via visible in Figure 3.6) and does not overlap the coupling region. The remaining portion of the ring is placed beneath a resistive heater, formed with a narrow strip of metal. This heater can be used to thermally tune the resonance wavelength if necessary.

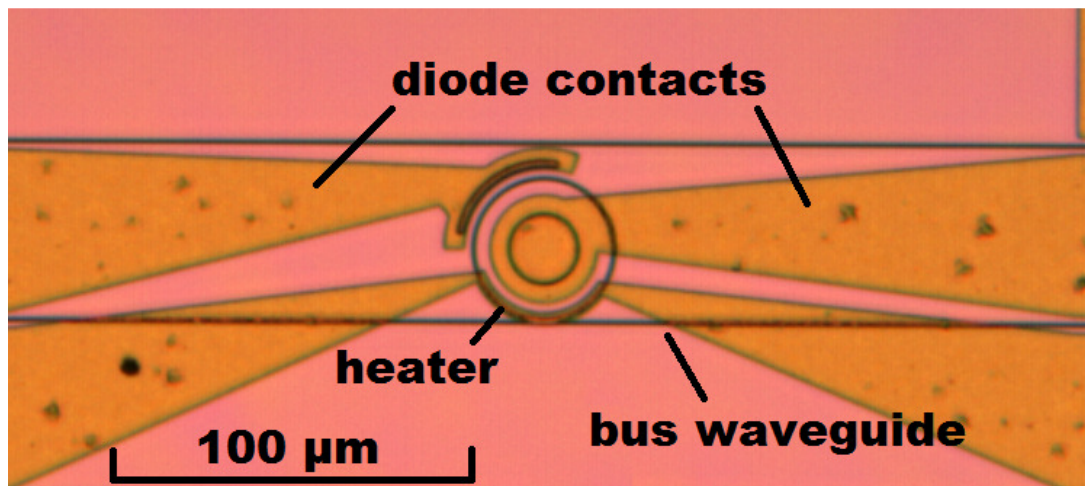


Figure 3.6 | An optical micrograph of a ring resonator detector with a 40  $\mu\text{m}$  diameter.

### 3.2.3 High-speed characterization method

A vector network analyzer (VNA) and a 10 GHz fiber coupled lithium niobate modulator were used to measure the small signal frequency response of the photodiode. An 18 GHz bias tee (picoseconds pulse labs model 550B), was used to apply bias to the device under test. The response of the system was calibrated using a 12 GHz capable, commercial InGaAs detector. This calibration eliminated the frequency response of the system except for the probe required to contact the ring resonator photodiode. The probe used was a Picoprobe model 40A-GS-300 rated at 40 GHz. For bit pattern measurements a 12.5 Gbit/s pattern generator was used to drive the modulator, while a 25 GHz RF amplifier was used to boost the photodiode signal prior to measurement with an oscilloscope. The experimental setup is represented as a block diagram in Figure 3.7.

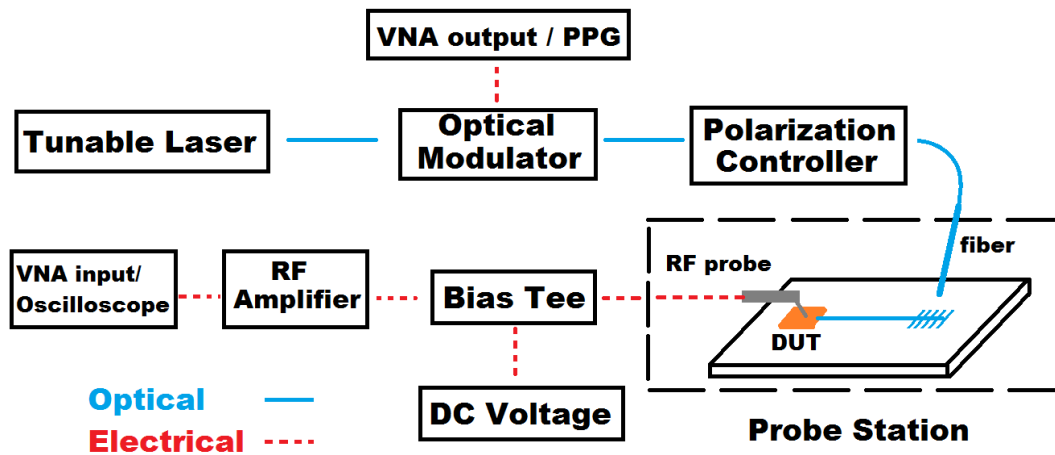
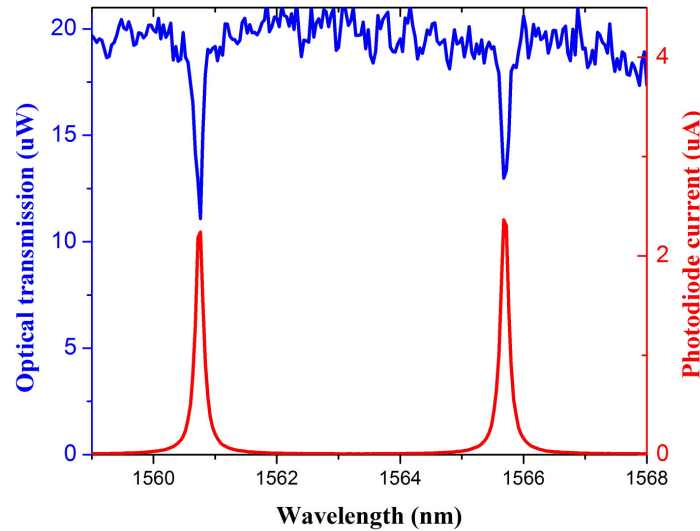


Figure 3.7 | A block diagram of the experimental setup for high-speed characterization. Small signal measurements were taken using a vector network analyzer (VNA), while eye diagrams were recorded with the pulse pattern generator (PPG) and oscilloscope.

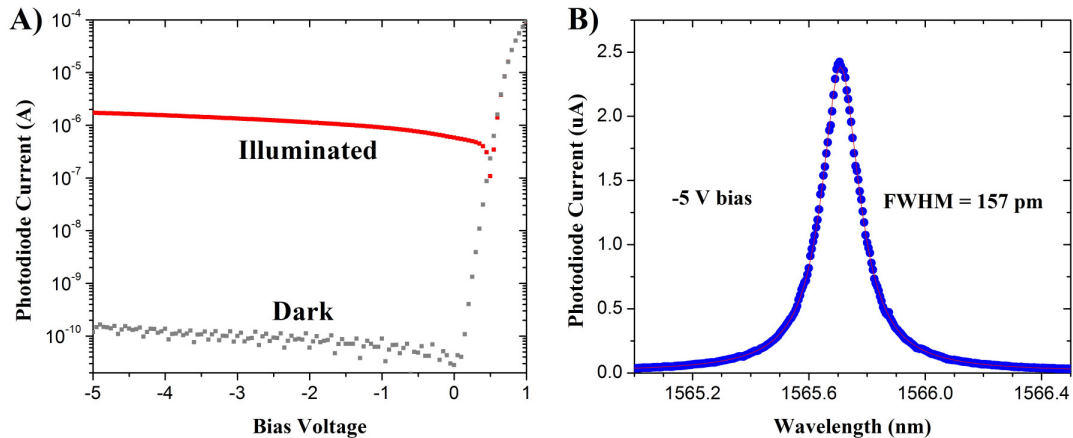
### 3.2.4 Continuous-wave measurement results

Figure 3.8 shows the optical transmission and photodiode current as a function of wavelength. The photocurrent follows the optical transmission showing enhancement while on resonance, with a responsivity of 0.023 AW at a reverse bias of 5 V. Figure 3.9

shows a current-voltage (IV) plot of the device. The dark current is 0.2 nA at a reverse bias of 5 V.



**Figure 3.8 | Optical transmission and photodiode current as a function of wavelength for the 40  $\mu\text{m}$  diameter ring resonator.**



**Figure 3.9 | Photodiode current as a function of wavelength for a 5 V reverse bias, and the current – voltage characteristic for dark and illuminated conditions with an estimated waveguide coupled power of 110  $\mu\text{W}$ .**

The devices show excellent sensitivity to low optical power levels. A photocurrent spectra is shown in Figure 3.10 for a 40  $\mu\text{m}$  diameter ring detector. The tunable laser output power was set to 0 dBm, and the built-in attenuator was used to reduce the power

by 50 dB, resulting in an estimated 2 nW of waveguide coupler power. The detector produced 40 nA of photocurrent on resonance, giving an internal responsivity of 20 A/W.

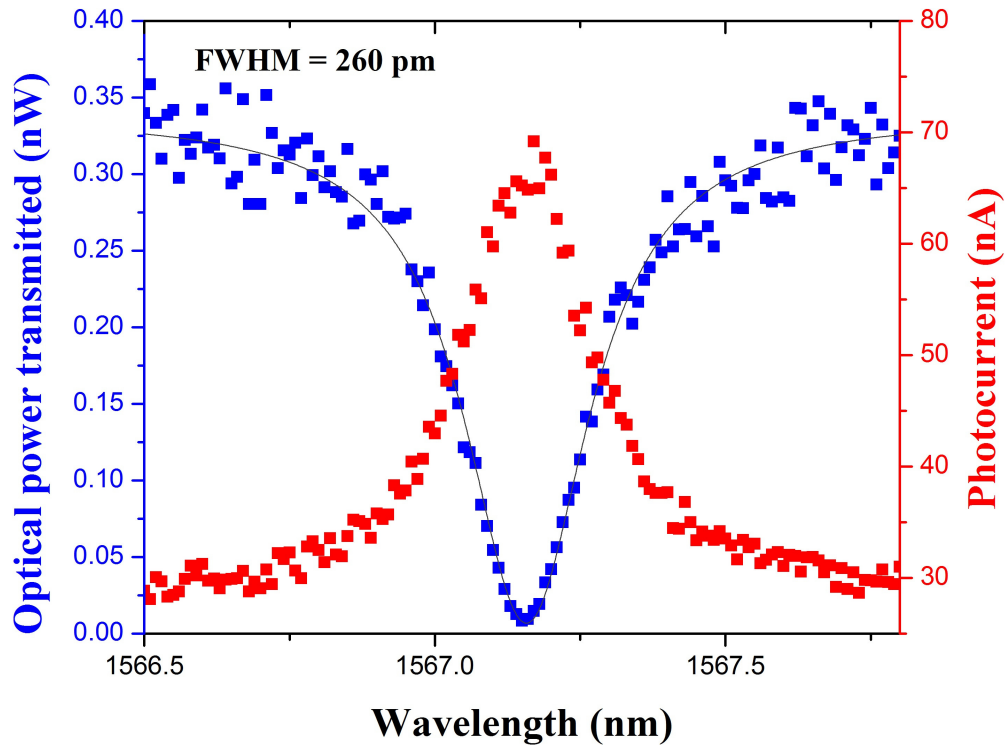


**Figure 3.10 |** Transmission and photocurrent spectra from a ring resonator with -50 dBm launch power. The ring diameter is 40  $\mu\text{m}$  and the photodiode was reverse biased at 30 V.

### 3.2.5 High-speed measurement results

In Figure 3.11a the normalized small signal frequency response is plotted for reverse bias voltages of 5, 10 and 15 V. A 3.5 GHz 3 dB bandwidth is seen at a reverse bias voltage of 15 V. A 5 Gbit/s eye diagram is shown in Figure 3.11b.

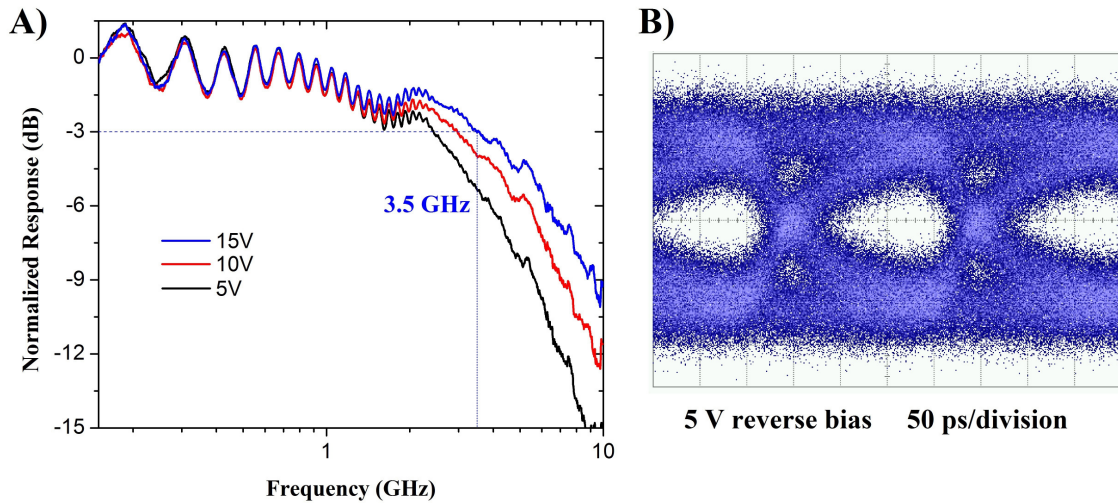


**Figure 3.11 | The normalized frequency response for three different bias voltages of the ring resonator based detector. (B) A 5 Gbit/s eye diagram.**

Although the devices indicate suitability for detection at the modest bandwidth of 3.5 GHz, a higher operational bandwidth might be expected. There are many possible factors influencing the speed of the devices. In order to examine the bandwidth limitation the influence of the experimental setup was first determined. The setup's high-speed capability was verified by measuring other (calibration) devices which achieved higher operational speeds. Therefore if there is some significant degradation of the response from the setup then it should not be evident at the speed of this ring detector.

As for the ring detector itself, the first potential limit on the operation speed examined was the photon lifetime within the ring. As described in chapter 2, the  $Q$  of a resonator describes the ratio between the energy stored (circulating photons) and the rate of energy lost (photon loss). The higher the  $Q$ , the longer photons will remain in the resonator. If the photon lifetime approaches that of the desired signalling rate, then the switching functionality of the resonator would be diminished. This is quantified by Eq. (3.12), which follows from chapter 2 section 2.4.5, which describes the operational bandwidth for a given  $Q$  and excitation wavelength. The measured device had a  $Q$  of approximately 10,000 at 1565 nm, imposing a limitation of

$$v_c = \frac{v}{Q} = \frac{c}{1565 \text{ nm} \cdot 10^4} = 19 \text{ GHz}. \quad (3.12)$$

This result is much higher than the measured bandwidth and therefore will have a limited effect on the total operation speed.

Another limit in operational speed which must be considered (in common with all photodetector structures) is the resistance-capacitance ( $RC$ ) limit. The capacitance of the photodiode was measured using a Boonton 7200 capacitance meter. Since the ring photodiode is very small and near the limit of the Boonton, similar devices longer in length were measured and the capacitance of the ring photodiode was obtained from extrapolation to be  $250 \pm 10$  fF. With a  $50 \Omega$  load resistance assumed (neglecting the resistance contribution of the doped silicon slab region) we can calculate the  $RC$  limited 3 dB bandwidth:

$$v_{RC} = \frac{1}{2\pi RC} = 12 \text{ GHz}, \quad (3.13)$$

and clearly this is not the primary limiting factor. Further confirmation of this conclusion was obtained from measurements of straight (non-resonant) waveguide detectors sharing the same chip area. These straight detectors were significantly longer than the circumference of the resonant photodiodes, and in fact showed better high-speed performance.

The final, classical limiting effect on the operation of a photodiode which is considered here is the transit time of the generated charge carriers, associated with their velocity. At a reverse bias of 15 V, if we assume a fully depleted junction width of  $1.5 \mu\text{m}$  and thermal saturation velocity is reached, ( $v_{sat} = 1 \times 10^7 \text{ cm/s}$ ), then the maximum carrier transit time is on the order of 15 ps. This is clearly not the source of the bandwidth limit as the rise and fall times in Figure 3.11 are approximately 150 ps. Although the small signal frequency response does show a dependence on voltage up to 15 V, further increases in bias voltage did not alleviate this limitation suggesting the saturation velocity was reached.

Upon further consideration and discussion, it was suggested that a possible source of the bandwidth limitation is operational instability. The small signal response of 3.5 GHz would typically result in a ‘cleaner’ eye diagram at 5 Gbit/s. In fact, in chapter 4 of this thesis, non resonant detectors of the same construction show a similar small frequency response but a much improved eye diagram. This discrepancy may be explained by the two measurement methods. With a small signal network analyzer measurement, steady state conditions are approximated and large fluctuations in carrier concentration are not present. In contrast, a bit pattern measurement introduces large fluctuations in carrier concentration which can lead to resonance instability. This is explored further in the next section.

### **3.3 High-speed resonant detection via defect states in silicon disk resonators**

#### **3.3.1 Overview**

In addition to the ring resonators of the previous section, microdisk *p-i-n* photodetectors were also fabricated and characterized at high speed. The devices are similar in construction to ring resonators whereby they are monolithic silicon devices which use a defect enhanced *p-i-n* photodetector incorporated onto a microdisk. The microdisk structure employed is a simple silicon pedestal, in essence it is a ring resonator where the centre of the ring remains unetched. Without the inner edge of a waveguide to confine light the optical modes differ from a ring with such a microdisk exhibiting ‘whispering gallery’ modes [13].

#### **3.3.2 Fabrication and device details**

The devices shared the same fabrication and characterization methods as the ring resonators in section 3.2. The disks themselves were created with diameters of 10 or 20  $\mu\text{m}$ , with bus waveguide widths of 350 nm and coupling gaps of 180 nm. The photodiode

occupied one half of the microdisk circumference. Phosphorous doping was 500 nm from the outside of the disk, while the boron doping was 1.5  $\mu\text{m}$  inside the disk edge for the 10  $\mu\text{m}$  diameter disk, and 2  $\mu\text{m}$  inside the disk edge for the 20  $\mu\text{m}$  diameter disk. Figure 3.12 shows an optical micrograph of the detector and a schematic diagram of the cross section.

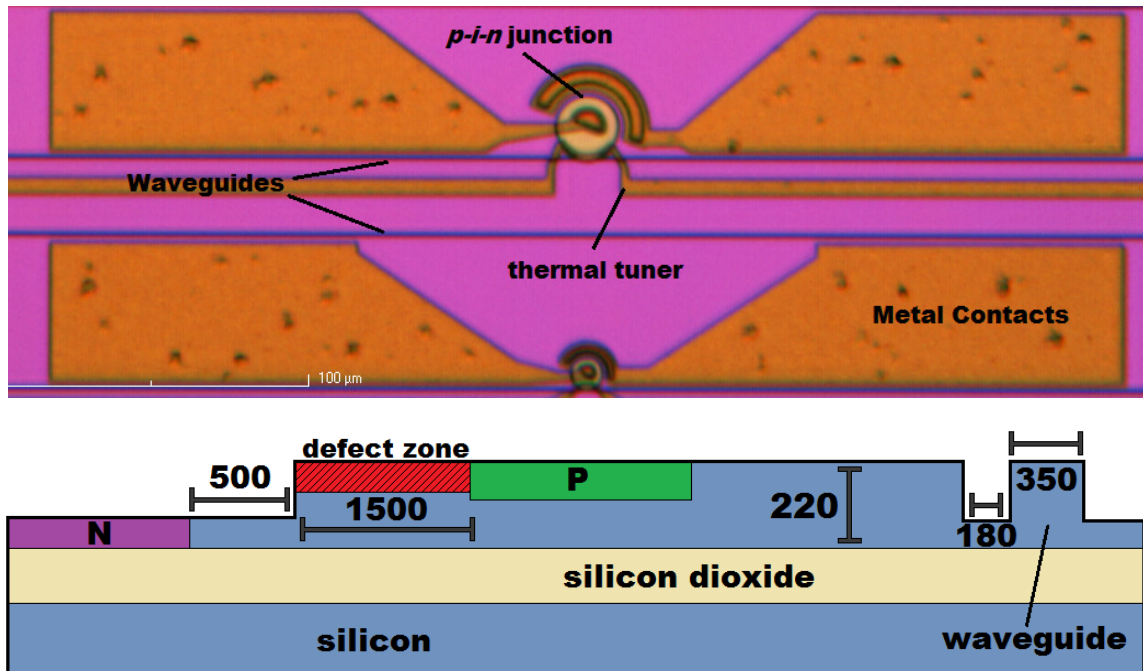


Figure 3.12 | An optical micrograph of microdisk photodetectors (10 and 20  $\mu\text{m}$  diameter) and a schematic diagram of the 10  $\mu\text{m}$  diameter microdisk (not to scale).

### 3.3.3 Continuous-wave characterization

The microdisks were characterized with a tunable laser in the same manner as the ring devices. In Figure 3.13 optical transmission and photocurrent spectra are shown for a 10  $\mu\text{m}$  diameter disk. There are three optical modes observed in the transmission spectrum, each showing a significantly different quality factor and photocurrent response. The two modes that show reduced photocurrent also show higher optical loss as indicated by the wider linewidth. These are likely the higher order modes which exist closer to the centre of the disk and thus nearer to the heavily doped  $p$  region. Due to the higher optical loss the power build-up is reduced and thus the photocurrent response is much lower than for the fundamental mode.

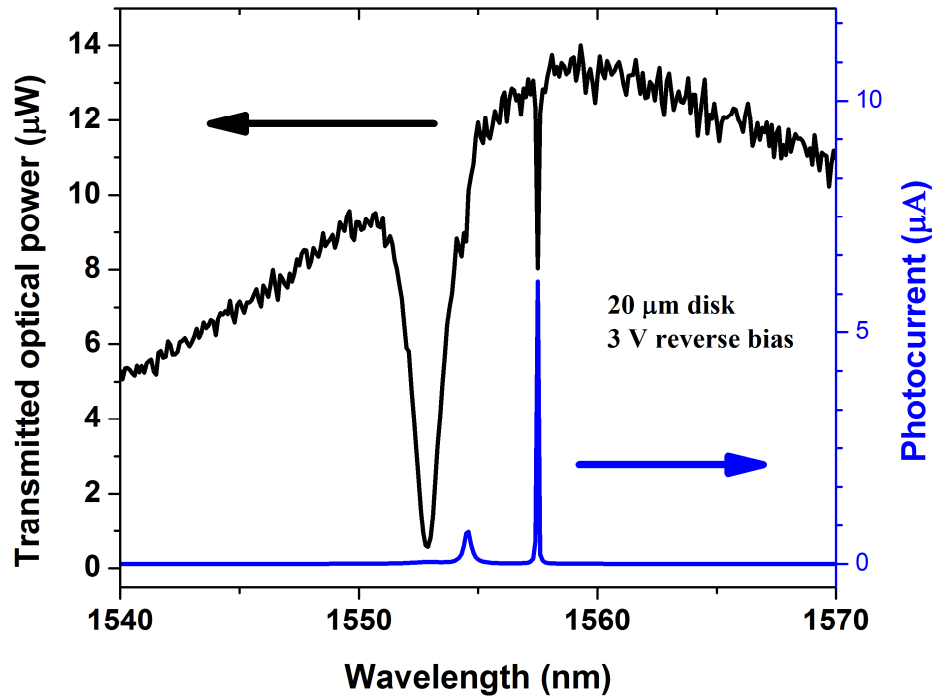
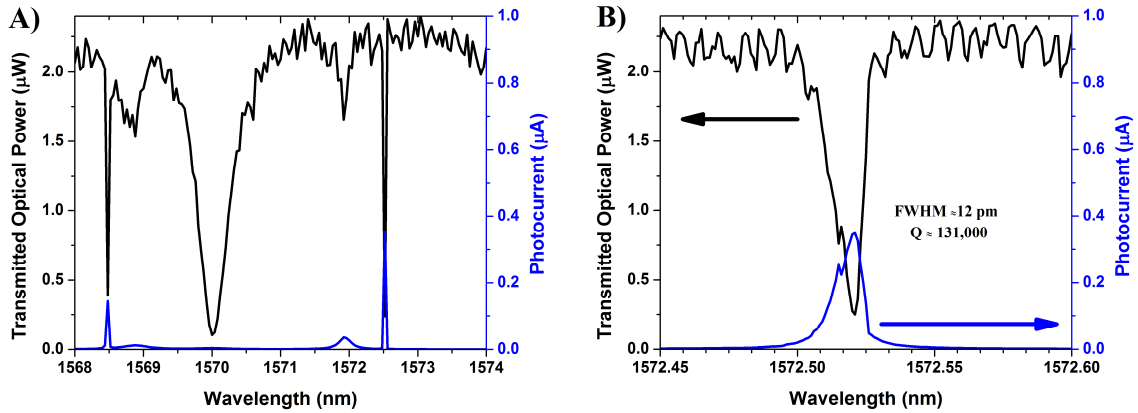


Figure 3.13 | Optical power transmitted and photocurrent as a function of wavelength for a 10  $\mu\text{m}$  diameter disk.

On the chip were ‘control’ microdisks which were masked during the post-fabrication ion implantation step. These disks still exhibit measurable photocurrent, and not surprisingly have a much higher  $Q$  than those with defects. In Figure 3.14 a 20  $\mu\text{m}$  diameter disk is shown that does not have defects. It has a linewidth of 12 pm and a  $Q$  of 131,000 for the resonance at 1572.52 nm. The  $Q$  obtained from these microdisks is very high compared to ring resonators, due to the lack of an inner sidewall. This in turn limits optical loss through scattering and surface-state absorption.



**Figure 3.14 | Transmission and photocurrent spectra of a 20  $\mu\text{m}$  diameter microdisk detector | (A) At 10 V reverse bias without ion implantation. (B) A finer scan of the resonance at 1572.5 nm.**

The microdisks that did not receive a defect implant still possessed measurable photocurrent on resonance. This response is due to surface-state defects at the Si-SiO<sub>2</sub> interface and two-photon absorption which is enabled by the optical intensity buildup for the high  $Q$  resonance. Figure 3.15 shows a direct comparison of the same microdisk design with and without defects. Approximately three times the level of photocurrent is seen in the detector with defects, meaning that even with reduced  $Q$  and two-photon absorption the defects still offer a significant net benefit.

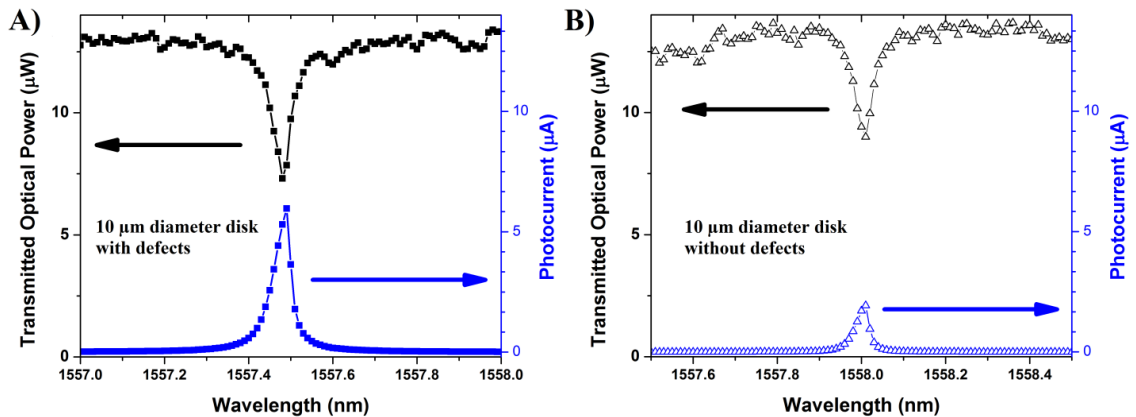


**Figure 3.15 | The optical transmitted power and photodiode current as a function of wavelength. The microdisks have a diameter of 10  $\mu\text{m}$  and are nominally identical A) Defects present. B) No defects present.**

### 3.3.4 Continuous-wave power loading

The buildup of intensity within micro-resonators presents a problem in the form of the creation of excess heat, a direct consequence of confined optical absorption. This heating increases the refractive index of the silicon, causing a red-shift in the resonant wavelength.

The impact on the resonance location can be significant. In Figure 3.16 spectra from a 20  $\mu\text{m}$  diameter disk resonator detector are shown for three different optical power levels of 0.2, 5 and 10 mW. Figure 3.16.a shows the optical power versus wavelength, while Figure 3.15.b shows the corresponding photocurrent.

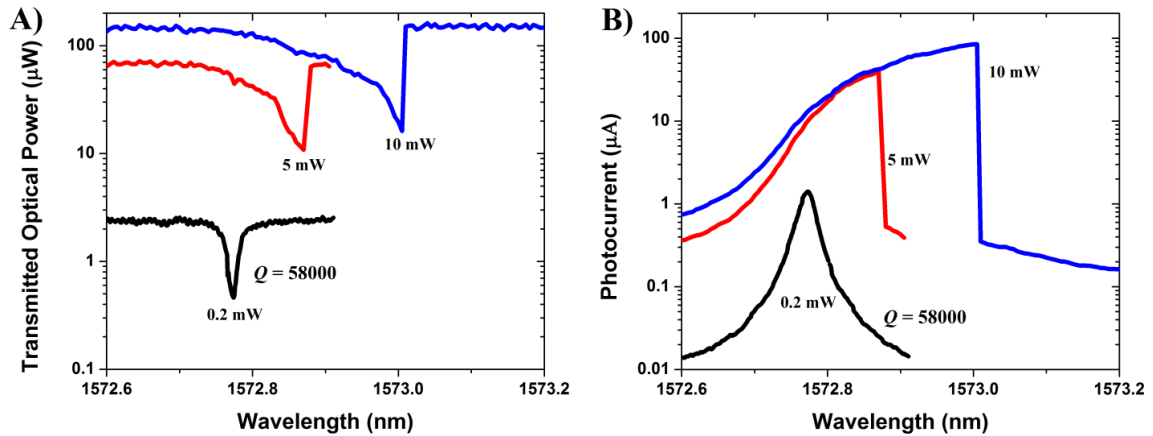


**Figure 3.16 | Optical power versus wavelength (left) and photocurrent versus wavelength (right) for a 20  $\mu\text{m}$  diameter disk resonator. Optical power launched at the grating coupler is labelled for each spectra.**

This thermal shifting will strongly depend on the  $Q$  of the resonator, which in this case is 58,000. This effect is less pronounced in detectors with a lower  $Q$ , due to the lower power build-up, but cannot be ignored.

Temperature control structures, like the resistive metal strip integrated on these detectors, can provide some compensation but thermal tuning is typically limited to the kHz regime [14]. In data transmission applications temperature control would become an issue, but signals can be encoded to achieve a balanced average power. That is, to prevent long chains of ‘off’ or ‘on’ states (zeroes and ones) so that the average thermally

dissipated power remains constant. This encoding reduces the data rate, but can remedy problems associated with thermal loading.

### 3.3.5 Frequency response

The microdisk frequency response was characterized with the same experimental setup used for the microring resonators described earlier in this chapter. The normalized small signal frequency response is shown in Figure 3.17.a. At resonance there is a 3 dB bandwidth of approximately 4 GHz, similar to the ring resonator devices in the previous section. However with the laser moved 100 pm off-resonance the frequency response is increased to approximately 7 GHz.

An eye pattern of the disk photodiode was also recorded. Figure 3.17.b shows a 10 Gbit/s eye diagram for a 20  $\mu\text{m}$  diameter disk with a reverse bias of 15 V. This result was recorded off-resonance and is consistent with the 7 GHz small signal bandwidth result.

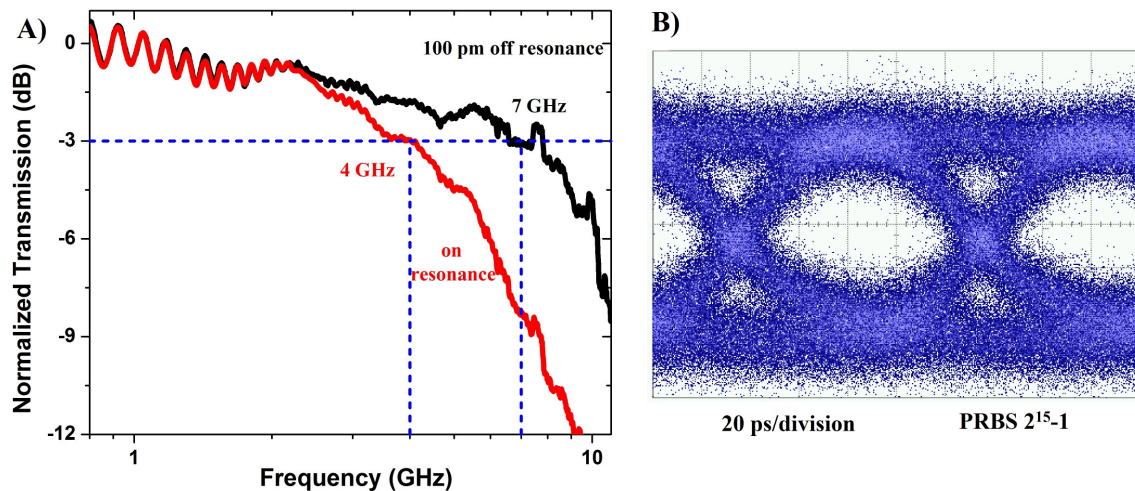


**Figure 3.17 | High-speed operation of a 20  $\mu\text{m}$  diameter microdisk photodetector at 15 V reverse bias. (A) The small signal frequency response, the 3 dB bandwidth is reduced from 7 GHz to 3 GHz on resonance. (B) A 10 Gbit/s eye diagram of the microdisk operating off resonance with a reverse bias of 15 V.**

In Figure 3.18 bit patterns for a 20  $\mu\text{m}$  diameter microdisk are shown for various wavelength displacements from resonance. When off-resonance the devices are ‘well

behaved', with the bit pattern resembling a square wave, as seen in the first frame at a wavelength of 1572.719 nm. At this point the bit pattern corresponds to the eye diagram in Figure 3.17.b; it is noisy due to the low optical power but remains open. As the wavelength approaches resonance the behaviour is no longer uniform, consistent with power buildup during consecutive 'on' states. Examining the pattern at a wavelength of 1572.889 nm, a relatively clean bit-rate pattern is seen up until the centre division of the plot, when several consecutive 'on' states occur and the power loading nearly doubles. In the last frame, 1573.011 nm, which is closest to resonance, the signal quality is degraded for the entire bit train. In this case the varying levels of the on-off states results in a closed eye diagram.

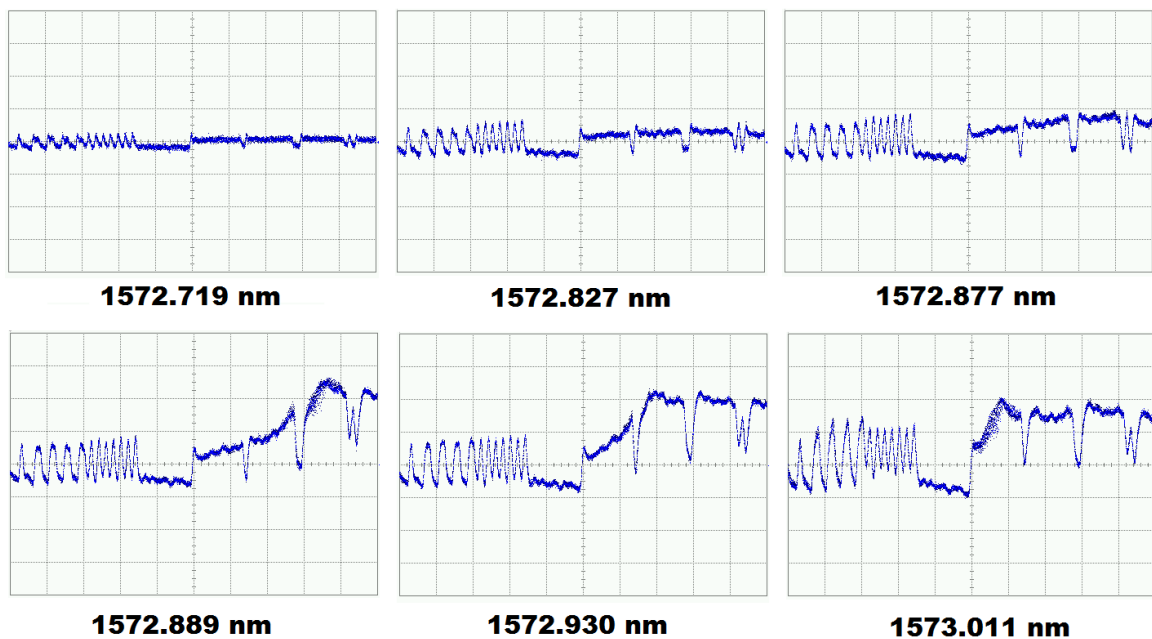


**Figure 3.18 | 5 Gbit/s bit patterns from a 20  $\mu\text{m}$  diameter microdisk detector for various wavelengths near resonance. The device was not stable on resonance, but showed an open eye off resonance. The timescale is 2 ns/division while the vertical scale is 30 mV/division.**

The microdisk thus is displaying a power dependent instability, the successive 'on' states pose a problem, and show a relatively fast power buildup on a scale less than 10 ns.

We can consider the photon lifetime of this resonance, which is 27 ps and corresponds to a  $Q$  of approximately 58,000. The resulting photon lifetime is given by

$$t_c = \frac{Q}{\omega} = \frac{58000 \cdot \lambda}{2\pi c} = 48 \text{ ps.} \quad (3.14)$$

The photon lifetime limited bandwidth is then

$$\nu_c = \frac{1}{2\pi t_{\text{phot}}} = 3.3 \text{ GHz.} \quad (3.15)$$

These values are consistent with the ‘on resonance’ small signal bandwidth result in Figure 3.16 and the fall time seen in Figure 3.17. The resonator is being limited by photon lifetime, but the large fluctuation in power is a separate issue.

Temperature instability is a potential issue when operating on resonance as greater power absorption would result in a higher temperature, inducing a resonance shift to higher wavelengths. Yet in this case the laser is operating at a wavelength less than resonance, therefore a thermal red-shift would increase the laser’s relative offset from the resonance peak. This increase in the laser offset would reduce the optical power coupled into the resonator, which is contrary to what is observed from Figure 3.18 where repeated ‘on’ states result in greater power. Additionally, the timescale of this effect is on the order of nanoseconds, far too short for typical thermal events on a 20  $\mu\text{m}$  diameter device.

### 3.3.6 Carrier concentration modulation as a cause of instability

The presence of free carriers in a silicon waveguide impacts the refractive index [10]. During operation the number of carriers is fluctuating as light enters the resonator, photons are absorbed, and free carriers are generated. The changing carrier concentration could shift the resonance position, altering the amount of light present in the resonator.

We consider a critically coupled ring resonator for simplicity. In this case, all loss is assumed to occur within the ring and therefore this represents the on resonance case after the ring has undergone the maximum shift due to carrier generation. Scattering losses are much lower than loss due to absorption and will be ignored. We will assume that every absorbed photon generates an electron-hole pair, but ignore effects due to avalanche

carrier multiplication. Given an incident power absorbed  $P_i$ , the generation rate of electron-hole pairs is then

$$\rho_{EHP} = \frac{P_i}{V_{wg} E_{phot}}, \quad (3.16)$$

where  $V_{wg}$  is the waveguide volume (*cross-sectional area x ring circumference*) and  $E_{phot}$  is the photon energy in Joules. Carriers are swept out of the ring due to the electric field, with an average lifetime  $\tau_{avg}$  given by the time needed to travel half the junction width:

$$\tau_{avg} = \frac{W}{2v_{sat}}, \quad (3.17)$$

where  $v_{sat}$  is the saturation velocity  $1 \times 10^7$  cm/s and  $W$  is the junction width. The steady state concentration of electrons is reached on timescales much longer than the average lifetime. With  $\tau_{avg} \approx 10$  ps, and a bit pattern of 5 Gbit/s, an ‘on’ bit would be 200 ps long and the carrier concentration would approach the steady state value, where the production rate of carriers is equal to the rate at which they are removed. The carrier concentration is then

$$\Delta N = \rho_{EHP} \tau_{avg} = \frac{P_i W}{V_{wg} E_{phot} 2v_{sat}}. \quad (3.18)$$

From the Soref relations [10] we can calculate the refractive index shift

$$\Delta n = - \left[ 8.8 \times 10^{-22} \frac{P_i W}{V_{wg} E_{phot} 2v_{sat}} + 8.5 \times 10^{-18} \left( \frac{P_i W}{V_{wg} E_{phot} 2v_{sat}} \right)^{0.8} \right], \quad (3.19)$$

and using Eq. (3.9) the refractive index shift of the silicon can be converted to a shift in the resonance wavelength:

$$\Delta \lambda = \frac{\Delta n_{Si}}{n_g} \frac{dn_{eff}}{dn_{Si}} \lambda. \quad (3.20)$$

The resonance blue-shift is plotted as a function of the optical power (in the bus waveguide) in Figure 3.19, for the case of a 10  $\mu\text{m}$  radius ring resonator with a

waveguide width of 500 nm and a height of 220 nm with a 50 nm slab. This example assumes that the ring is critically coupled and absorption losses dominate scattering loss. In this situation no optical power exits down the bus waveguide and all absorption generates free carriers within the ring waveguide.

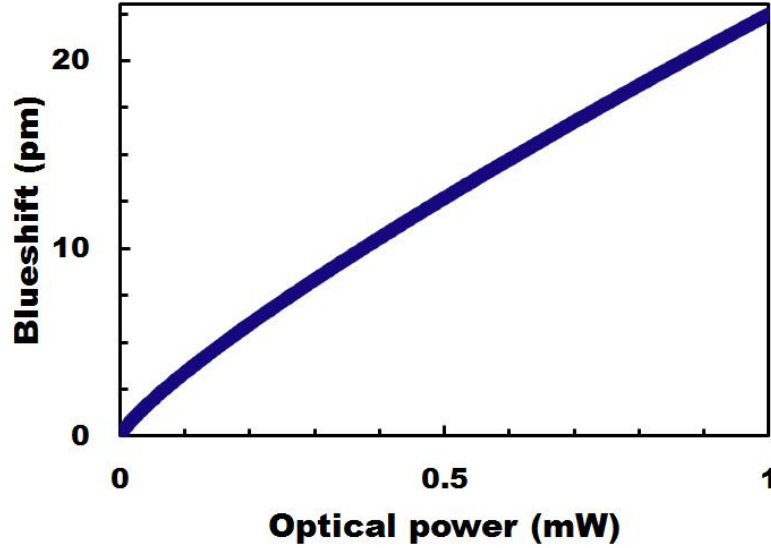


**Figure 3.19 | A model of the blue-shift versus optical power in the bus waveguide for a 10  $\mu\text{m}$  radius critically coupled ring resonator. The wavelength is 1550 nm and the  $p$ - $n$  junction width is 1.5  $\mu\text{m}$ .**

Such a wavelength shift is detrimental to detector operation as it would introduce variation in the sensitivity of the detector. This effect was not observable with continuous-wave measurements. This may be due to a counteracting thermal shift which masks the blue-shift during continuous-wave measurements. This effect is evident at high-speed operation due to the difference in time constant for the thermo-optic and free carrier effects in silicon. We thus describe the high-speed modification of the resonance point through:

$$\Delta\lambda = \lambda - \lambda_0 = -\frac{dn_{eff}}{n_g} \frac{\lambda_0}{dn_{Si}} \left[ 8.8 \times 10^{-22} \frac{P(\lambda)_i W}{V_{wg} E_{phot} 2v_{sat}} + 8.5 \times 10^{-18} \left( \frac{P_i W}{V_{wg} E_{phot} 2v_{sat}} \right)^{0.8} \right]. \quad (3.21)$$

### 3.3.7 The shift in the imaginary index

As we have seen, the modulation of the real part of the refractive index due to the presence of carriers can negatively impact resonant detection. The imaginary part of the refractive index will also change, and any change of the loss within a resonator will change the build-up factor of the device. The build-up factor influences the responsivity, so this is an important consideration.

Following the example describe above, we can use the Soref relation [10] which describes the change in optical absorption due to the presence of free carriers,

$$\Delta\alpha = [8.5 \times 10^{-18} \Delta N_e + 6 \times 10^{-18} \Delta N_h]. \quad (3.22)$$

An optical power level of 1 mW within the bus waveguide of a critically coupled all-pass resonator would lead to an increase in  $\alpha$  of  $0.12 \text{ cm}^{-1}$  in the silicon. Typical intrinsic waveguide loss close to 3 dB/cm, or  $\alpha = 0.69 \text{ cm}^{-1}$ , and resonant detectors in this chapter show loss several times higher than this. The impact of a changing loss on the build-up factor for an all-pass ring resonator is given by the equation

$$\frac{I_3}{I_1} = \left| \frac{E_3}{E_1} \right|^2 = \frac{(1-t^2)a^2}{1+(ta)^2 - 2ta \cos(\delta)}, \quad (3.23)$$

where ‘ $a$ ’ is the single round trip amplitude transmission, given by  $a = e^{-\alpha L}$ . On resonance, we can plot this relation for different values of the transmission coefficient ‘ $t$ ’, shown in Figure 3.20. For a 10  $\mu\text{m}$  radius ring an increase in  $\alpha$  of 0.12 would reduce the value of ‘ $a$ ’ by 0.01. This may have a significant impact in the limiting case of  $t = 0.99$ . However the loss of an implanted ring is several times higher than intrinsic waveguide loss (as seen from the earlier passive resonator results), meaning that ‘ $a$ ’ values close to 1 (and ‘ $t$ ’ values) are generally not achieved in this type of resonant detector. This rules out the steepest part of the curve in Figure 3.20, ensuring a small reduction in the build-up factor due to carrier concentration changes. As a reminder, this calculation assumes bias

sufficient for carrier saturation velocity. In the case of no bias the resulting free carrier concentration would be much higher.

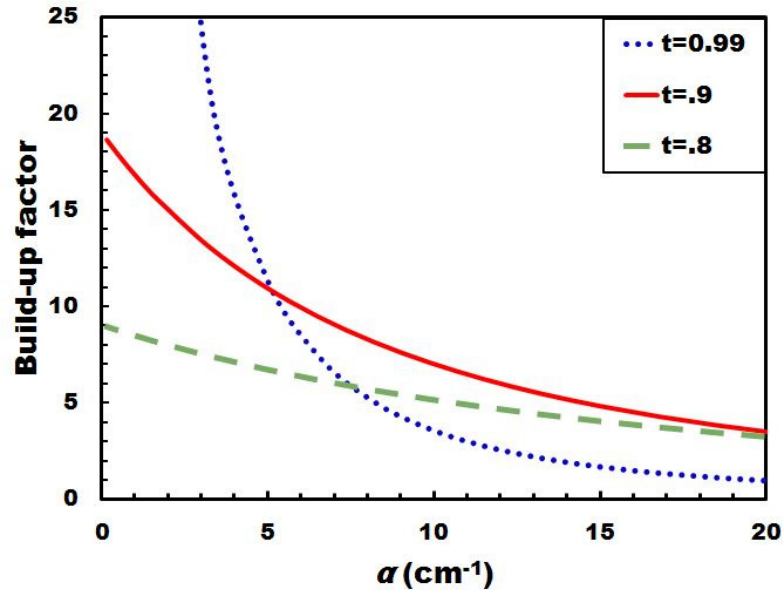


Figure 3.20 | The build-up factor of a ring resonator versus the attenuation coefficient.

Beyond the modifications due to free carrier concentration, other phenomenon could influence the build-up factor. These include two-photon absorption, and potentially the saturation of lattice defects.

### 3.4 Summary

This chapter introduced a study of defects in SOI waveguide resonators, followed by characterization of microring and microdisk resonator detectors.

The study of ion implantation in SOI waveguide resonators determined the refractive index shift associated with the introduction of lattice defects. The resulting shift was larger for defects than an equivalent concentration of free carriers. This process is a potential method for post-fabrication ‘trimming’ of resonant devices. Defects can be easily incorporated through ion implantation and removed via thermal annealing.

The frequency response of microring resonators were characterized. Both the small signal response and large signal response was recorded. The results showed lower bandwidth than expected. Possible limitations included: the  $RC$  limit, photon lifetime limit, carrier transit time and defect lifetime. However all of these considerations can be eliminated as similar defect based detectors have shown stable operation at higher speeds as results in chapter 4 of this thesis will demonstrate. The microring is thought to be limited by resonance instability.

The bandwidth limitation was explored in more detail with results from a microdisk photodetector. The microdisks possess a higher  $Q$  than the microring and therefore demonstrate greater resonance instabilities. Based on the observations of the microdisk, a simple model was suggested for carrier induced refractive index shift and subsequent instability in resonant detectors. The model shows that a significant resonance shift can accompany absorption, thus impacting the photocurrent response. The changing refractive index poses a challenge for a resonant detector operating at high power. Due to the extreme sensitivity of the devices they are likely not suitable for high-speed photodetection where dynamic operating points are required.

Low power detection is a potential niche for these detectors as the issues of resonance stability are avoided and the ring characteristics can be exploited as a highly responsive low power detector in sensing applications. The resonant structure provides a build-up of optical power within the ring, and the photodiode itself can be greatly shortened thus reducing the dark current.

In summary, the resonant detectors presented in this chapter have several strengths: a compact footprint, low dark current, enhanced responsivity on resonance and optical filter functionality. These benefits mean there is potential use for resonant detectors in lower power sensing applications, such as spectroscopy or as a channel monitor combined with an optical filter. However they are less suitable for high-speed data transfer as they suffer from instabilities.

## References

1. Logan, D.F. *et al.* Defect-enhanced Silicon-on-insulator Waveguide Resonant Photodetector With High Sensitivity at 1.55  $\mu\text{m}$ . *IEEE Photon. Technol. Lett.* **22(20)**, 1530 (2010).
2. Doylend, J.K., Jessop, P.E. and Knights, A.P. Silicon photonic resonator-enhanced defect-mediated photodiode for sub-bandgap detection. *Opt. Express* **18(14)**, 14671–14678 (2010).
3. Wright, N.M. *et al.* Free carrier lifetime modification for silicon waveguide based devices. *Opt. Express* **16(24)**, 19779–19784 (2008).
4. Pelaz, L., Marqués, L.A. and Barbolla, J. Ion-beam-induced amorphization and recrystallization in silicon. *J. Appl. Phys.* **96(11)**, 5947 (2004).
5. Foster, P.J. *et al.* Optical attenuation in defect engineered silicon rib waveguides. *J. Appl. Phys.* **99(7)**, 073101 (2006).
6. Doylend, J.K. Defect-mediated photodetectors for silicon photonic circuits. PhD. Thesis, *McMaster University* (2010).
7. Fallahkhair, A.B., Li, K.S. and Murphy, T.E. Vector finite difference modesolver for anisotropic dielectric waveguides. *J. Lightwave Technol.* **26(11)**, 1423-1431 (2008).
8. Gardes, F.Y. *et al.* High-speed modulation of a compact silicon ring resonator based on a reverse-biased pn diode. *Opt. Express* **17(24)**, 21986–21991 (2009).
9. Rouger, N., Chrostowski, L. and Vafaei, R. Temperature effects on silicon-on-insulator (SOI) racetrack resonators: A coupled analytic and 2-D finite difference approach. *J. Lightwave Technol.* **28(9)**, 1380–1391 (2010).
10. Soref, R.A. and Bennett, B.R. Electrooptical effects in silicon. *IEEE J. Quantum Elec.* **23(1)**, 123-129 (1987).
11. Ziegler, J.F., Ziegler, M.D. and Biersack, J.P. SRIM–The stopping and range of ions in matter (2010). *Nucl. Instrum. Meth. B.* **268(11)**, 1818-1823 (2010).

12. Shafiiha, R. *et al.* Silicon waveguide coupled resonator infrared detector. in *Proc. of Optical Fiber Communication Conf./Natl. Fiber Optic Engineers Conf.*, Paper No. OMI8 (2010).
13. Soltani, M., Yegnanarayanan, S. and Adibi, A. Ultra-high Q planar silicon microdisk resonators for chip-scale silicon photonics. *Opt. Express* **15(8)** 4694-4704 (2007).
14. Atabaki, A.H. *et al.* Optimization of metallic microheaters for high-speed reconfigurable silicon photonics. *Opt. Express* **18(17)**, 18312-18323 (2010).

# Chapter 4    Avalanche High-Speed Photodetectors

## Overview

In the previous chapter the limitations of resonant enhanced detectors were discussed. The dominant result was that resonant instabilities interfere with high-speed operation. This chapter will describe non-resonant detectors operating in the avalanche regime with results presented for both high-speed and continuous-wave operation. The detector design has similarities with the ring resonator detectors in chapter 3; that is a *p-i-n* junction on a sub-micron silicon-on-insulator (SOI) rib waveguide with ion implantation of the intrinsic region to introduce lattice defects for enhanced absorption.

There are multiple design iterations described in this thesis, each fabricated through multi-project wafers, facilitated by CMC Microsystems. This approach offered excellent fabrication quality and volume which was not achievable otherwise. However the relatively long design and fabrication cycle (> 6 months) limited the total number of fabrication runs over the course of the PhD work. Subsequent experimental results will be presented in chronological order with the focus being operational speed. Reports on continuous-wave (or steady-state) characterization will not be repeated for each device set because the results are not wholly different between fabrication runs.

The first section of this chapter will discuss devices which were fabricated at CEA-LETI in Grenoble, France, followed by devices fabricated at IME A\*STAR in Singapore.

The results reported in this chapter have formed the basis of the research journal publication:

Ackert, J.J. *et al.* 10 Gbps silicon waveguide-integrated infrared avalanche photodiode. *Opt. Express* **21**(17), 19530-19537 (2013).

## 4.1 LETI devices

### 4.1.1 Design and fabrication

Detectors were fabricated at CEA-LETI with their 193 nm deep-ultraviolet lithography process on SOI wafers with a top silicon thickness of 220 nm and a buried oxide layer thickness of 2  $\mu\text{m}$ . The silicon waveguides were created from a 170 nm etch, leaving a silicon slab height of 50 nm. A 1  $\mu\text{m}$  thick oxide layer was deposited over the waveguides to isolate them from an Al/Cu metal contact layer. Boron and phosphorous ion implantations at a dose of  $2 \times 10^{14} \text{ cm}^{-2}$  formed the diodes. To allow for absorption in the infrared, ion implantation was used to create deep-level defects. A variety of implantation conditions and annealing temperatures were performed via post-fabrication implantation. In these cases, photolithography at McMaster was used to create a photoresist mask prior to selective ion implantation.

The photodiodes were incorporated onto waveguides with a width of 500 nm which had doped regions situated 500 nm from the waveguide sidewall. The detector lengths ranged from 200 to 800  $\mu\text{m}$ . Figure 4.1 is a schematic cross section of the detector. Shallow-etch grating couplers were designed to facilitate Transverse-Electric mode coupling at a wavelength of 1550 nm. Such couplers have been previously characterized in the results of chapter 3 and provide a total loss from fiber to fiber of 15 dB.

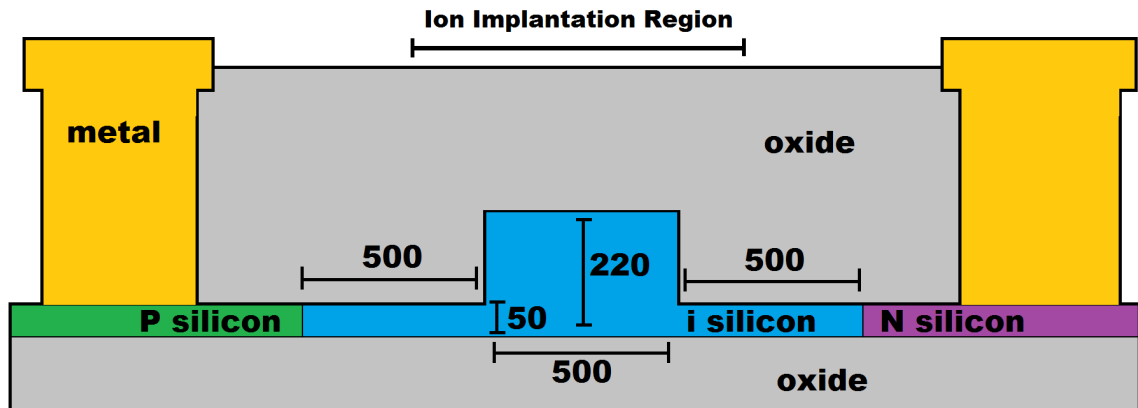
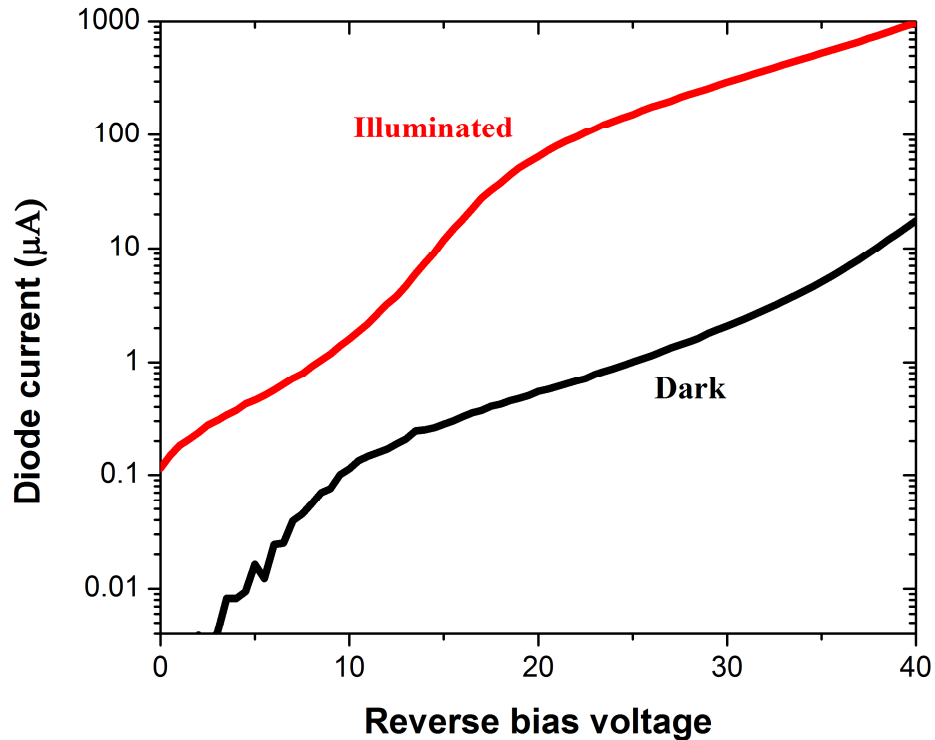


Figure 4.1 | A schematic cross-section of the LETI detector with dimensions shown in nanometers (not to scale).

#### 4.1.2 Continuous-wave characterization

The detectors show a high responsivity in the avalanche regime, in Figure 4.2 the current-voltage (IV) characteristic is shown for a 600  $\mu\text{m}$  long photodiode. The optical power coupled to the waveguide was estimated to be 200  $\mu\text{W}$ , giving a responsivity of 4.7 A/W at 40 V reverse bias. To maintain reasonable dark current levels of less than a few microamps, a likely operating point of 30 V would be chosen where the responsivity is 1.5 A/W. Optical loss in the photodiode's absorption region was 86 dB/cm, although this value is dependent on the implant dose and specific annealing treatment.



**Figure 4.2 | Current versus reverse bias voltage for a 600  $\mu\text{m}$  long photodiode from the LETI fabrication run.**

High responsivity is an important consideration in any photodetector, as is a linear response with optical power. For instance, an ideal photodetector would maintain the same responsivity across a large range of incident optical power. Saturation or non-linear optical effects can influence the response, which can occur with relatively modest coupled power levels because of the extremely small cross section of the waveguide.

A 200  $\mu\text{m}$  long photodetector was measured with varying level of optical input power. The laser power was reduced using an integrated optical attenuator built into the Agilent 81640A tunable laser. Figure 4.3 shows the photodiode current as a function of estimated waveguide coupled power. The photocurrent shows linear behaviour from -30 dBm to 3 dBm, demonstrating that the detector can be useful for both high and low power applications.

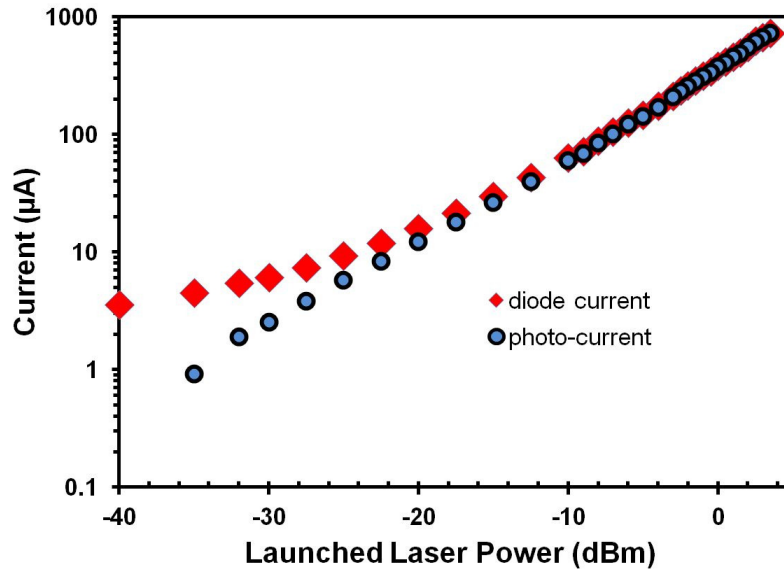


Figure 4.3 | The photodiode current as a function of launched power for a 200  $\mu\text{m}$  long photodiode (LETI) with a reverse bias voltage of 40 V. Upon subtracting the dark current of 3.5  $\mu\text{A}$ , linear operation is seen from -30 to 3.5 dBm. An estimated 7 dBm is lost to coupling.

### 4.1.3 Temperature response

The variation in performance as a function of ambient temperature for photodetectors (and indeed any integrated device) dictates the operational application. In the case of the current devices this is further complicated because the responsivity of defect mediated detectors is dependent on a relatively low post-process annealing temperature. The defects introduced from ion implantation can be removed at temperatures less than 300  $^{\circ}\text{C}$ , as described in the previous chapter of this thesis.

The detectors were exposed to temperatures up to 275  $^{\circ}\text{C}$  and the photocurrent response was measured together with the change in optical power transmitted. Figure 4.4 shows the photocurrent and optical loss versus temperature for an 800  $\mu\text{m}$  long device at 40 V reverse bias. The annealing steps were done in atmospheric conditions for 5 minutes at each temperature. In between annealing steps the samples were characterized. The necessity to remove the chip from the optical setup for annealing at each step introduced random alignment error. However a clear trend is seen: as the temperature increases the photocurrent response increases. Above 300  $^{\circ}\text{C}$  a drop in response was observed (not

shown); thus the experiment did provide a guide to an optimal post-process annealing. It is noteworthy that previous devices have had defect states which have annealed out at lower temperatures. This particular sample received a silicon implant with an energy of 1 MeV and a dosage of  $1.4 \times 10^{12} \text{ cm}^{-2}$ .

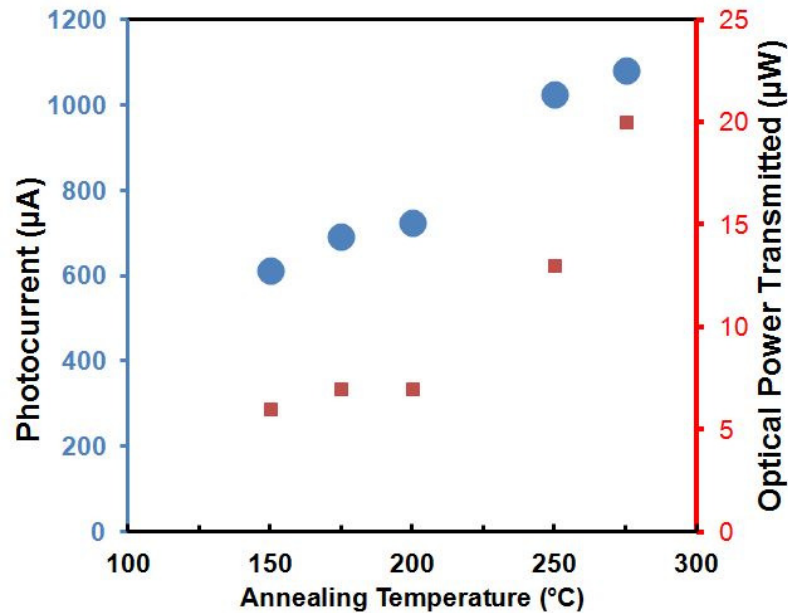


**Figure 4.4 | The annealing response of an 800 μm LETI detector at 40 V reverse bias. The photocurrent and transmitted optical power is represented after various annealing temperatures. Each annealing step was 5 minutes in air at the specified temperature. The implantation used silicon at an energy of 1 MeV and a dosage of  $1.4 \times 10^{12} \text{ cm}^{-2}$ .**

The temperature limitations imposed by defect annealing will impact the fabrication of a larger photonic integrated circuit using this detector. The consequence is that the ion implantation step which introduces the lattice defects must be done after dopant activation and metallization processes, as these processes require temperatures in excess of 400 °C.

The temperature response of an operating device was also investigated using a temperature controller and a thermoelectric cooler mounted within the sample stage. The temperature was adjusted from 20 to 70 °C, the upper limit achievable with this thermoelectric cooler, and the current-voltage characteristic was measured. Figure 4.5 shows the photocurrent response with temperature for a reverse bias of 35 V and 10 V.

With increasing temperature the device showed increasing photocurrent, as well as an expected increase in dark current.

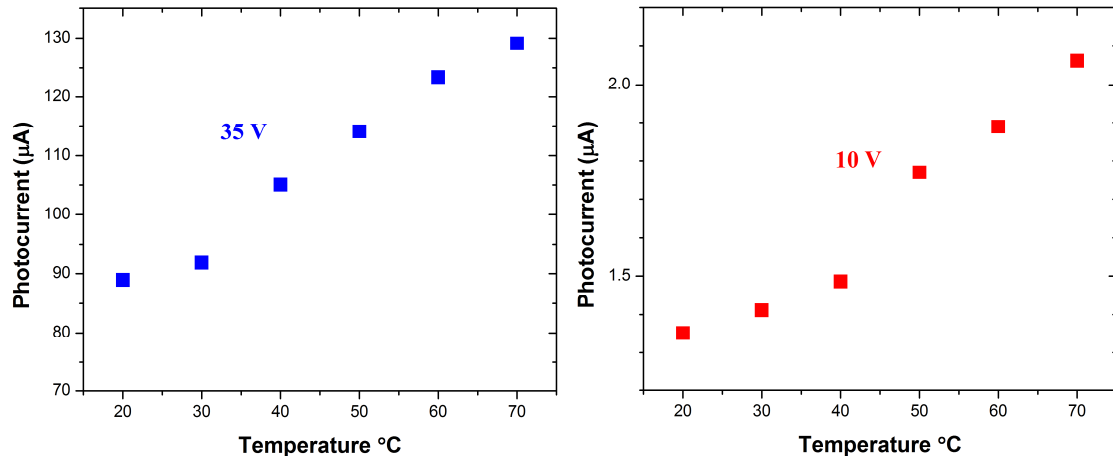


**Figure 4.5 | The photocurrent of a 200  $\mu\text{m}$  long photodiode (LETI) with varying environmental temperature and reverse bias of 35 V and 10 V.**

The temperature response is somewhat unexpected for an avalanche detector, where in the general case increasing the temperature will reduce the gain and subsequent photocurrent. With a higher temperature, free carriers are more likely to undergo phonon scattering. The higher chance of scattering means that ionizing collisions are less likely to occur, as the phonon scattering extracts energy from the carriers. This should reduce the gain of the diode for a specific applied voltage. However these detectors show an increase in photocurrent with temperature which is of similar margin for both low and high bias. The increase is attributed to a more efficient defect mediated excitation process, as is present at 10 V when there is little avalanche gain.

This response demonstrates that the photodiode can be operated in a substantial range of ambient temperature, a necessary property in data communication.

#### 4.1.4 Wavelength dependence

The wavelength dependence of the detector was measured within the operating limitations of the grating couplers (approximately 100 nm). Figure 4.6 shows the transmitted optical power versus wavelength, plotted alongside the photocurrent versus

wavelength, both in arbitrary units normalized to the peak wavelength value close to 1565 nm. The optical spectrum represents the wavelength sensitivity of the two grating couplers (input and output). The waveguide itself has a wavelength dependent loss, however over this range it is assumed to be small in comparison to the influence of the grating couplers.

The response of the detector is representative of the optical transmitted power, taking into account light entering the detector only passes through one wavelength sensitive grating coupler. This indicates that there is no significant feature in the detector's response spectrum in the important telecommunications *C* band, and sections of the *S* and *L* bands. We can infer from this plot, and the absorption plots of [1], that the photodetector can operate over a wide wavelength region (in contrast to competing technologies such as those based upon germanium integration). In chapter 6 a demonstration of response beyond wavelengths of 2  $\mu\text{m}$  will be reported.

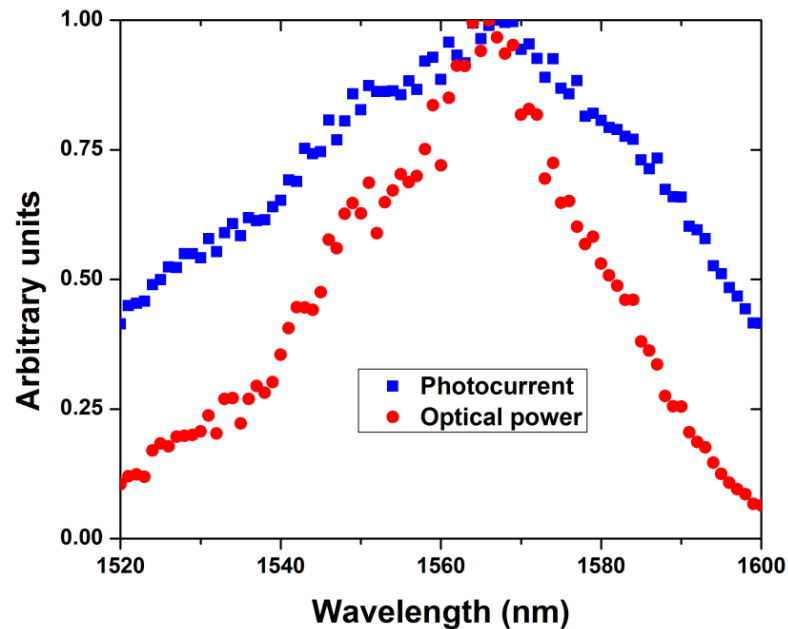


**Figure 4.6 | The photocurrent versus wavelength for a defect implanted photodetector (blue) and the transmitted optical power through the photodetector waveguide (red). The profile for the transmitted power falls off more rapidly as it passes through two wavelength-sensitive grating couplers.**

#### 4.1.5 High-speed results

The detectors were measured at high speed in collaboration with researchers at Queen’s University, Kingston, Canada. The small signal frequency response of the device was determined using a lightwave network analyzer (LNA) rated for 20 GHz and operating at 1550 nm. A source-measure unit (Keithley 2400) and a 20 GHz bias tee were used to apply a bias voltage and measure the photocurrent. For large signal measurements, a pulse pattern generator (PPG) driving an optical modulator followed by an erbium-doped fiber amplifier was used to generate a 10 Gbit/s optical non-return-to-zero on-off keying signal incident on the photodiode. An equivalent time sampling oscilloscope was subsequently used to measure the eye diagram of the generated photocurrent. Figure 4.7 is a block diagram of the high-speed characterization setup.

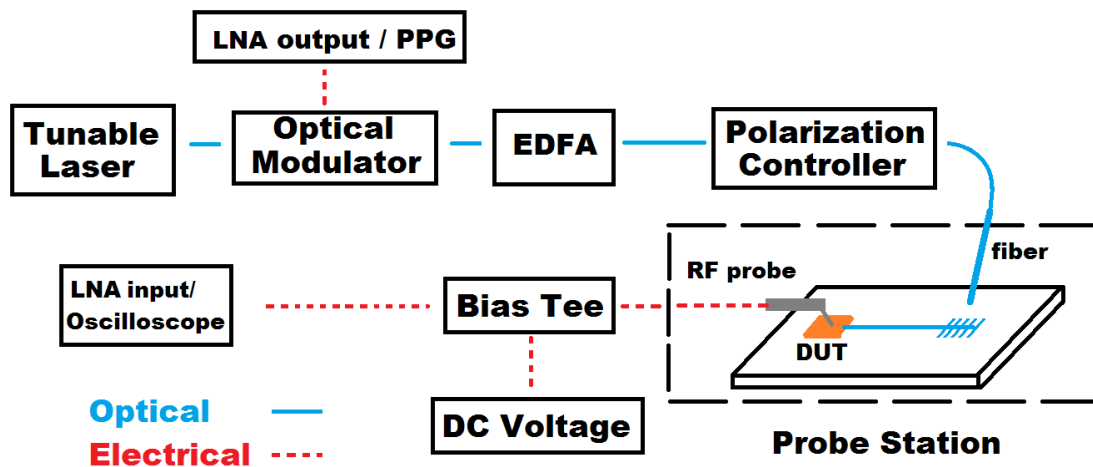
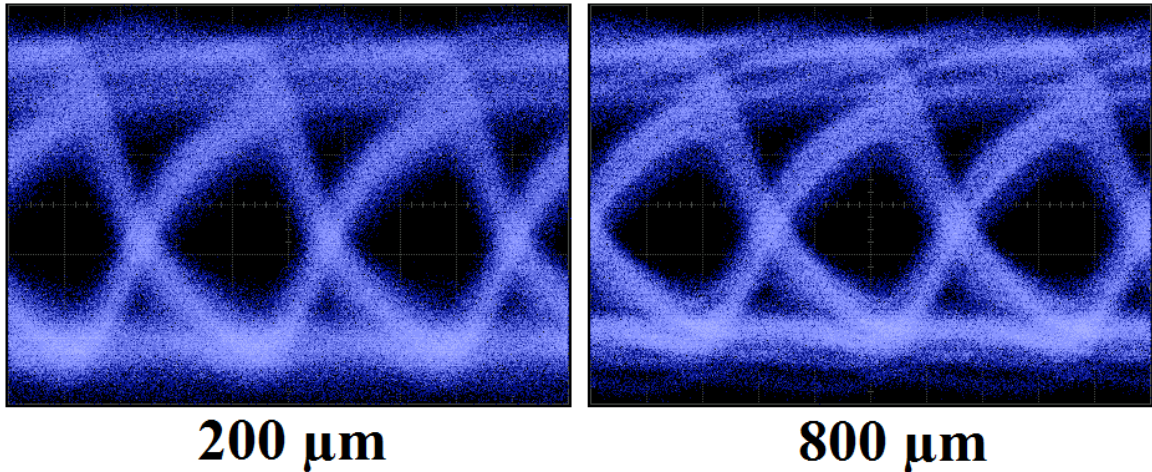


Figure 4.7 | A block diagram of the high-speed characterization setup for LETI photodiodes. Small signal measurements used the LNA while eye diagrams were taken with the PPG and oscilloscope.

The devices were found to operate with an open eye diagram at 10 Gbit/s. Shown in Figure 4.8 are eye diagrams for both a 200  $\mu\text{m}$  and 800  $\mu\text{m}$  device. While the 800  $\mu\text{m}$  device shows a larger signal (as expected), the general characteristic of the eyes are similar, with a fall time of approximately 60 ps.



**Figure 4.8 | A comparison of 10 Gbit/s eye diagrams between an 800  $\mu\text{m}$  and a 200  $\mu\text{m}$  long detector (LETI), with otherwise identical configuration. The timescale is 30 ps/division. The vertical scale is 3.7 mV/div for the plot 200  $\mu\text{m}$  device, and 8.2 mV/div for the 800  $\mu\text{m}$  device.**

Small signal measurements were also carried out with the LNA. Figure 4.9 shows the normalized response versus frequency for three device lengths, 200, 600 and 800  $\mu\text{m}$ . The result shows again that the performance is similar. In fact the 200  $\mu\text{m}$  device shows the smallest bandwidth but this is attributed to measurement difficulties for this detector as opposed to the true response.

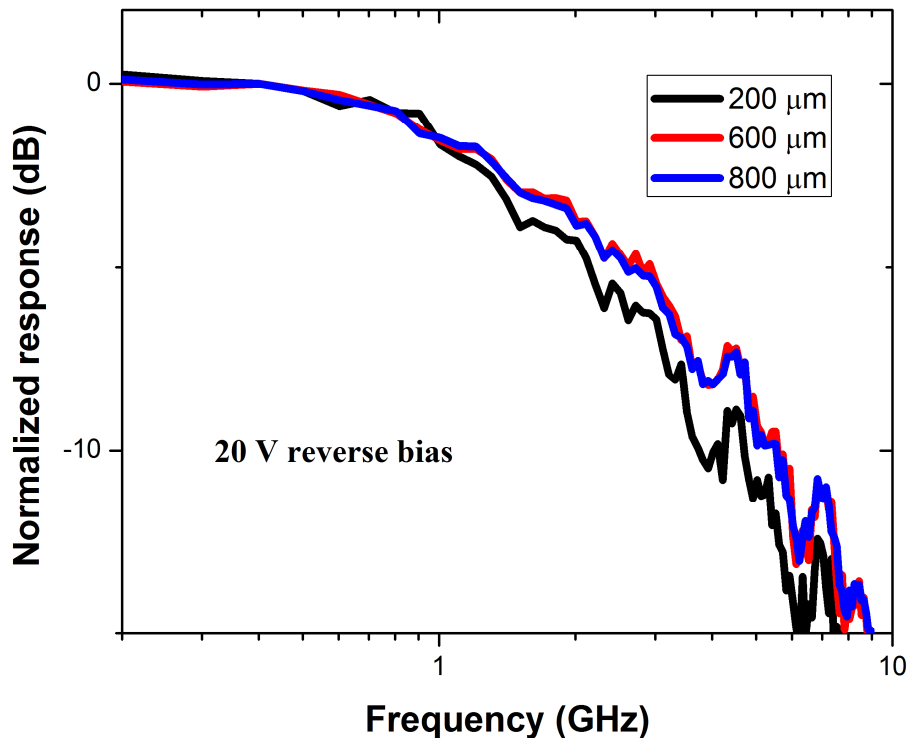
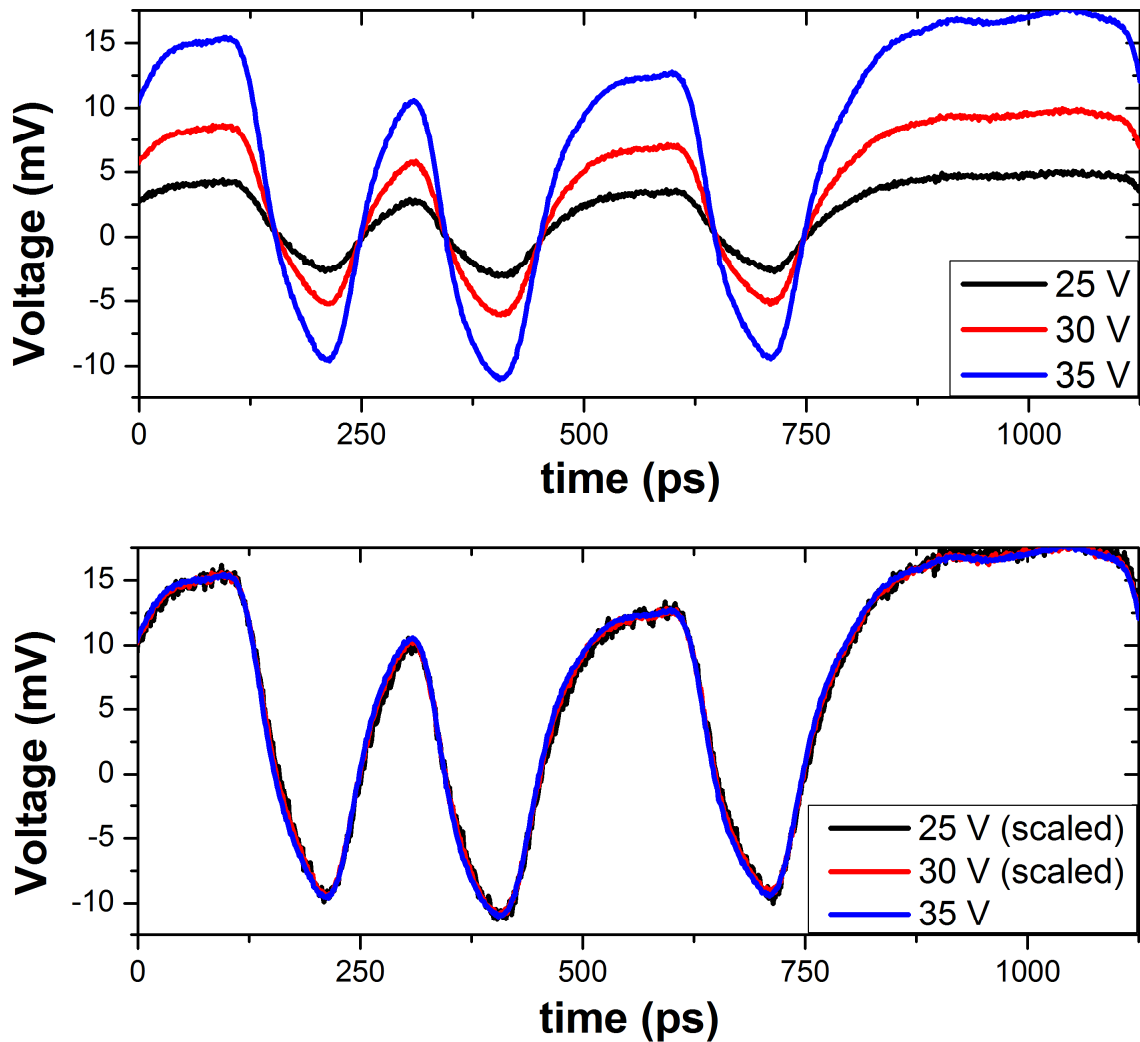


Figure 4.9 | The normalized frequency response of three LETI detectors of length 200, 600 and 800  $\mu\text{m}$  operating at a reverse bias of 20 V.

The effect of operation voltage on device performance was also studied. This can impact behaviour in two ways: (1) variation in carrier transit time (with an inadequate electric field the excited carriers are not swept out of the absorption region before the next light pulse arrives); (2) variation in avalanche multiplication. As the voltage increases the multiplication factor increases, eventually limiting the bandwidth of the detector as the avalanche process takes some time to end after the light pulse has been absorbed.

A 10 Gbit/s bit pattern was recorded for a 200  $\mu\text{m}$  device and is shown in Figure 4.10 for three different reverse bias conditions. Included in the figure are two plots: A) is the original data for 25, 30 and 35 V, while B) shows the same data but with the 25 and 30 V traces linearly scaled to match the amplitude of the 35 V trace. After scaling it can be clearly seen that the bit pattern of the device remains constant for each bias condition. Measurement for lower biases was not possible due to the reduced responsivity which was insufficient for measurement.



**Figure 4.10 | Measured waveforms for a 200  $\mu\text{m}$  long device for reverse bias of 25, 30 and 35 V. The upper figure shows the original measured waveforms for a 10 Gbit/s signal. In the lower plot, the traces were linearly scaled.**

This result shows that the frequency response is unchanged between 25 and 35 V, which indicates that the carrier transit time has been minimized. This also shows that the avalanche gain has no detrimental effect up to a reverse bias of 35 V.

Moving beyond 35 V a decline in the frequency response was observed. The device of Figure 4.10 was not recorded with a bit pattern at 40 V, however small signal measurements of a 600  $\mu\text{m}$  detector were taken at a reverse bias of 35 and 40 V. At 40 V there is a noticeable drop in performance, which is shown in Figure 4.11. At 35 V the 3

dB bandwidth is 2 GHz while at 40 V it is reduced to 0.85 GHz. This reduction is attributed to the gain limitation on the response time of the detector

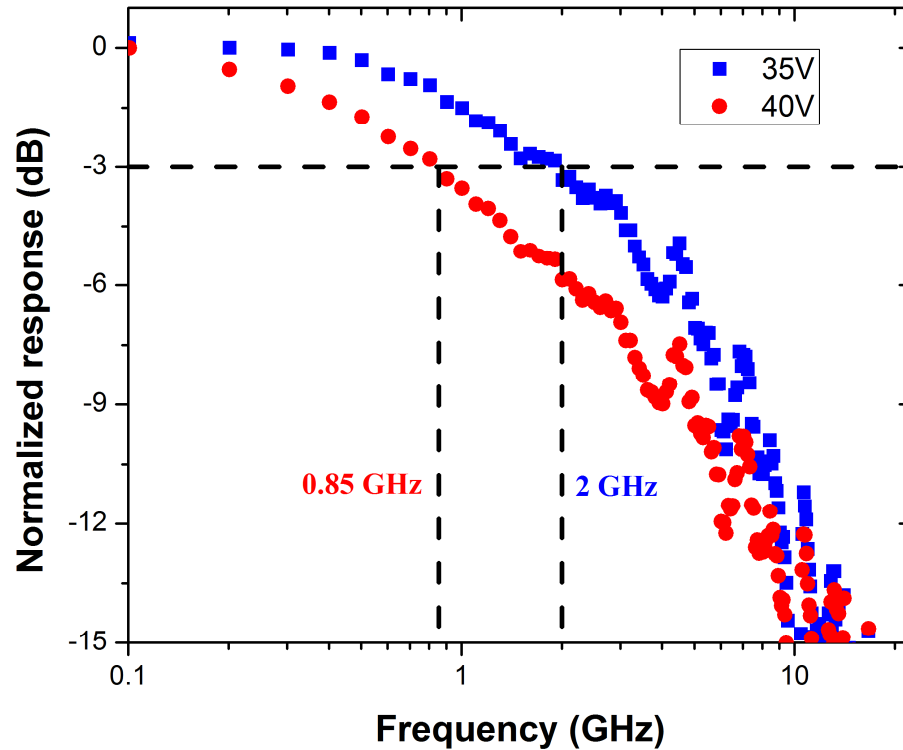


**Figure 4.11 | The normalized frequency response for a 600  $\mu\text{m}$  long detector (LETI ) with a reverse bias of 35 and 40 V. At 40 V a degradation in the response is seen, which is attributed to avalanche multiplication.**

Given that the operating point of such a device would likely be below 35 V to maintain a reasonable dark current, this was deemed to be a very encouraging result.

#### 4.1.6 Bandwidth limiting factors

The capacitance of a range of devices was measured to determine the operational speed limit. In Figure 4.12 the capacitance of several device lengths are plotted. The 800  $\mu\text{m}$  long detector had a capacitance of 1300 fF, but a linear fit results in a non-zero y-intercept value. This residual value was not observed in other capacitance measurements using the same experimental configuration, so it remains uncertain as to whether it was measurement inaccuracy or related to the device itself.

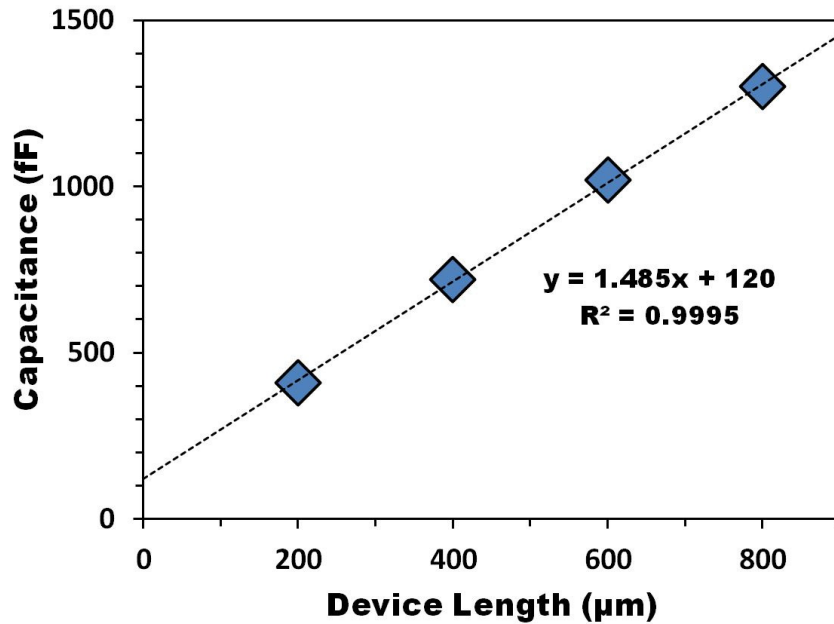


Figure 4.12 | The capacitance of the LETI photodetectors for multiple device lengths.

We can then calculate the  $RC$  limited bandwidth which is given by

$$f_{3dB} = \frac{1}{2\pi RC}. \quad (4.1)$$

The resistance is not directly measured, but if we assume a negligible resistance from the doped silicon and take the load resistance value of  $50 \Omega$ , then the limitation imposed by a capacitance of  $1300 \text{ fF}$  for the  $800 \mu\text{m}$  long device is  $2.44 \text{ GHz}$ . This is consistent with the observed results from Figure 4.9, and therefore the likely speed limitation.

## 4.2 Devices fabricated at IME\*ASTAR (Singapore)

### Overview

Following the promising results from the LETI detectors, a fabrication run at IME A\*STAR Singapore included both resonant and non-resonant detectors. While the resonant photodiodes did not yield significantly different results as those reported in chapter 3, improvements were seen in the non-resonant devices compared to those

reported above. As this was the first of three fabrication runs at IME A\*STAR reported in this thesis, the devices in this section will be labelled IME #1.

#### 4.2.1 Fabrication

The devices were fabricated using the 248 nm optical lithography platform. The waveguides were 500 nm wide and formed in a 220 nm thick layer of silicon over 2  $\mu\text{m}$  of buried oxide. Boron and phosphorous implants in the 50 nm thick slab region formed a *p-i-n* junction. The doped regions were separated 500 nm from the waveguide sidewall. Post-IME fabrication was performed in order to introduce defects into the waveguide region. The lithography was performed at McMaster University and the devices were implanted at the University of Western Ontario. The results presented here are for a boron implantation dose of  $1 \times 10^{12} \text{ cm}^{-2}$  with an energy of 1050 keV and annealed at a temperature of 200  $^{\circ}\text{C}$  for 5 minutes in air ambient. The propagation loss of this sample was measured to be 83 dB/cm. A schematic diagram of the detector cross section is shown in Figure 4.13.

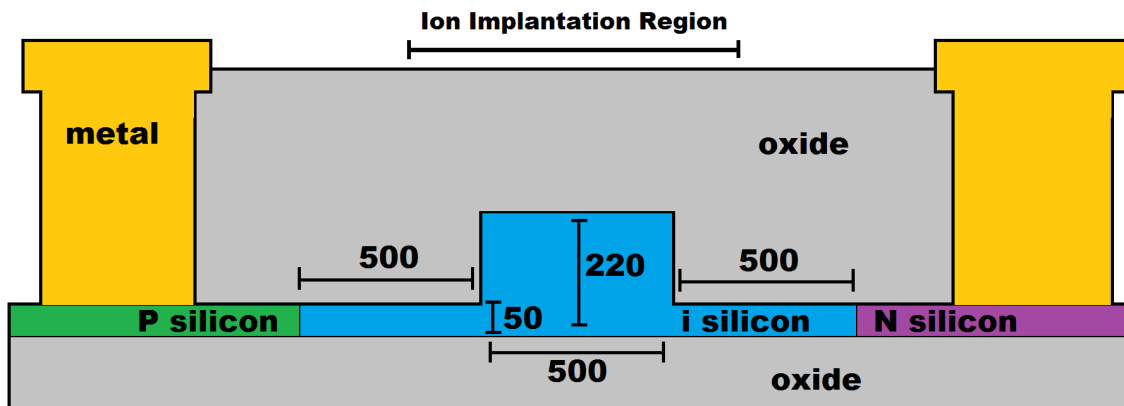
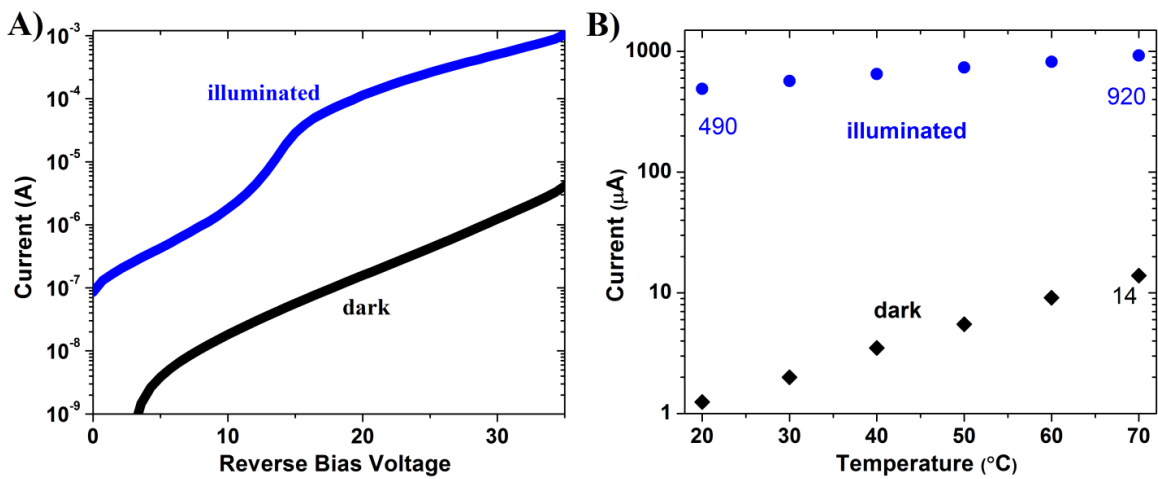


Figure 4.13 | A schematic cross-section of the IME #1 photodetector. Dimensions are shown in nanometers (not to scale).

#### 4.2.2 Continuous-wave results

Continuous-wave results were generally similar to those seen for the LETI devices described in section 4.1, with observed differences attributed to the varying implantation

and annealing conditions. In Figure 4.14.a the current-voltage characteristic is shown for a 1 mm long photodiode with an estimated waveguide coupled power of -7 dBm at a wavelength of 1565 nm. The estimated external responsivity (based on waveguide coupled power) at 35 V is 5 A/W, with a dark current of 4  $\mu\text{A}$ . In Figure 4.14b the temperature response of the device is shown from 20  $^{\circ}\text{C}$  to 70  $^{\circ}\text{C}$  at a reverse bias of 30 V. The photocurrent nearly doubles across this temperature range, while the dark current increases from approximately 1  $\mu\text{A}$  to 10  $\mu\text{A}$ .



**Figure 4.14 | Current measurements for a 1 mm long photodiode (IME #1) A) Current versus reverse bias voltage at 20  $^{\circ}\text{C}$ . B) Current versus temperature at 30 V reverse bias.**

### 4.2.3 High-speed results

The devices were measured at Queen’s University with a similar experimental configuration as described in section 4.1.5. An additional measurement included was a bit-error rate test (BERT). A BERT compares the output signal from a pattern generator to the received signal from the photodetector, providing a quantitative analysis of the detector’s performance. The BERT system lacked the sensitivity of the oscilloscope and thus required the use of a transimpedance amplifier (TIA). We employed a Micram TIA-56, rated for operation at 56 Gbit/s. Figure 4.15 shows the schematic diagram of the test setup. Small-signal frequency response measurements were also taken, with the same

experimental setup described in section 4.1.5. This simply requires the LNA to replace the PPG and BERT, and the removal of the TIA.

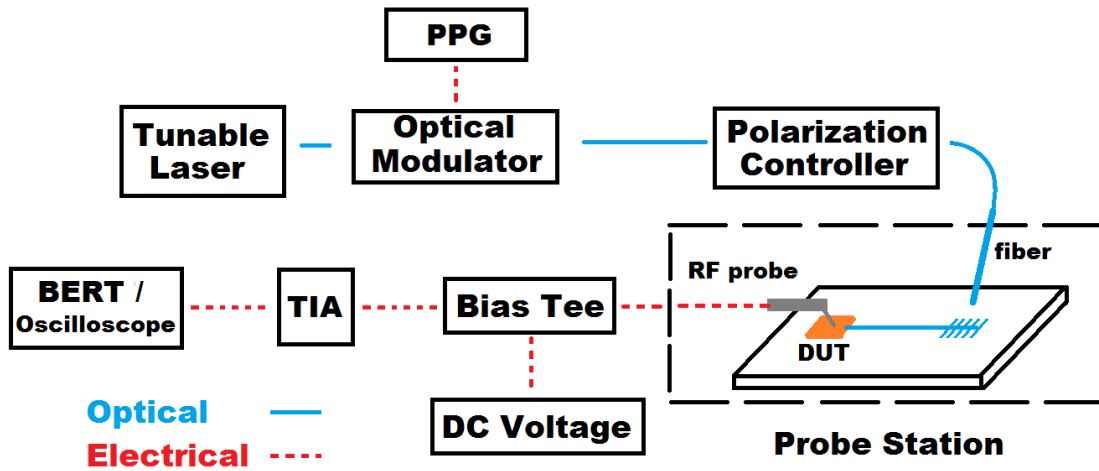


Figure 4.15 | A block diagram of the experimental setup for bit error rate tests for the IME #1 detector.

The small signal frequency response was recorded at a reverse bias of 35 V and is shown in Figure 4.16. A 3 dB bandwidth of 3.25 GHz is seen, a small increase over the previously described LETI chips considering the increased length of 1 mm versus 800  $\mu\text{m}$ .

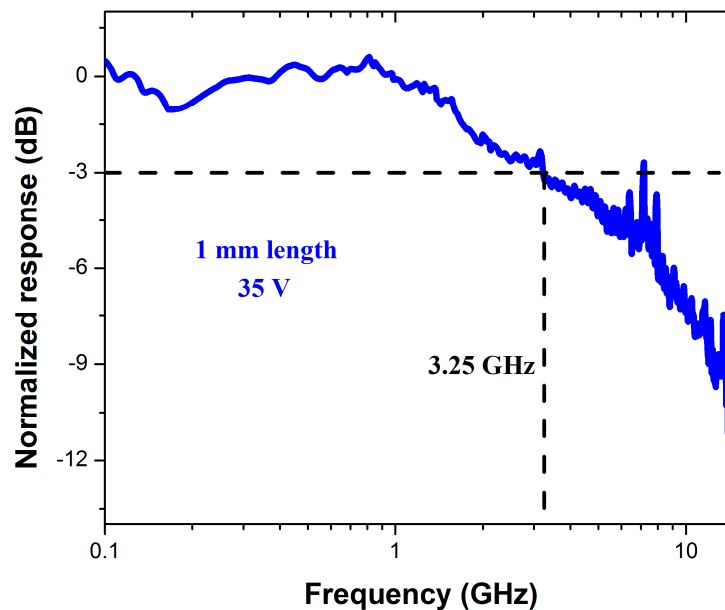
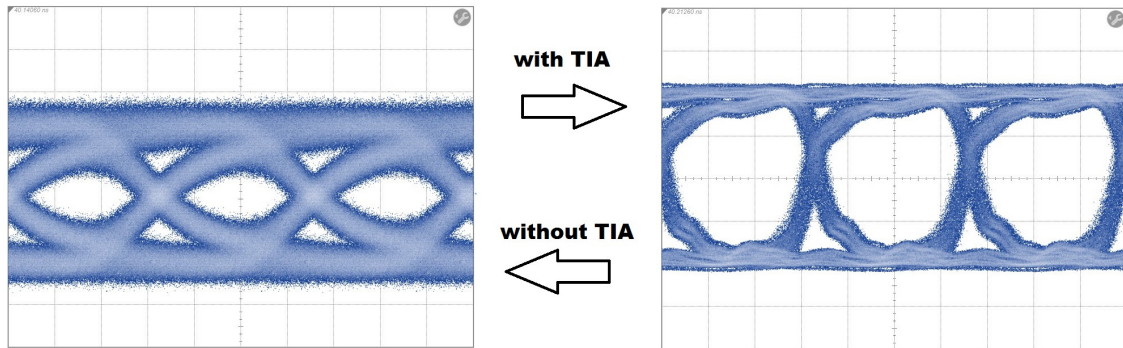


Figure 4.16 | The small-signal frequency response of a 1 mm photodiode (IME#1).

The eye diagram of the device can be seen in Figure 4.17. Shown on the left is the case without the TIA in use. Shown on the right is the device with the TIA (as required for the BER measurement). With the use of the TIA the eye diagram appears much more open or square. The TIA contains a limiting amplifier, thus changing the relative shape of the eye by bounding the output voltage.



**Figure 4.17 | Eye diagrams for a 1 mm long detector (IME#1). Left – The unamplified signal. Right- The signal with the transimpedance amplifier used. The voltage amplitude scale with the TIA was 70 mV/div, without the TIA it is 8.2 mV/div. The time scale is 30 ps.**

A BER measurement was performed for a 1 mm long detector. The results are shown in Figure 4.18 for a reverse bias of 25, 30 and 35 V. The BER is shown as a function of waveguide coupled average power. This power estimate was based on transmission measurements which included the entry coupler, waveguide detector and exit coupler. The assumption of equal loss for entry and exit couplers was made. Error-free operation is accomplished for all three bias levels, with the required optical power level decreasing with increasing bias. At 35 V reverse bias and -10 dBm waveguide coupled power, the detector is operating with a bit-error rate better than  $1 \times 10^{-12}$ .

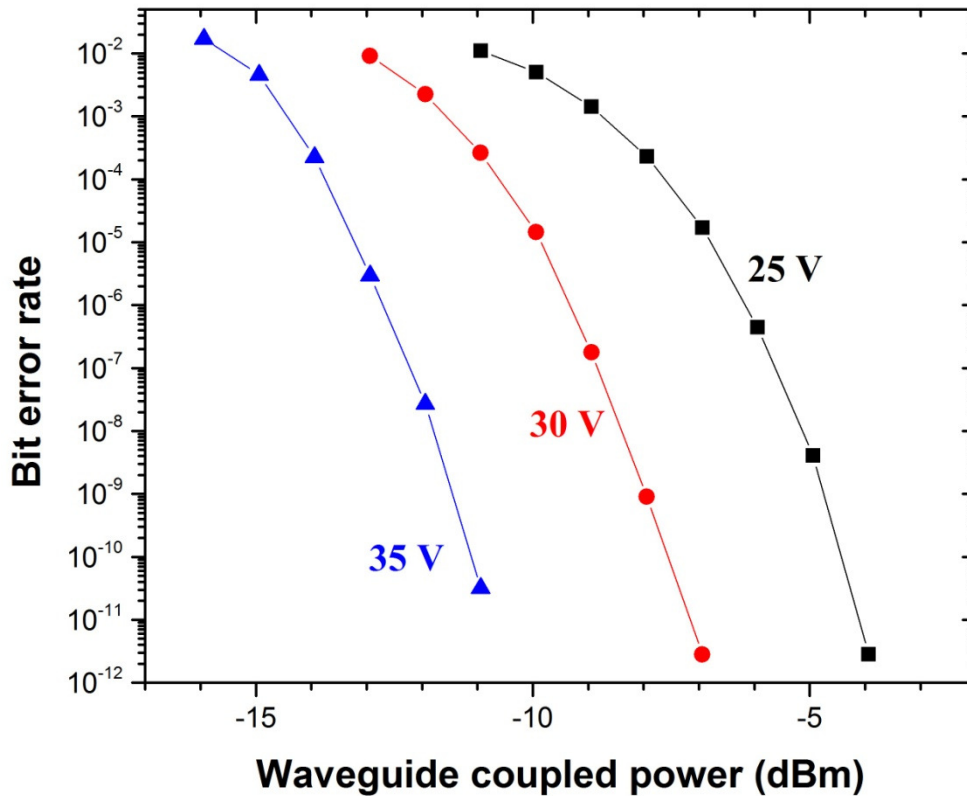


Figure 4.18 | Bit-error rate at 10 Gbit/s versus waveguide coupled power for a 1 mm IME #1 device at three levels of reverse bias.

These are significant results as they demonstrate the low noise potential of the detectors into the avalanche regime at a reverse bias of 35 V. For an optical receiver, a sensitivity metric is defined by the minimum power at which error-free operation is observed. Error-free is often defined with a bit-error rate better than 1 error per terabit ( $\text{BER} < 10^{-12}$ ). However Forward Error Correction (FEC) methods provide a means for data links to accommodate higher bit-error rates and thus function with a lower received optical power. The penalty for these error checking schemes is a reduction in data rate, called ‘overhead’ [2]. Many fiber optic systems employ a 7% overhead, where a sequence of bits is translated into a coded sequence 7% longer than the original. For example, the RS(255, 239) code, where 255 coded bits represent 239 original bits, communication with a BER less than  $10^{-12}$  requires an original uncoded BER less than  $10^{-4}$ .

Commercially available avalanche photodiode receivers operate error-free below -20 dBm, suggesting a performance gap between the current integrated detector and discrete III-V semiconductor solutions. The device presented here is not fully optimized and more sensitivity may yet be found with different defect concentrations or waveguide configurations. Furthermore the TIA used in this case was far from optimal as it was externally packaged commercial product and not optimized for the photodiode. The bandwidth of the TIA (56 Gbit/s) greatly exceeded the device operation speed, which serves to unnecessarily amplify high frequency noise present in the system [3].

Due to the excellent 10 Gbit/s performance, the detector was subsequently measured at higher bit-rates. Figure 4.19 shows a 14 and 20 Gbit/s eye diagram, both taken using the TIA. The 20 Gbit/s eye is significantly degraded, although the 14 Gbit/s eye appears largely open.

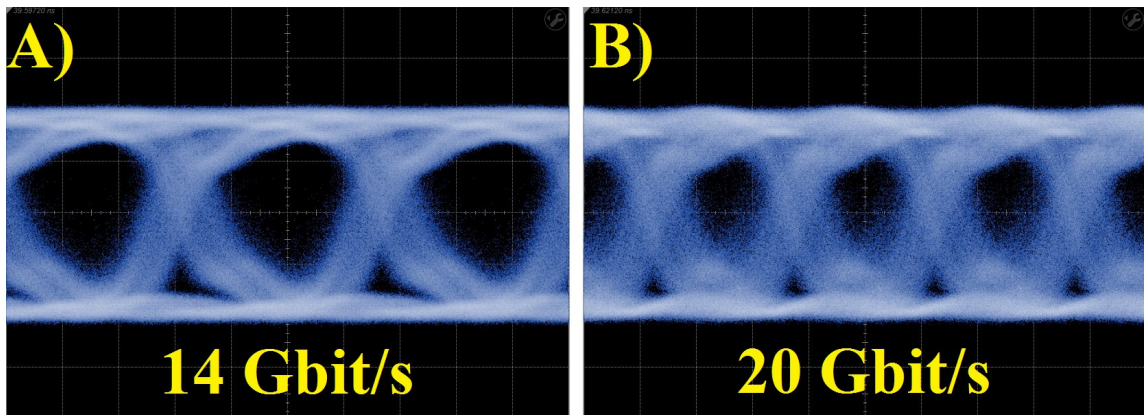


Figure 4.19 | Eye diagrams for a 1 mm long photodiode (IME#1) reverse biased at 35 V. A) 14 Gbit/s B) 20 Gbit/s.

These results lead us into the possible bandwidth limitations of the device. It is clear the performance was increased over the LETI devices described above. This improvement is attributed to a reduced  $RC$  time constant. Capacitance measurements showed an improvement with 1 mm devices showing less than 300 fF, a factor of 4 reduction compared to the LETI devices. Since the detector was of similar design, with regard to the  $p-i-n$  junction and defect concentration, this lowered capacitance is potentially due to

the metal contact design as the metal in the LETI device covered approximately 4 X more surface area.

With this lowered capacitance much faster device operation might have been expected. Multiple samples with varying implantation dose, and resulting defect concentration, were measured but no discernible operation speed difference was observed. It is likely that the devices were limited by the *RC* time constant, but is this due to an increased resistance rather than capacitance?

A fabrication issue with the metal contacting the silicon within the may have led to higher than expected resistance. The oxide etch which established the metal vias was too deep and extended through the thin silicon slab. A correctly performed etch would stop at the silicon layer, allowing the deposited metal to contact a wide area of silicon. In this case, the wide contact area was etched through, leaving the edge of the silicon slab the only contact area. Thus the total contact area of the metal via with the silicon was much lower than anticipated, potentially increasing this contact resistance to values which would limit the device operation speed. Typical metal-silicon contact resistance values from the foundry cannot be disclosed but with this low contact area such contact resistance could be significant relative to the load resistance of 50  $\Omega$ . Figure 4.20 shows SEM images of device cross-sections taken with a focused ion beam (FIB) tool, the metal layer can be seen to extend below the silicon slab layer.

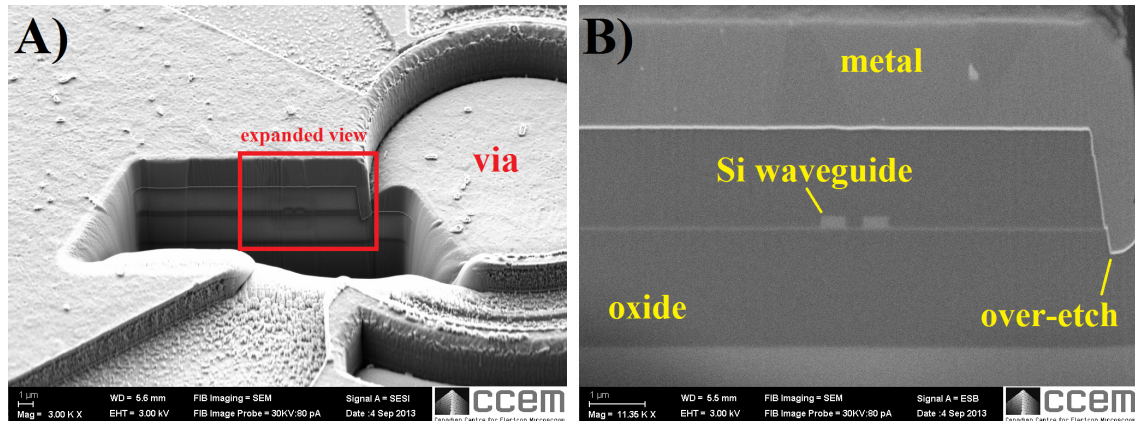


**Figure 4.20 | Scanning electron microscope images off cross sections cut with a FIB. A) an overview of the device, showing the trench cut across the directional coupler of the ring resonator. B) A magnified view of the directional coupler region (light propagation perpendicular to the cross-section). Visible to the right is the overetch of the silicon via, where the deposited metal is seen to extend below the silicon slab region.**

A second uncertainty in regards to resistance is the silicon slab thickness. While the designed thickness was 50 nm in each case, process variability introducing a deeper etch could increase resistance. The slab is visible in the cross sections of Figure 4.20, and a close-up image in Figure 4.21. The thickness appears to be less than 50 nm but this alone is not a reliable indicator due to the low image quality at the silicon interface with the oxide. The oxide is a non-conducting material, allowing charge to build up and create distortions in the image. The sample surface was coated with a conducting material which allows for high quality imaging of the oxide clad surface, but the cross section area was not. Furthermore secondary electron imaging was used, and at the edge of a material emission rates are increased, leading to a distorted image [4, 5]. These effects contribute to the lack of definition of the interface between the silicon and silicon dioxide.

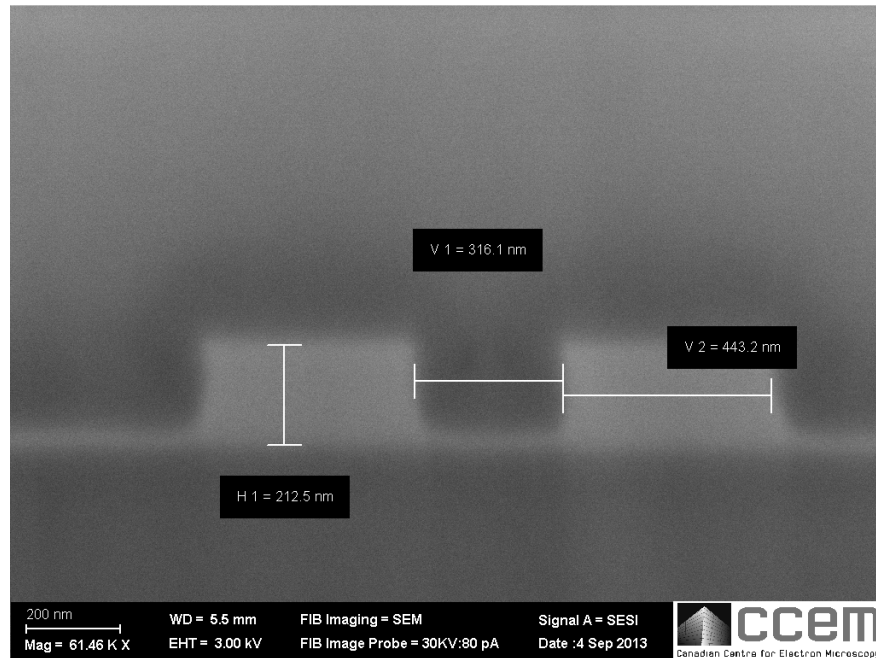


**Figure 4.21 | An SEM image of a waveguide directional coupler from a ring resonator (IME#1).**

If these potential sources of increased resistance were large then it would be expected to be observed in the forward bias current of the photodiode yet comparisons of the IME #1 device show little difference from other samples. This raises two possibilities which are not accounted for. First, the over-etch shown in Figure 4.20 may not have been uniform across the wafer and secondly, inconsistency in the high-speed characterization setup. The experimental setup was not identical for each device run, and devices from each run were not directly compared simultaneously. These concerns are less relevant considering the results presented later in this thesis.

### 4.3 Summary

This chapter presented experimental results for two sets of avalanche photodiode devices; fabricated at LETI (Grenoble, France) and IME A\*STAR (Singapore). These devices make use of an SOI waveguide using a horizontal *p-i-n* detector geometry and ion implantation to introduce lattice defects which enhance absorption.

Both detectors demonstrated similar continuous-wave results, with responsivity of up to 5 A/W, and sensitivity to temperature. The photoresponse followed previously observed trends of defect concentration [6] where temperature exposure above 300 °C permanently reduces detector effectiveness. Measurements of the devices operating up to 70 °C demonstrated that the photocurrent is enhanced with increased temperature, which is important for communications applications.

The photodiodes were characterized at high speed, with error-free operation at 10 Gbit/s achieved for the IME devices. Bit-error rate measurements were not carried out for the LETI devices, but from eye diagram measurements it is clear the IME #1 devices showed higher performance. Comparisons of the high-speed results indicate that the bandwidth limitations are not related to the lattice defects, carrier transit time or avalanche multiplication. Both devices are limited by their  $RC$  time constant, with the LETI devices showing a relatively high capacitance and the IME #1 devices potentially suffering from a high resistance due to a fabrication error.

Regardless of the difficulties, the benchmark of 10 Gbit/s is impressive for a silicon photodiode and the  $RC$  limitations indicate that better performance is achievable, as seen later in this thesis. The next chapter will present results from a second fabrication run at IME A\*STAR.

## References

1. Fan, H.Y. and Ramdas, A.K. Infrared absorption and photoconductivity in irradiated silicon. *J. Appl. Phys.* **30(8)**, 1127-1134 (1959).
2. Smith, B.P. and Kschischang, F.R. Future prospects for FEC in fiber-optic communications. *IEEE J. Sel. Topics. Quantum Electron.* **16(5)**, 1245-1257 (2010).
3. Voinigescu, S. High-frequency integrated circuits. *Cambridge University Press* (2013).

4. Kim, K.H. *et al.* Charging effects on SEM/SIM contrast of metal/insulator system in various metallic coating conditions. *Mater. Trans.* **51(6)**, 1080-1083 (2010).
5. Nishi, Y. and Doering, R. Handbook of semiconductor manufacturing technology, second edition. *CRC Press* (2008).
6. Foster, P.J. *et al.* Optical attenuation in defect-engineered silicon rib waveguides. *J. Appl. Phys.* **99(7)**, 073101 (2006).

# Chapter 5 Photodetection with Si/SiO<sub>2</sub>

## Surface States

### Overview

Following the successful testing of the IME #1 devices there was an opportunity for a second fabrication run at IME A\*STAR. This IME #2 layout was to have a focus on non-resonant detectors, of which two variations will be presented in this chapter:

1) A photodetector which does not use an ion implantation step to create lattice defects, but operates via optical absorption using surface defects along the waveguide edge. At the interface of the silicon and the silicon dioxide cladding, defects necessarily arise due to unsatisfied bonds. These surface-state defects were first demonstrated for photodetection by Baehr-Jones *et al.* [1] with a silicon waveguide contacted with metal through narrow silicon wings. While the work demonstrated the concept it was far from an optimized structure. This thesis reports improvement over that first result with modifications to the device geometry. This involves a *p-i-n* junction implemented on a rib waveguide, and a selective oxide etch over the waveguide region in order to leave the surface unpassivated. This oxide etch step is shown to increase the response of the photodetector, while the *p-i-n* junction enables high-speed operation at low bias;

2) Avalanche photodetectors similar to those described in the previous chapter that employed ion implantation to create lattice defects. These devices allow for a comparison of detectors with and without bulk lattice defects (i.e. detectors where bulk defects are present and those where surface-states alone mediate photodetection). The high-speed operation is not significantly degraded due to the presence of bulk lattice defects.

The results reported in this chapter have formed the basis of the following research journal publication.

Ackert, J.J. *et al.* Monolithic silicon waveguide photodiode utilizing surface-state absorption and operating at 10 Gb/s. *Opt. Express* **22(9)**,10710-10715 (2014).

## 5.1 Fabrication & Measurement

The devices were fabricated at IME A\*STAR using their 248 nm UV lithography platform. The SOI rib waveguides were nominally 500 nm wide and 220 nm in height over a 2  $\mu\text{m}$  thick buried oxide. The remaining silicon slab region was 90 nm thick. Light was coupled to the waveguides with grating couplers defined by a 70 nm deep etch. Ion implantation of boron and phosphorous formed doped regions of a *p-i-n* junction, with a target concentration for each dopant of  $8 \times 10^{19} \text{ cm}^{-3}$ . A top oxide layer was deposited and subsequently contact vias formed, with contact to the silicon made with aluminium. Following the metallization process, a selective oxide etch was carried out above the *p-i-n* region. The oxide was etched in order to expose the silicon surface, leaving it unpassivated. In Figure 5.1, scanning electron microscope images can be seen of the device. Figure 5.1.a shows a top view of the waveguide and etched region, while Figure 5.1.b shows a cross section view of a cut made using a focused ion beam tool.

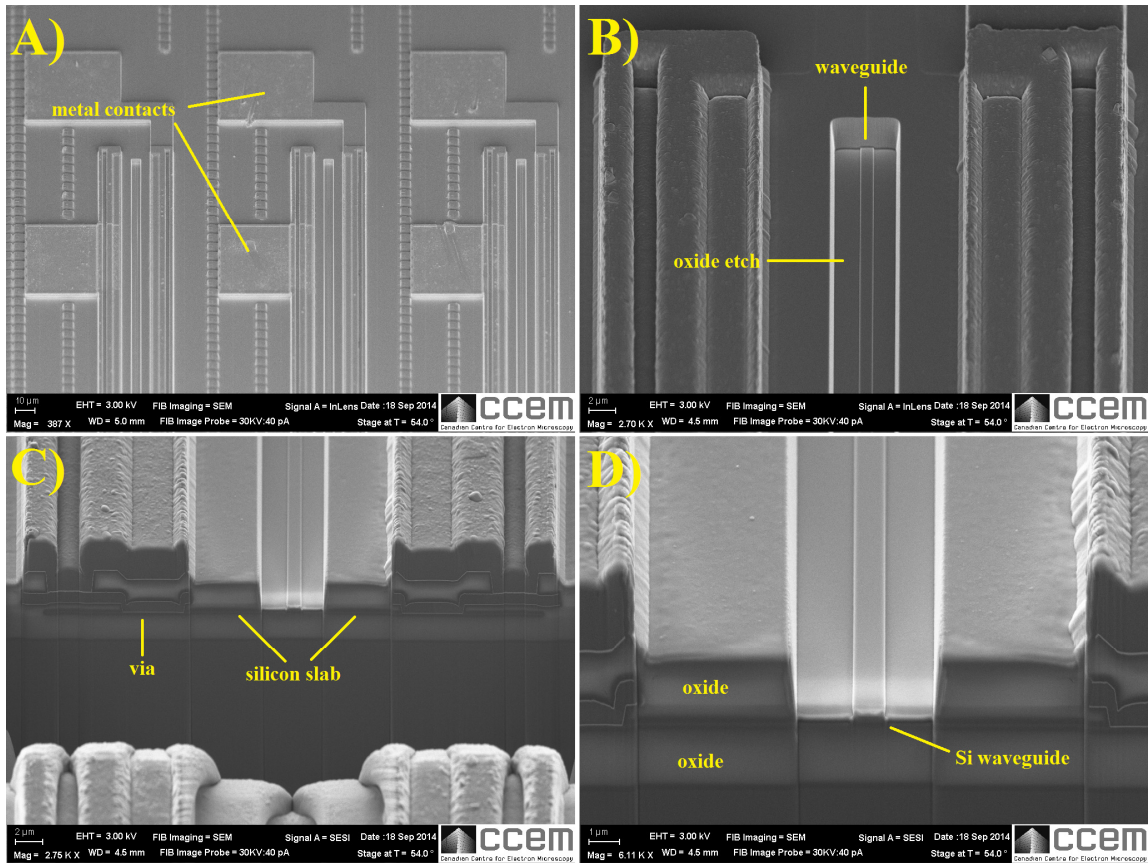


**Figure 5.1 | Scanning electron microscope images of the IME #2 photodetector A) A plan view of the chip with three detectors visible B) Increased magnification from a single detector C) A cross-section of the photodetector D) The cross-section with higher magnification.**

The selective oxide etch was a significant improvement for in the process flow over previous iterations, as the samples no longer required a photoresist mask prior to post-IME ion implantation in the case of the need for bulk defect formation. Furthermore the energies required for implantation can be defined as much lower due to the shallower penetration depth required. This oxide window feature allowed for two distinct types of detector, an avalanche detector operating from bulk defects due to ion implantation, and a surface-state detector which received no implant. Both detectors are formed from the same structure, the surface state detector as fabricated, and the avalanche detector receiving a post-IME ion implantation step in order to introduce lattice defects.



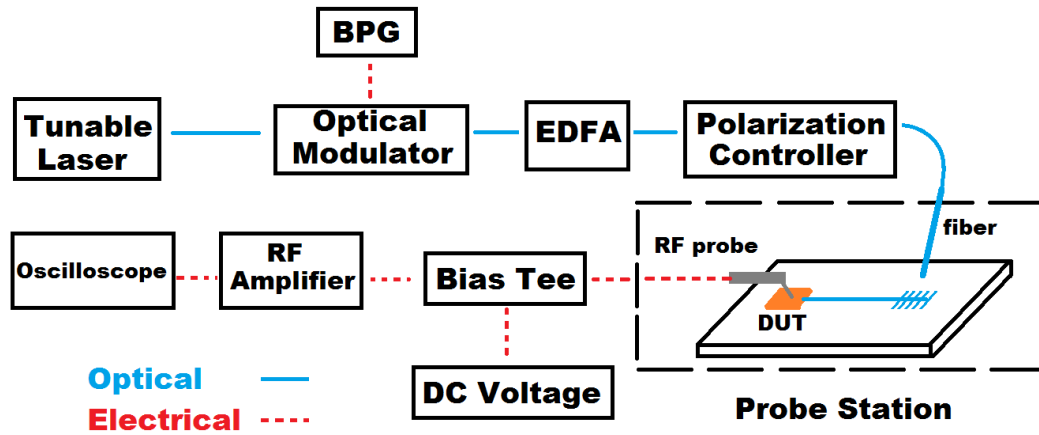


Figure 5.3 | A block diagram of the experimental setup for eye diagram measurements.

## 5.2 Surface-state detectors

### 5.2.1 Continuous-wave results

The detectors relying on surface-state mediation were characterized as fabricated by IME, without undergoing an extra ion implantation step. The oxide opening created during fabrication left an area of exposed silicon, unlike the previous iterations of detectors. This exposed silicon has a thin layer of native oxide after exposure to air, leaving it poorly passivated. This resulted in increased optical absorption versus a detector that did not have the thick cladding oxide removed.

The current-voltage characteristic for a 2 mm long device is shown in Figure 5.7, where the estimated waveguide coupled power is 220  $\mu\text{W}$ . The external responsivity of the detector at 25 V is 0.09 A/W, and at 2 V it is 0.045 A/W. While this responsivity is low compared with bulk defect photodetectors, the internal quantum efficiency is not. The surface-state devices have a loss of just  $6 \pm 1$  dB/cm. For example, with 220  $\mu\text{W}$  of waveguide coupled power a 2 mm long photodiode would absorb 53  $\mu\text{W}$ . This produces 20  $\mu\text{A}$  of photocurrent, and results in an *internal* responsivity of 0.37 A/W at 25 V, equivalent to an internal quantum efficiency of 30 %. The detector also compares

favourably to earlier work on surface-state detectors. Those reported by Baehr-Jones *et al.* [1] showed just 0.036 A/W at 11 V for a 1.5 mm long device. The difference is attributed to a higher level of recombination in the Baehr-Jones device, where the design included thin silicon arms several microns long in which carrier recombination would occur.

The large impact of the oxide removal is demonstrated in Figure 5.4. Control devices that did not receive the oxide removal step were characterized. The control devices were fabricated in the same IME A\*STAR platform and had nominally identical waveguide width and doping separation, however they were 1 mm in length instead of 2 mm. These control devices have a reduction in photocurrent of approximately two orders of magnitude when compared to the device with the oxide removal step. Furthermore, dark current is also lower in the control device, as the surface remains passivated. The differences between these two devices clearly show the beneficial effect of the unpassivated silicon in terms of photodetection. The impact of oxide removal results from the initially unsatisfied bonds at the silicon surface reacting with ambient oxygen and forming a low quality, native oxide.

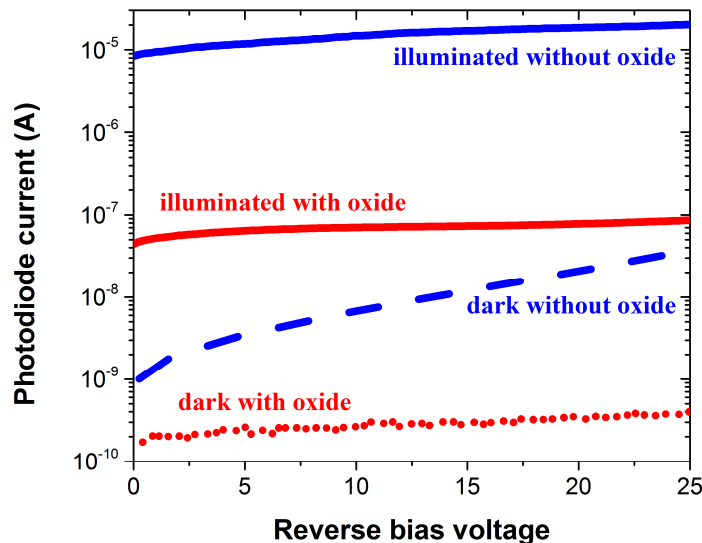


**Figure 5.4 | Photodiode current versus reverse bias voltage for a 2 mm surface-state photodetector and a 1 mm long control device lacking the oxide opening step. The unpassivated surface due to the oxide opening enhances the response of the surface-state device.**

### 5.2.2 Optical power linearity

Linear operation (i.e. a linear response in photocurrent as a function of optical power) is desired for photodetectors in general. In the case of the monolithic detectors described here, verification of linear behaviour also rules out two-photon absorption (a non-linear phenomenon) [2] as the dominant absorption mechanism. The optical power linearity was investigated using an erbium-doped fiber amplifier, set to a fixed gain, and a variable fiber optic attenuator. Figure 5.5 plots the photocurrent response for varying levels of optical power coupled into the chip, with linear response observed over the measured range. Linear operation is observed in agreement with the result of Baehr-Jones *et al.* [1]. It indicates that two-photon absorption is not significant and therefore surface states are the dominant cause of the optical absorption.

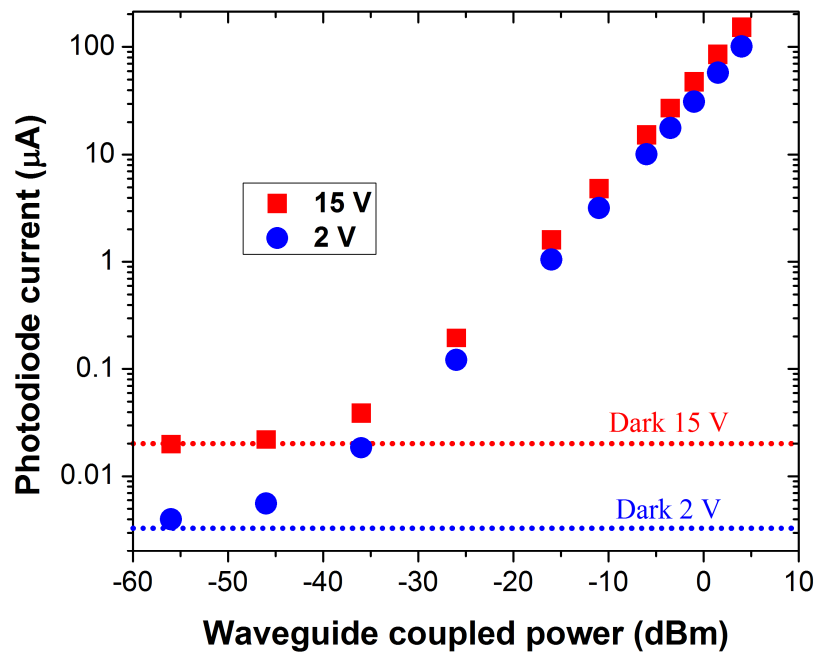
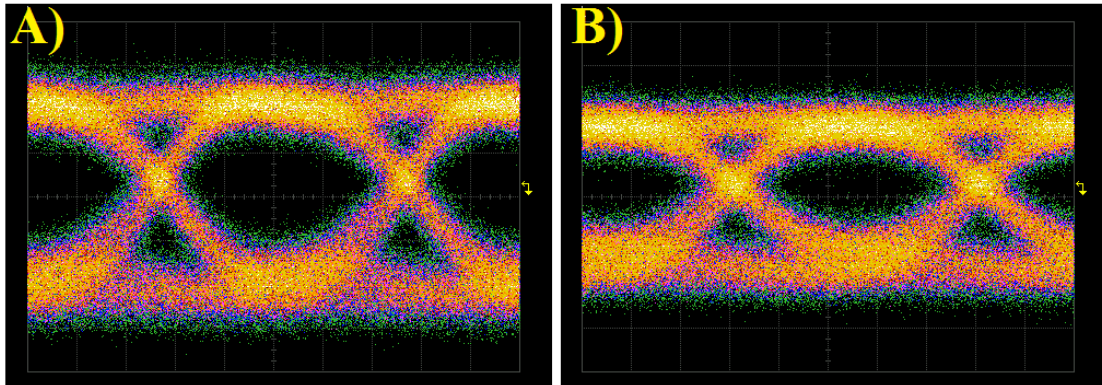


Figure 5.5 | Photodiode current versus waveguide coupled optical power for a 2 mm long photodiode. The current is shown for a reverse bias of 15 V and 2 V, a linear response is seen across the measured range if dark current is subtracted.

### 5.2.3 High-speed results

The high-speed response of the surface-state detectors was observed using a  $2^{31}$ -1 PRBS on-off keying signal. An oscilloscope was used to record eye diagrams at 10 Gbit/s which are shown in Figure 5.6. In Figure 5.6.a, a 2 mm long detector is shown operating at a reverse bias of 10 V, while in Figure 5.6.b the same device is shown operating at a reverse bias of 2 V. The rise and fall time is approximately 60 ps, and there is no significant change in this value upon increasing the reverse bias voltage.



**Figure 5.6 | 10 Gbit/s eye diagrams of a 2 mm long surface-state photodiode. A) 10 V reverse bias B) 2 V reverse bias.**

The high-speed operation achieved here exceeds that of the Baehr-Jones device, which showed a small-signal bandwidth of 1.7 GHz. The Baehr-Jones device used silicon wire waveguides and metal to silicon contacts without the use of doping. Consequently the metal contacts were placed several microns away from the waveguide to avoid optical absorption, leaving carriers to travel several microns through thin undoped silicon arms before extraction. In contrast, the device reported here uses a rib waveguide and *p-i-n* junction, reducing the carrier travel distance to 1  $\mu\text{m}$  (the waveguide width plus the doping separation). This structure allows for fast operation with a reverse bias of just 2 V. Operating without the need for an external high voltage source, or step-up voltage converter would simplify the power design of a photonic chip, or enable integration into a low voltage CMOS environment.

## 5.3 Bulk defects versus surface-state defects

### 5.3.1 Comparison of continuous-wave results

We now discuss the merits of the surface-state detector versus a detector utilizing bulk defects introduced using ion implantation. Most importantly, these two detectors operate optimally in different bias regimes. The bulk defect detectors show a strong avalanche effect at high bias, but a small photocurrent at low bias. Comparatively, the surface-state detectors show a significantly better response at low bias, but lack high responsivity in the avalanche regime.

In Figure 5.7 the current-voltage characteristics of a surface-state (no bulk defects) and avalanche detector (with bulk defects) are compared. The figure provides insight into the effect of the bulk defects on the detector. At low bias, significant recombination at defect centres reduces the photocurrent, while in the surface-state device carriers can be extracted with relatively high efficiency as only the surface acts as a source of recombination. At high bias there is a significant increase in photocurrent for the bulk defect device, but this effect is not observed in the surface-state device. Upon breakdown (not shown in Figure 5.7), the surface-state detector photocurrent trends with the dark current and significantly increased responsivity is not observed, while the bulk defect devices show avalanche gain well before breakdown, indicating perhaps (and importantly) that the defects play a role in the avalanche process itself.

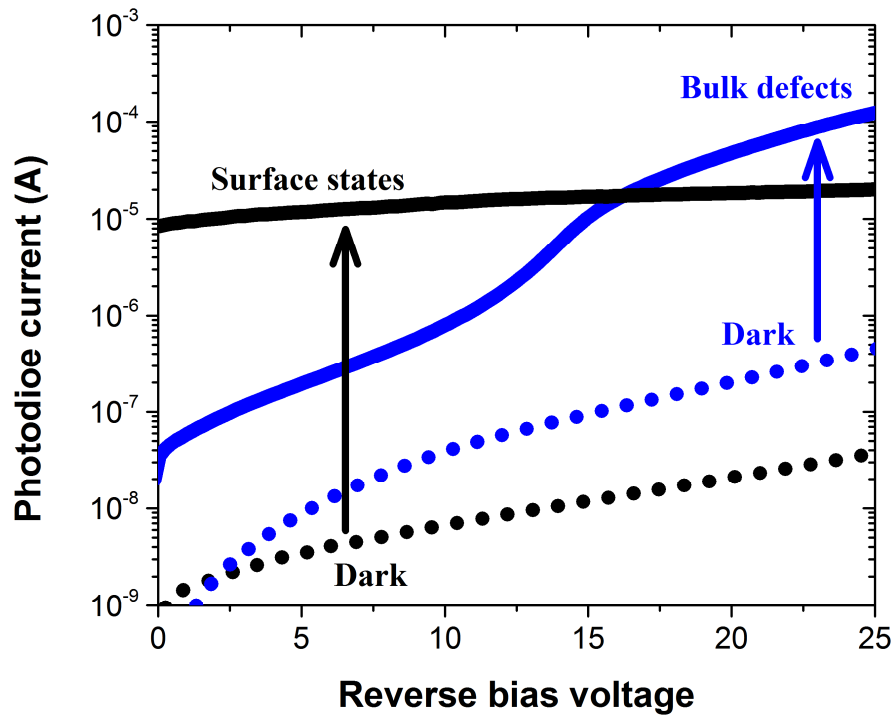
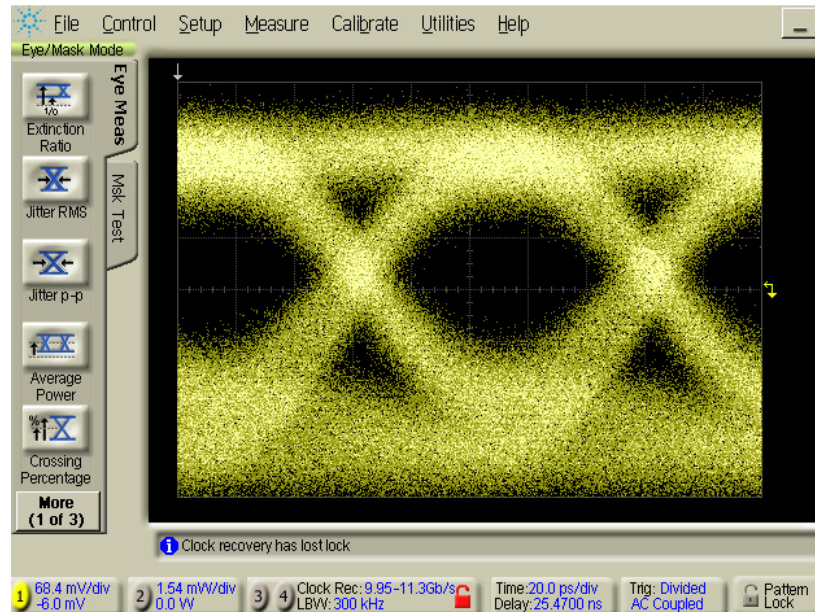


Figure 5.7 | A comparison of the surface-state detector with a bulk defect detector. The bulk defect device is 1 mm long, while the surface-state device is 2 mm.

It should be noted that this plot provides the general trend of behaviour for the two detectors; the particular here devices come from different chips and utilize different design dimensions. A direct comparisons of responsivity should not be inferred from this figure.

### 5.3.2 Comparison of high-speed operation

An eye diagram for an ion implanted detector is shown in Figure 5.8 for a 1 mm long 1000-100 detector operating at 10 Gbit/s. The operation speed of these photodetectors does not surpass that of the previous IME #1 devices. Considering the  $RC$  time constant limitation, these detectors should have possessed lower resistance, due to a thicker slab region. Capacitance measurements showed 230 fF for a 1 mm long device, slightly higher than the previous fabrication run but still a relatively low value. The devices also possessed a shorter  $p-n$  separation, which would reduce any carrier transit time limitations compared to the previous devices.



**Figure 5.8 | A 10 Gbit/s eye diagram for a 1 mm long ion implanted photodiode (1000-100) at 15 V reverse bias (IME #2).**

The high-speed operation of the ion implanted and surface-state detector are compared using eye diagrams shown in Figure 5.9. The response time of the detectors is not greatly different, however the implanted detector does show pattern dependencies. Both of the eye diagrams are for 2 mm long detectors, as the shorter length surface-state diode did not produce great enough photocurrent to enable measurement.

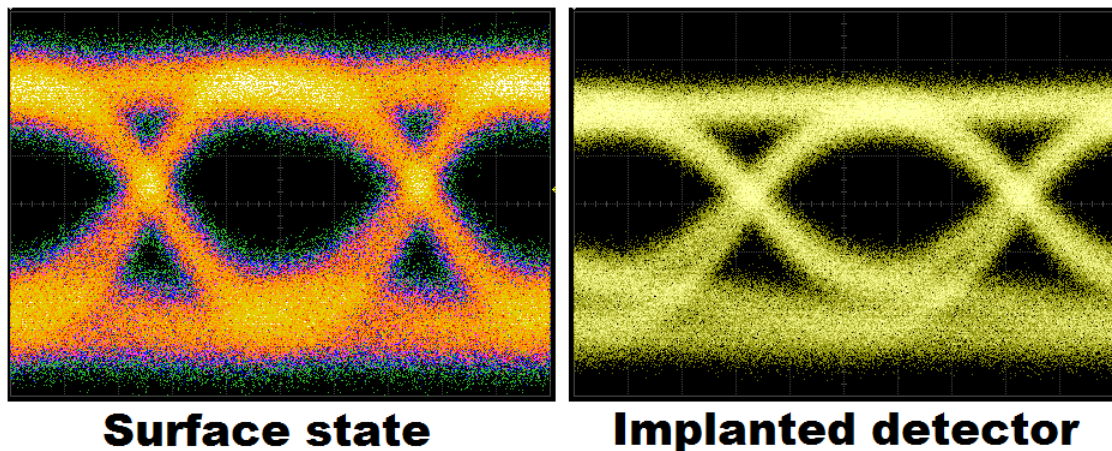


**Figure 5.9 | Eye diagrams of a surface-state detector (-20V bias) and an ion implanted detector (-26 V bias). Both are 2 mm long detectors operating at 10 Gbit/s (20 ps/division time scale). The surface-state detector was a 500-300 design while the implanted detector was 500-400.**

From the eye diagrams we can see that the surface-state detector is not significantly faster than the bulk defect devices, despite the presence of bulk defects and their potential effects on the carrier lifetime and mobility.

## 5.4 Summary

This chapter presented results for surface-state detectors and avalanche detectors fabricated at IME A\*STAR (IME #2 run).

A surface-state detector at a wavelength of 1530 nm has been demonstrated. The detector showed an open eye diagram at 10 Gbit/s with a 2 V reverse bias with a responsivity of 0.045 A/W. Optical absorption is due to surface-state defects which show an internal quantum efficiency of 30%. No ion implantation step is necessary to create surface defects. Instead, an oxide opening etch step was utilized to expose the silicon to air which allowed for the growth of native oxide and an increased concentration of surface defects. The monolithic silicon structure and ease of fabrication makes this device very adaptable for a variety of fabrication process flows. The primary application of this device will likely be waveguide power monitoring.

The avalanche detectors incorporated bulk defects. Operation speed was not enhanced over the previous generation of devices, despite the use of a thicker silicon slab to reduce resistance and a low measured capacitance. However, comparisons of the high-speed operation of the bulk defect and surface-state detectors showed that the presence of defects did not significantly impact high-speed operation.

These detectors are primarily attractive for the ease of fabrication, and consequently their implementation into a variety of complex circuits. While surface-state detectors offer much less responsivity than the ion implanted avalanche detectors, their low optical absorption and high internal quantum efficiency (30%) suggests the primary application is power monitoring. This geometry can easily be integrated onto a waveguide providing a large advantage over hybrid approaches.

It is likely that many improvements can be found to the surface-state detector. As previously described, the sensitivity of these detectors depends on the optical mode/surface overlap, and waveguide geometry could be changed to maximize this. This includes simple dimension changes, but also could involve the use of slot waveguides [3]. Another area not explored in this thesis is the effects of alternative surface treatments. These devices underwent an oxide etch to the silicon surface, followed by exposure to air and the growth of the native oxide. There is no reason to believe that this process resulted in the optimal concentration of surface defects. Alternative passivation treatments would likely produce different responsivities.

## References

1. Baehr-Jones, T., Hochberg, M. and Scherer, A. Photodetection in silicon beyond the band edge with surface states. *Opt. Express* **16**, 1659-1668 (2008).
2. Chen, H. and Poon, A.W. Two-photon absorption photocurrent in p-i-n embedded silicon microdisk resonators. *Appl. Phys. Lett.* **96**, 191106 (2010).
3. Dell'Olio, F. and Passaro, V.M. Optical sensing by optimized silicon slot waveguides. *Opt. Express* **15**, 4977-4993 (2007).

# Chapter 6 Long Wavelength Detection

## Overview

This chapter presents measurements of the response of defect mediated avalanche detectors to long wavelengths. Thus far this thesis has contained measurements in established telecommunication windows around 1550 nm (the so called *C* and *L* bands). This chapter includes continuous-wave measurements using wavelengths from 1.96 to 2.5  $\mu\text{m}$ . High-speed operation of the detectors is demonstrated at 1.96  $\mu\text{m}$ , with an open eye diagram at 20 Gbit/s representing the highest demonstrated bit-rate in this thesis. The results are followed with a comparison to the previous lower speed detectors in this thesis.

The photodetectors were fabricated as part of a third multi-project wafer facilitated by CMC Microsystems at IME A\*STAR in Singapore, and will be referred to as IME #3. Devices from the LETI, IME #1 and IME #2 runs were not characterized at longer wavelengths due to lack of compatibility of the coupling structures.

A journal article describing these photodetectors has been accepted for publication in Nature Photonics.

## 6.1 Integrated optics at extended wavelengths

Optical communications has evolved to use wavelengths around the 1.55  $\mu\text{m}$  region due to the availability of low-loss optical fibers and the high utility of the erbium-doped fiber amplifier. These innovations have spurred the development of a family of devices which operate in this wavelength range. This operating window is largely shared by efforts in silicon photonics, as most integrated devices must interface with external optical equipment or fiber.

In the coming decades the data capacity offered by current telecommunications technology will not be sufficient to meet demand [1]. High growth in internet data use

continues to occur, largely due to the delivery of video over the internet. Large research efforts are being focused on technologies which promise increased bandwidth through the use of new spectral regions near 2  $\mu\text{m}$  and the use of hollow-core photonic band-gap fiber [2]. These fibers are predicted to offer low optical loss in this wavelength region, but most importantly they will offer low non-linearity due to the mostly air core. A second key technology is the recently developed thulium-doped fiber amplifier, which has a gain window from 1.8 to 2.05  $\mu\text{m}$  [3]. This is a broader wavelength range than that achievable with erbium doped fibers and therefore many more channels can occupy the same fiber in a wavelength-division multiplexing scheme.

With the increasing appeal of the silicon photonics platform for telecommunications the long wavelength regions will become increasingly important for integrated optics. Furthermore, there is a myriad of other applications which will demand integrated long wavelength components [4].

There is a limited availability of photodetectors for this wavelength range which are compatible with silicon photonics. Hybrid approaches have been demonstrated using III-V devices [5], but this solution is limited by the necessity for wafer bonding, making waveguide-integrated devices difficult. Germanium on silicon is a common hybrid material system used for detection at 1550 nm but has low absorption at longer wavelengths. Alloys of germanium-tin have high potential beyond 1550 nm and have received much attention in recent years, but there has been limited results thus far [6,7]. Graphene is an upcoming optoelectronic material and detection has been demonstrated at long wavelengths on silicon waveguides [8] and chemical vapor deposition of graphene on silicon could allow for processing at the wafer scale [9]. However the performance of demonstrated devices and the sophistication of fabrication techniques at this time leave much development work to be done.

Defect-based detectors have been reported in silicon beyond the telecommunications windows. Grote *et al.* demonstrated 1 Gbit/s operation at a wavelength of 1.9  $\mu\text{m}$  [10], and recently Souhan *et al.* achieved devices with a bandwidth of 1.7 GHz at 2.2  $\mu\text{m}$  [11].

Both of these works relied on the introduction of lattice defects. Detectors that rely on deep levels introduced by dopant atoms such as gold have been reported [12], however gold is a highly detrimental contaminant in CMOS processing so their device utility for silicon photonics is questionable.

## 6.2 Fabrication

The detectors were fabricated at IME A\*STAR in Singapore and will be referred to in the text as IME #3. The primary goal for this fabrication run was to produce edge-coupled devices that could be characterized at wavelengths up to 2.5  $\mu\text{m}$ . The photodiodes comprised of *p-i-n* junctions on SOI waveguides formed with a 90 nm etch. The SOI wafer consisted of a top layer of silicon 220 nm in height, and a 2  $\mu\text{m}$  thick buried oxide layer. The waveguides were 1  $\mu\text{m}$  in width and boron and phosphorous dopants were implanted 300 nm from the waveguide sidewall to minimize optical propagation loss. The contacts were formed with a 2  $\mu\text{m}$  thick deposition of aluminum, and were positioned several microns away from the waveguide. A schematic cross section of the device is shown in Figure 6.1. An oxide etch was done to open an implantation window over the intrinsic region of the detector. A boron ion implantation at an energy of 60 keV and a dose of  $1 \times 10^{13} \text{ cm}^{-2}$  introduced lattice defects. In Figure 6.2 SEM images are shown, including a cross-section cut obtained with a focused ion beam tool. Further fabrication details will be discussed at the end of this chapter, with a comparison to previous devices.

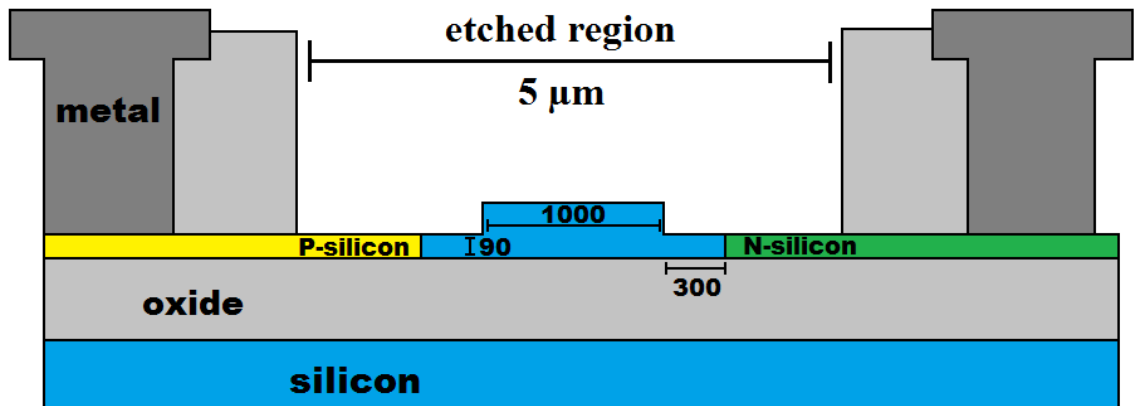
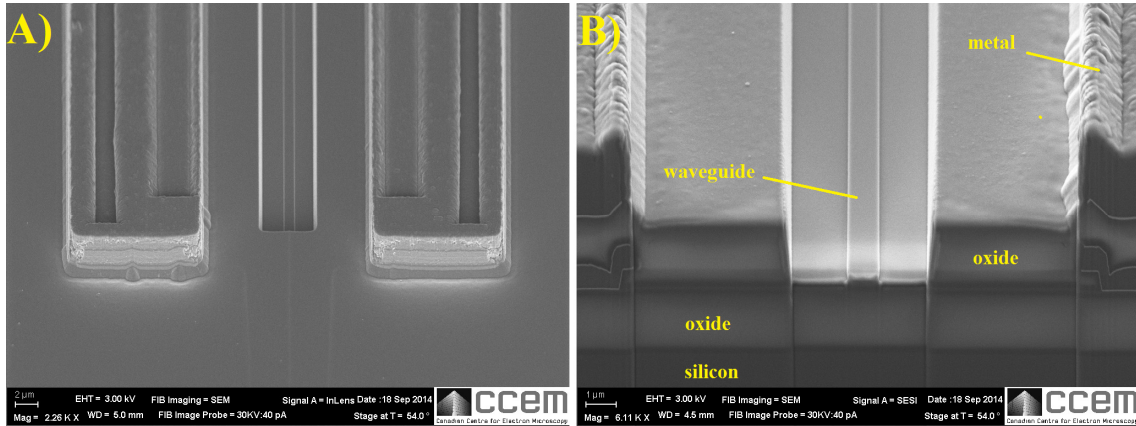


Figure 6.1 | A schematic cross-section of the IME #3 photodiode. Waveguide dimensions are labeled in nanometers (not to scale).

Light was coupled to the photodiodes with inverted-taper waveguides [13]. Compared to grating couplers, the inverted tapers have broadband coupling and offer much greater experimental opportunity. The fabrication of grating couplers introduces uncertainty in the peak transmission wavelength, primarily due to the etch depth. Further, grating couplers require the repetition of device structures for tests at different wavelengths. However, grating couplers can be a useful choice for their ease of alignment and freedom of positioning. The use of edge couplers restricts chip layouts as every waveguide requires access to the edge of the sample.

The edge couplers used in this case had a width which was linearly reduced from the detector waveguide width of 1000 nm, to 180 nm over a distance of 200  $\mu\text{m}$ . The silicon waveguide height and oxide cladding remain unchanged over the length of the taper. To facilitate coupling to this structure, a deep etch was carried out at the edge of the chip. This allowed the edge to be located within a few microns of the tapered waveguide, ensuring that the external fiber could be positioned closely after sample dicing. The coupler on this chip achieved a loss of approximately 4 dB at a wavelength of 2.02  $\mu\text{m}$ . This compares favourably with previously reported grating coupled results in this thesis.



**Figure 6.2 | SEM images of a photodiode from the IME #3 fabrication run. A) An overhead view of the photodiode B) A cross-section of the photodiode taken with a focused ion beam tool.**

## 6.3 Results

### 6.3.1 Continuous-wave measurements

The photodiodes were characterized using a fiber-coupled 2.02  $\mu\text{m}$  laser diode. A pair of Thorlabs PM2000 fibers, modified to have a lensed tip with a 4  $\mu\text{m}$  spot size, were used to couple light in and out of the waveguides. The fibers were mounted on piezoelectric XYZ stages and an InGaAs detector (Thorlabs PDA10D) measured the optical power from the output fiber. The current-voltage (IV) characteristic is shown in Figure 6.3, where an external responsivity of  $0.3 \pm 0.02$  A/W is achieved at a reverse bias of 30 V, with a dark current of less than 1  $\mu\text{A}$ .

This responsivity is calculated using the coupling loss measurement of 4 dB, and a launch power of 1 mW. The coupling loss was found by measuring the average throughput waveguide loss, a measurement which included an input coupler, output coupler and a 2.5 mm long waveguide. The couplers are assumed to have equal loss but the waveguide loss is a source of uncertainty. In this responsivity calculation, a loss of 3 dB/cm is assumed. Waveguide loss structures were not included on this sample due to area constraints. However, waveguides from similar chip layouts measured at 1550 nm typically show a propagation loss of 2-3 dB/cm. At longer wavelengths SOI waveguide

loss remains low, rib waveguides have been demonstrated with an optical loss of 0.7 dB/cm at a wavelength of 3.39  $\mu\text{m}$  [14]. Sidewall scattering as a source of loss decreases as the wavelength is increased, as small wavelengths more easily scatter off small discontinuities. With the assumption of similar loss to waveguides at 1550 nm and the relatively short waveguide length, the resulting uncertainty in responsivity is relatively small.

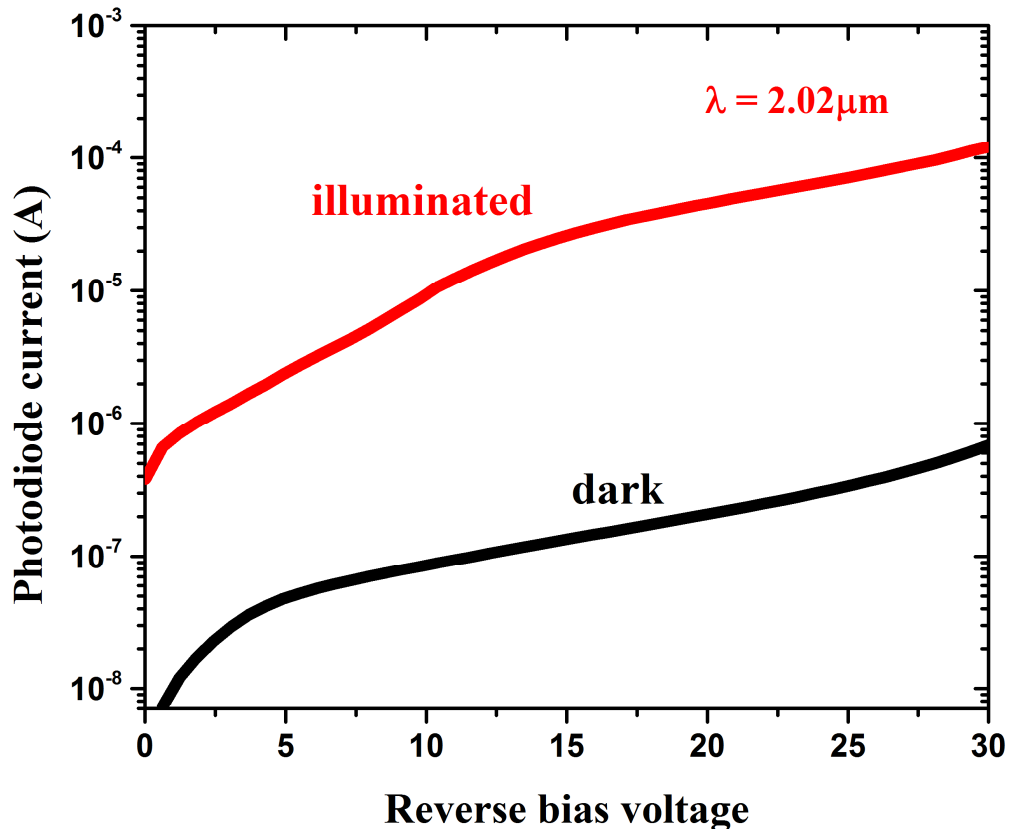


Figure 6.3 | Current versus reverse bias voltage for a 1 mm long photodiode (IME #3) at a wavelength of 2.02  $\mu\text{m}$ .

The photodiode response with wavelength was measured using a tunable  $\text{Cr}^{2+}:\text{ZnSe}$  laser with a free-space output, which was coupled to a fiber with an objective lens. The output of the laser was adjusted such that 10 mW was measured prior to the device under test, correcting for wavelength dependent loss of the fiber and objective lens. The photodiode current was measured for various wavelengths and is shown in Figure 6.4. There is a drop in the response from 1.96 to 2.5  $\mu\text{m}$  of 14 dB, which is more significant

than seen in previous work [15], which showed a 9 dB reduction from 2 to 2.5  $\mu\text{m}$ . In the work of Thomson *et al.* the waveguide cross section was over 10  $\mu\text{m}^2$  while the device presented here is merely 0.22  $\mu\text{m}^2$ .

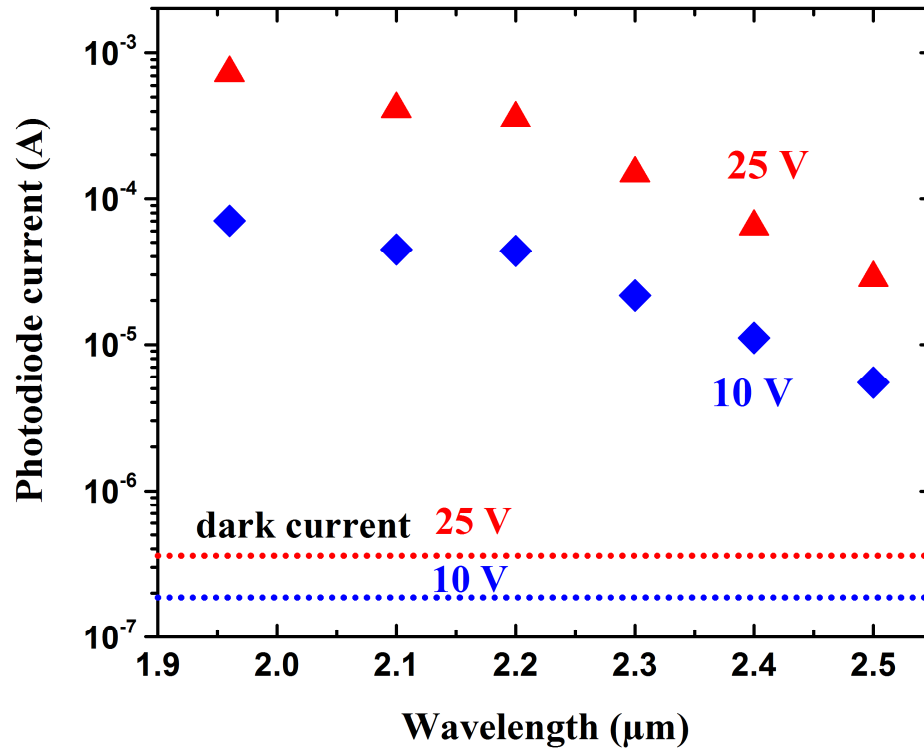


Figure 6.4 | Current versus wavelength for a 1 mm long photodiode (IME #3) with a reverse bias of 10 and 25 V.

With longer wavelengths the propagating optical mode is expected to suffer higher loss from two sources. First, the mode will extend further outside the waveguide and into the highly absorbing doped regions. Secondly the thickness of the buried oxide will no longer be sufficient and leakage into the bulk silicon will occur. Individual test waveguides with no detector structure and a width of 750 nm showed severe reduction in efficiency with longer wavelength. The transmission of such a waveguide versus wavelength is shown in Figure 6.5. The optical power transmitted degrades sharply beyond 2.3  $\mu\text{m}$ , in a similar manner to that shown in Figure 6.4. There was no test waveguide with a width of 1000 nm, but it is surmised that a significant portion of the

difference between this work and that of Thomson [15] is due to the small cross section waveguides which are not suitable for 2.5  $\mu\text{m}$  operation.

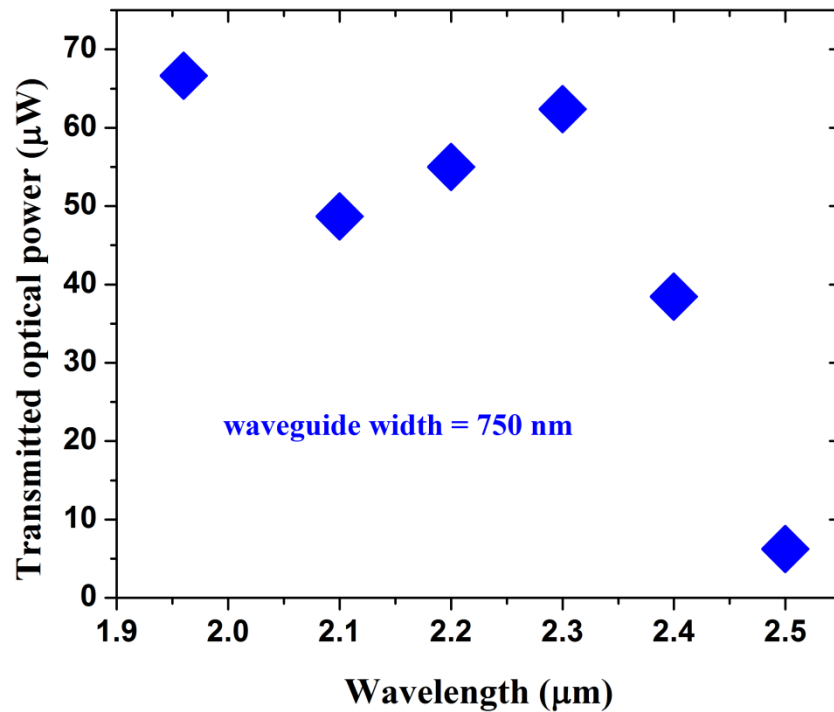


Figure 6.5 | Optical transmission of a 750 nm waveguide versus wavelengths.

The power linearity was also measured and is shown in Figure 6.6 for a wavelength of 2.2  $\mu\text{m}$  for two different reverse bias voltages. The photocurrent varies as a fractional exponent of the input optical power, suggesting saturation of lattice defects or space-charge effects. More importantly this shows that two-photon absorption is not the dominant mechanism, as this would be revealed as an increase in efficiency with increased power.

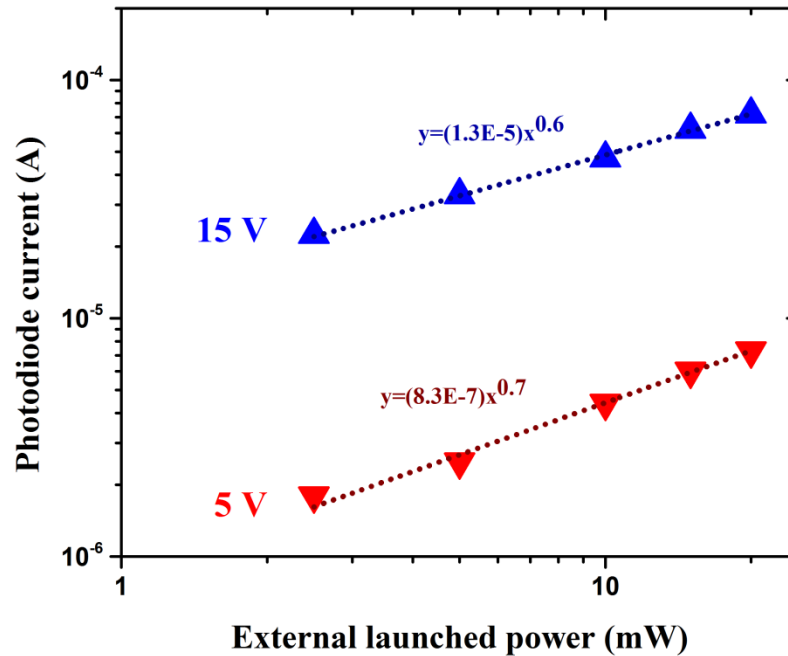


Figure 6.6 | Photodiode current versus optical power at a wavelength of 2.2  $\mu\text{m}$  for a 1 mm long IME #3 photodiode. Photocurrent is shown for 5 and 15 V reverse bias.

### 6.3.2 High-speed measurements

High-speed characterization was carried out with a 1.96  $\mu\text{m}$  laser diode as it possessed a much lower noise level than the tunable  $\text{Cr}^{2+}:\text{ZnSe}$  laser. Optical launch power exiting the fiber was 10 mW, a power level made possible by the presence of a TDFA [3]. A 10 GHz  $\text{LiNbO}_3$  modulator (Photline model MX-2000-LN-10) was driven by a 40 Gbit/s pseudo-random bit sequence generator (Centellax TG1P4A) and RF amplifier rated for 40 Gbit/s operation (Centellax OA4MVM3). The output was passed through a polarization controller before the tapered fiber which was coupled to the test waveguide. A 40 GHz rated probe interfaced with the photodetector under test, and a 50 GHz bias tee (picoseconds pulse labs 5543) was used to apply a bias with a Keithley 2400 Sourcemeter. The AC output of the bias tee was connected to a digital communications analyzer (DCA) with an 80 GHz bandwidth (Agilent 86116C Opt. 040). Eye patterns were recorded with a non-return to zero, on-off keying signal with a pattern length of  $2^7-1$ . A block diagram of the experimental setup is shown in Figure 6.7.

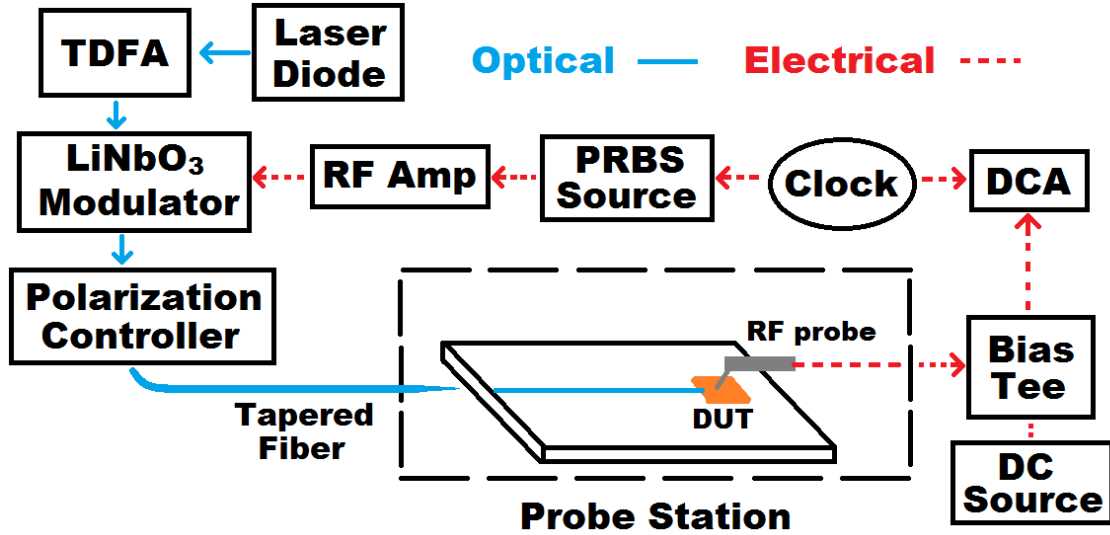


Figure 6.7 | A block diagram of the experimental setup for high-speed characterization at a wavelength of 1.96  $\mu\text{m}$ .

Eye diagrams are shown in Figure 6.8 for a 1 mm long photodiode. An open eye at 28 Gbit/s was observed, which is a large improvement over previous devices in this thesis.

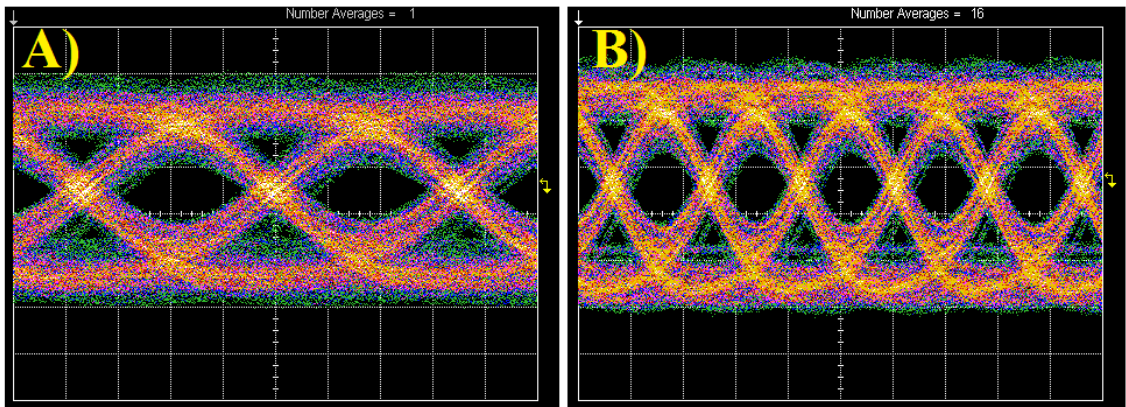
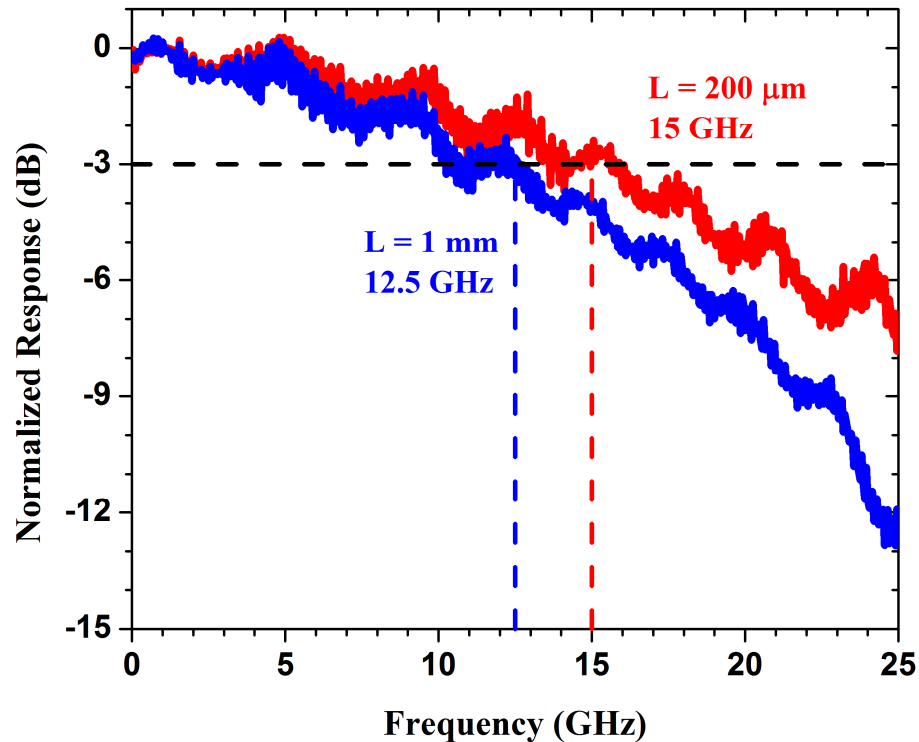


Figure 6.8 | Eye diagrams of a 1 mm long IME #3 photodiode operating at a wavelength of 1.96  $\mu\text{m}$  with a bit-rate of 28 Gbit/s at a reverse bias of 27 V. A) Timescale 10 ps/div B) Timescale 20 ps/div.

Interpreting the speed limitation from these eye diagrams is difficult because the LiNbO<sub>3</sub> modulator was rated for 10 GHz, so 28 Gbit/s is likely in the bandwidth limited regime. The experiment lacked a suitable reference photodiode to record the system

response. Therefore the detector bandwidth was characterized at 1550 nm, where higher speed test equipment is available. The normalized small signal response for a 1 mm and 200  $\mu\text{m}$  long photodiode at a wavelength of 1550 nm are plotted in Figure 6.9. The 1 mm device shows a small signal 3 dB bandwidth of 12.5 GHz while the 200  $\mu\text{m}$  device achieves 15 GHz.



**Figure 6.9 | The small signal frequency response of IME #3 photodetectors of lengths 1 mm and 200  $\mu\text{m}$  at a wavelength of 1550 nm.**

The capacitance of the 1 mm photodetector was measured to be  $260 \pm 10$  fF using a Boonton 7200 capacitance meter at a frequency of 1 MHz. If we neglect the resistance of the doped silicon and assume a  $50 \Omega$  load resistance then the  $RC$  limited bandwidth is approximately 12 GHz. This is comparable with the measured result for 1550 nm, and also a likely limitation for the 2  $\mu\text{m}$  wavelength measurements.

It is worthwhile to examine the operation of the device at different levels of bias. In an avalanche detector, a high gain factor limits the operation bandwidth [16]. Alternatively, too low a bias could result in carrier transit time limitations. Figure 6.10 presents eye

diagrams at 20 Gbit/s for reverse bias voltages of 15, 20 and 27. The higher bias voltages increase the signal magnitude without noticeable degradation in operation speed. This confirms that carrier velocity saturation has occurred, as expected based on the results earlier in this thesis. It also shows that these results are not limited by avalanche gain.

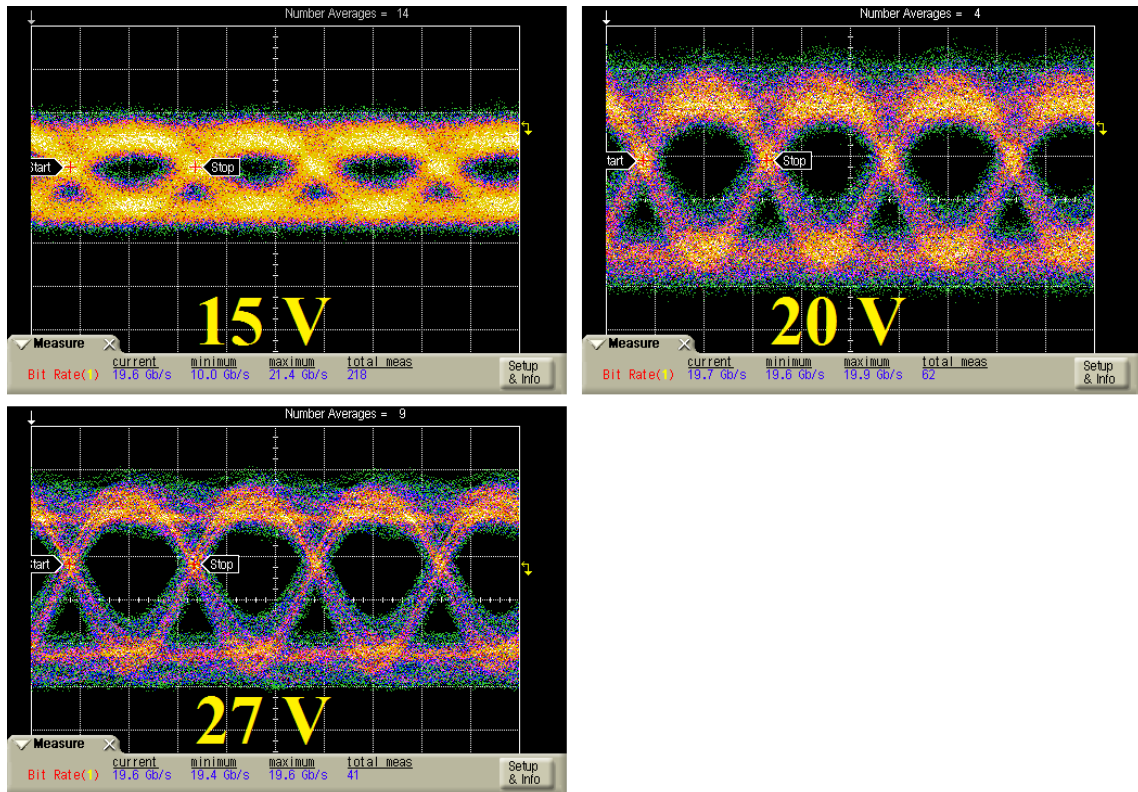


**Figure 6.10 | 20 Gbit/s eye diagrams of a 1 mm long IME #3 photodetector at a wavelength of 1.96  $\mu\text{m}$  with reverse biases of 15, 20 and 27 V. The vertical scales are 2.0, 2.0 and 6.7 mV/division respectively. The horizontal scale is 20 ps/division.**

These results also indicate that the 2  $\mu\text{m}$  wavelength measurements were not greatly limited by the 10 GHz rated modulator and that the  $RC$  time constant is the likely limitation. A 12.5 GHz detector would not likely operate beyond 20 Gbit/s, as was observed in Figure 6.10. The 28 Gbit/s operation shown in Figure 6.8 would not be suitable for data communication as it's in the bandwidth limited regime. Yet significantly, 20 Gbit/s is the fastest eye diagram of any waveguide integrated device operating at this wavelength to date.

## **6.4 Comparison with previous work described in this thesis**

The IME #3 devices represent an impressive increase in operation speed over the previous devices presented in this thesis. This result has established that defect lifetimes were not imposing operational speed limitations on earlier device iterations, albeit the ultimate speed of the detector remains an open question.

The result raises questions as to why earlier efforts were limited to slower speeds. It is useful to compare the fabrication parameters of the devices in detail, which are tabulated in Figure 6.11. The design parameters listed (e.g. metal dimensions) were not verified after fabrication. The fabrication facilities generally produce devices with dimensions within given specification, however fabrication errors are possible as seen with the metal process for the IME #1 device.

	<b>Fabrication run</b>			
	<b>LETI</b>	<b>IME #1</b>	<b>IME #2</b>	<b>IME #3</b>
<b>Error-free bit rate (Gbit/s)</b> *estimated	< 6*	10	10*	20*
<b>Small signal bandwidth (GHz)</b>	2 (800 $\mu\text{m}$ long)	3.25 (1 mm long)	No data	15 (200 $\mu\text{m}$ long) 12.5 (1 mm long)
<b>Capacitance (fF/mm)</b>	1300	300	230	260
<b>Silicon slab height (nm)</b>	50	50	90	90
<b>Implantation window</b>	photoresist	photoresist	Oxide	Oxide
<b>N++ concentration</b>	4E19	4E19	8E19	4E20
<b>P++ concentration</b>	4E19	4E19	8E19	4E20
<b>Contact metal</b>	Al/Cu	Al	Al	Al
<b>Contact metal thickness</b>	0.58	2	2	2 (2 step)
<b>Via (width <math>\mu\text{m}</math>)</b>	3	6	9.8	9
<b>Via distance from waveguide (<math>\mu\text{m}</math>)</b>	4.75	2.75	8.1	7.9
<b>Metal coverage per mm of length (<math>\mu\text{m}^2</math>)</b>	85000	23000	31200	29000

**Figure 6.11 | A comparison of fabrication parameters for detectors in four different multi-project wafer fabrication runs.**

Examining the capacitance values and metal layout, the LETI devices had increased capacitance and significantly different metal design parameters compared to the IME devices. The area covered by metal was significantly higher for the LETI device, which may be contributing to high parasitic capacitance and lower operation speed.

The performance difference between the IME #2 and IME #3 devices is harder to explain. For the IME devices, dimensions for the metal and vias varied primarily due to differing design rules between shuttle runs. For the IME #2 and #3 devices the metal parameters are nearly identical and the difference in measured capacitance is not significant enough on its own to explain the operation speed difference.

The designs shared many characteristics, with the primary difference being the  $p$  and  $n$  dopant concentration. It is possible that the IME #2 devices were being limited by

diffusion current. If absorption in the doped silicon wings was occurring then photocurrent could be generated if excited carriers drift into the depletion region (the waveguide). This diffusion current would have a slow time response. The IME #3 devices received a significantly higher doping concentration, meaning that excited minority carriers in the wings would recombine more rapidly, reducing the contribution of diffusion current. However this explanation alone does not account for observation. At 1550 nm the detectors show little absorption in the dopant (in both waveguide mode simulations and measurement). Detectors were measured with dopant up to 500 nm away from the waveguide sidewall. Therefore the contribution of diffusion current will be very small, and may materialize itself as noise rather than the dominant response.

As the devices in both cases appear to be limited by the  $RC$  time constant, few possibilities for the bandwidth disparity remain. The detector layers were extremely similar for IME #2 and #3 (with the exception of the coupling structures). The measured capacitance of the devices were similar, yet almost a factor of 4 difference in bandwidth is seen. Unfortunately resistivity test structures were not present, so determining whether the fabrication was to specification of the design is difficult.

The influence of defect concentration on operation speed requires further characterization. The LETI and IME #1 devices were characterized with large variation in implant dose, and no observable difference was found. However the potential impact of dose may have been concealed by their relatively slow  $RC$  time constant. The faster IME #3 devices were not characterized with the same degree of variation in defect concentrations. The limited variations in dose of the IME #3 detectors did not reveal any trends, but it would be premature to suggest there is no time response dependence on dose.

## 6.5 Summary

This chapter has demonstrated a defect mediated silicon avalanche detector operating at 20 Gbit/s. The detector is 1 mm long with a responsivity of 0.3 A/W at 2.02  $\mu\text{m}$  and has a small signal bandwidth of 12.5 GHz, limited by the  $RC$  time constant.

This represents the fastest demonstrated operation in this wavelength range for any previously reported waveguide-integrated detector, and a significant improvement over previous defect mediated silicon detectors in this range. It also represents the fastest large signal operation (open eye diagrams) of defect mediated detectors at any wavelength range. Previous demonstrations have shown error free operation limited to 10 Gbit/s [17,18]. Considering the noise inherent in the experimental setup, this detector is likely to achieve error-free operation at 20 Gbit/s.

The detector has showed sensitivity at wavelengths up to 2.5  $\mu\text{m}$ . A significant drop in sensitivity is seen above 2.2  $\mu\text{m}$  which is partly due to the waveguide geometry. Efficient detection at these extended wavelengths should be feasible with larger waveguides, however this may limit the high-speed performance.

This detector shares the fabrication procedure of earlier devices in this thesis. Fabrication is straightforward, incorporating standard CMOS ion implantation techniques.

The question of ultimate operation speed for defect based devices remains open. The limitation of the avalanche detectors in this thesis is suggested to be the  $RC$  time constant. While the limitations of the LETI and IME #1 devices of chapter 4 were evident, the origin of the limitation to the IME #2 devices was not.

What is certain is that the defect mediated absorption process can occur rapidly, and for an optical intensity sufficient to support data transfer. Previous work in silicon [19] demonstrated this for a small signal, yet the same devices showed only 10 Gbit/s large signal operation. The results of this chapter have extended the large signal operation speed.

## References

1. Richardson, D.J. Filling the light pipe. *Science* **330**, 327-328 (2010).
2. Mode-Gap research project. <http://modegap.eu> (2014).
3. Li, Z. *et al.* Diode-pumped wideband thulium-doped fiber amplifiers for optical communications in the 1800–2050 nm window. *Opt. Express* **21(22)**, 26450-26455 (2013).
4. Soref, R.A. Mid-infrared photonics in silicon and germanium. *Nature Photon.* **4(8)**, 495-497 (2010).
5. Ye, N. *et al.* InP based active and passive components for communication systems at 2  $\mu\text{m}$ . *J. Lightwave Technol.* **PP(99)**, (2014).
6. Roelkens, G. *et al.* Silicon-based photonic integration beyond the telecommunication wavelength range. *IEEE J. Sel. Top. Quantum Electron.* **20(4)**, 394-404 (2014).
7. Soref, R.A. Silicon-based silicon–germanium–tin heterostructure photonics. *Phil. Trans. R. Soc. A.* **372** (2014).
8. Gan, X. *et al.* Chip-integrated ultrafast graphene photodetector with high responsivity. *Nature Photon.* **7**, 883-887 (2013).
9. Zhang, Y., Zhang, L. and Zhou, C. Review of chemical vapor deposition of graphene and related applications. *Accounts chem. res.* **46(10)**, 2329-2339 (2013).
10. Souhan, B. *et al.* Error-Free Operation of an All-Silicon Waveguide Photodiode at 1.9 $\mu\text{m}$ . *IEEE Phot. Tech. Lett.* **25(21)**, 2031-2034 (2013).
11. Souhan, B. *et al.* Si<sup>+</sup>-implanted Si-wire waveguide photodetectors for the mid-infrared. *Opt. Express* **22**, 27415-27424 (2014).
12. Mailoa, J.P. *et al.* Room-temperature sub-band gap optoelectronic response of hyperdoped silicon. *Nature Commun.* **5**, 1-8 (2014).
13. Almeida, V., Panepucci, R. & Lipson, M. Nanotaper for compact mode conversion. *Opt. Lett.* **28**, 1302-1304 (2003).

14. Mashanovich, G.Z. *et al.* Low loss silicon waveguides for the mid-infrared. *Opt. Express* **19(8)**, 7112-7119 (2011).
15. Thomson, D. *et al.* Optical detection and modulation at 2 $\mu$ m-2.5 $\mu$ m in silicon. *Opt. Express* **22**, 10825-10830 (2014).
16. Emmons, R.B. Avalanche-photodiode frequency response. *J. Appl. Phys.* **38**, 3705-3714 (1967).
17. Grote, R.R. *et al.* 10 Gb/s error-free operation of all-silicon ion-implanted-waveguide photodiodes at 1.55  $\mu$ m. *IEEE. Phot. Tech. Lett.* **25(1)**, 67-70 (2013).
18. Ackert, J.J. *et al.* 10 Gbps silicon waveguide-integrated infrared avalanche photodiode. *Opt. Express* **21**, 19530-19537 (2013).
19. Geis, M.W. *et al.* Silicon waveguide infrared photodiodes with > 35 GHz bandwidth and phototransistors with 50 AW-1 response. *Opt. Express.* **17(7)**, 5193-5204 (2009).

# Chapter 7 Summary, Suggested Future Work & Outlook

## 7.1 Summary of work

This thesis focused on the high-speed capability of defect-mediated silicon photodiodes. It has established the feasibility of these photodiodes for communications applications over a wide wavelength region through detailed results of high performing device structures.

A study of resonant detectors with lattice defects was presented in chapter 3. It included the characterization of defects within passive silicon resonators, followed by experimental results from ring and disk resonator detectors at high speed. The passive characterization revealed the change in the real part of the refractive index, as well as the optical loss; important information for a resonant device incorporating defects. Experimental characterization of resonant detectors revealed limited operational bandwidth, significantly less than predicted based on the device design. Instability while operating on resonance was observed in microdisk structures. The cause of this instability is due to free carriers introducing a resonance shift. A simple model was presented for a ring resonator which shows a significant resonance shift, capable of influencing power levels in the ring. These effects make it difficult for high-speed operation of resonant detectors of this nature. However, promising high sensitivity results showing the detectors operating in steady-state with low optical intensity were presented.

In chapter 4 high-speed characterization of silicon defect based detectors operating in the avalanche regime were presented. These detectors were in a non-resonant configuration and demonstrated error-free operation at 10 Gbit/s at a wavelength of 1550 nm. The effects of both annealing and operation temperature was explored. The

combination of high responsivity and error-free operation demonstrated the feasibility of monolithic silicon detectors for communications applications.

In chapter 5, the fabrication, characterization and measurement of surface-state photodetectors was presented. These devices absorb light through defect states at the surface of the silicon waveguide. The devices in this thesis showed large improvements over existing work on silicon surface-state detectors. The simple nature of these devices means they are suitable for power monitoring or sensing applications. A comparison of bulk defect and surface-state devices was made which showed that the bulk defects did not significantly inhibit high-speed operation.

Operation of defect-based photodiodes at mid-infrared wavelengths was explored in chapter 6. The detectors showed sensitivity at wavelengths up to 2.5  $\mu\text{m}$ . Most significantly, they showed high-speed operation at 1.96  $\mu\text{m}$  with responsivity competitive with alternative material platforms. This wavelength range is significant as future communications systems may employ photonic band-gap fibers and thulium-doped fiber amplifiers.

## **7.2 Suggested future work**

### **7.2.1 Avalanche detection**

Defect-based devices have been studied for many years, but by a relatively small number of researchers within the field of silicon photonics. What may not be obvious is that the optimization of the defect concentration remains to be done. The parameter matrix for the creation of lattice defects through ion implantation is extensive and has not been exhaustively explored. The variables include; ion species, dose, energy, annealing temperature and annealing time. While this thesis has filled in some data points in this regard, it is by no means complete and it's likely that improvements are left to be found in detector efficiency. The difficulty of such a study is the fabrication burden, as detector variations (e.g. waveguide width) can be varied across a die, implantation and annealing

parameters cannot. Given the detector performance demonstrated in this thesis and the real potential for communications applications, it may become worthwhile to undertake such ‘brute force’ investigations.

The devices in this thesis have achieved high bit-rates, but the ultimate speed limitation of defect mediated devices was not determined. The devices here were found to be limited by the  $RC$  time constant. Therefore electrical optimization may eventually reveal the time response of the defect mediated absorption and charge separation process. During work on this thesis a study of operation speed versus dose and annealing temperature was carried out. The data is not included in this thesis as no significant trends were observed. This study was carried out with the earlier, and slower, generation of devices. In light of the faster performing detectors achieved later, this study could be repeated, as a limited number of dose variations were tested in this case.

A significant experiment left to be completed is the determination of the  $k$  value (i.e. the impact ionization ratio of electrons and holes). This describes the noise related to avalanche multiplication, and the gain-bandwidth limitation of an avalanche detector. This value has been measured for silicon, but not for silicon with lattice defects. A planar detector would be preferred to determine  $k$ , as it removes the highly non-uniform electric field present in the waveguide geometry and thus the varying multiplication factor. However, without a waveguide structure the sensitivity of the detector is greatly reduced. The  $k$  value would also determine the viability of a separate absorption and multiplication structure, or whether the current bulk implant technique is preferable.

### **7.2.2 Long wavelength detection**

There is a sizeable investigation remaining of lattice defect mediated detectors at long wavelengths. The responsivity at longer wavelengths requires more attention. In chapter 6 the devices lose response, in part, to the wavelength dependence of the waveguides. The design of waveguides for longer wavelengths is required to accurately determine the efficiency further into the mid-infrared.

The temperature response of the devices has not been studied. This includes both the permanent change of detector responsivity with annealing and the temporary change with ambient temperature. Additionally, the optimal defect concentration may not be equivalent for all wavelengths if different defect complexes are responsible for absorption in the mid-infrared.

### **7.2.3 Surface-state photodetection**

Chapter 5 of this thesis presented results for a surface-state detector. These detectors show promise for power monitoring and potentially surface chemistry sensitive applications. This device was not the primary focus of this thesis, and represents an area ripe for further investigation.

Future studies with this detector are recommended to focus on varying the surface treatment as a means to improve detector efficiency. The investigation in this thesis included devices with native oxide from atmospheric exposure at room temperature. A scheme to investigate alternative exposures could include an etch of the native oxide, followed by varied lengths of exposure and potentially a deposited oxide (or other compound) to prevent further reactive oxidation of the surface. Alternatively, increasing surface roughness may yield higher absorption due to the increased surface area. Exploring different waveguide structures is another means to improve the efficiency. Devices in this thesis used a simple rib waveguide (500 x 220 nm) but changes in dimension will lead to changes in optical overlap with the surface region.

## **7.3 Outlook**

Silicon photonics is a growing field and the last decade has seen an increasing volume of research. A great deal of this work involves devices with extremely complex design and fabrication. One might observe that the imagination of researchers surpasses the technological capabilities of the day (and so it should). Yet the adaptation of research into

manufactured technology is ultimately driven by economics and it is in this context that the work in this thesis holds value.

This thesis demonstrated high performing photodetector structures for use in silicon photonic integrated circuits. The most remarkable aspect of this class of detector is the relatively basic fabrication process. Competing photodetectors on the silicon platform require hybrid material systems which often require non-standard approaches. Hybrid structures may limit the economic viability of the silicon photonic platform, as multiple different material requirements may become unfeasible when incorporated into increasingly integrated environments.

The monolithic silicon approach taken in this thesis could be implemented in a variety of silicon process configurations. This class of detector has been demonstrated to be capable for data communication applications, whether it will be adopted is uncertain as such a choice requires a balance between fabrication cost and performance.

Finally, it is important to realize that applications exist beyond data communication. Data communication demands high performance and is a high value application, meaning that relatively higher cost hybrid approaches may be employed. As the manufacturing of photonic integrated circuits matures, especially cost sensitive applications will emerge. This might include sensing or lab-on-a-chip applications that make use of ‘disposable’ PICs. Such devices would greatly benefit from monolithic silicon solutions.